

Characterization of Epoxy/Copper Interphases using Nanoindentation

Vorgelegt von

M.Sc.

Karim Elabshihy

geb. in Dakahliya, Ägypten

von der Fakultät III – Prozesswissenschaften

der Technischen Universität Berlin

zur Erlangung des akademischen Grades

Doktor der Ingenieurwissenschaften

- Dr.-Ing -

Genehmigte Dissertation

Promotionsausschuss:

Vorsitzender: Prof. Dr. John Banhart

Gutachter: Prof. Dr.-Ing. Manfred H. Wagner

Gutachter: Prof. Dr. rer. nat. Heinz Sturm

Gutachter: Dr.-Ing. Gerhard Kalinka

Tag der wissenschaftlichen Aussprache: 26. Oktober 2016

Berlin 2016

Abstract

Characterization of the size and mechanical properties of interphases is essential when designing multicomponent materials. Polymer/metal composites, often found in microelectronics, are an example of such multicomponent materials, where understanding the interphase properties can provide vital information about the durability of a finished product. When nanoindentation is used to investigate the size and mechanical properties of an interphase, a common challenge is that the indenter or the stress zone formed around it are often restricted by the reinforcement, making it difficult to distinguish the mechanical property variations caused by the interphase itself from those caused by the mechanical bias effect. In addition, due to the relatively small size of the interphase, it is usually difficult to apply multiple adjacent indents in the interphase region without overlap.

In this work, a testing system was developed that allows applying nanoindentation in a polymer/metal interphase region, while excluding the mechanical bias effect. We used an epoxy/Cu/epoxy system, where only one epoxy side was cured while in contact with the copper. This way, the other independently cured epoxy side can be used as a reference to determine the indent affected zone (IAZ) and account for it in the interphase measurements. Using the finite element method (FEM), we confirmed the validity of the proposed system.

A method of applying multiple adjacent indentations without overlap was introduced, and nanoindentation was used to investigate the interphase between Cu and two different epoxy systems; amine-cured and anhydride-cured. Moreover, the Berkovich indenter was oriented symmetrically with respect to the Cu, in order to avoid asymmetry-associated errors. The nanoindentation results showed that a Cu layer that is only 10 nm thick still exhibits a constriction effect on the indentations in its vicinity. The amine-cured epoxy did not show any sign of interphase existence using the introduced method. In contrast, a soft interphase with a thickness of $\sim 1.7 \mu\text{m}$ was measured by nanoindentation experiments on the anhydride-cured epoxy. Furthermore, it was shown that the proposed system can be used to determine the interphase thickness as well as its relative mechanical properties regardless of the indentation depth. Atomic force microscopy (AFM) measurements confirmed the nanoindentation results. This system can be further used for investigating other polymer/metal interphases to better understand the factors influencing them, thus helping engineer the interphase size and properties in a way that enhances composite performance.

Zusammenfassung

Die Charakterisierung von Ausdehnung und mechanischen Eigenschaften der „Interphase“ ist von besonderem Interesse beim Einsatz mehrphasiger Werkstoffe. Beispiele für solche partikelverstärkten Polymere findet man in der Mikroelektronik, wo sich die Eigenschaften der Interphase erheblich auf die Gebrauchseigenschaften und die Dauerhaftigkeit der fertigen Produkte auswirken kann. Bei Verwendung der Methode der Nanoindentation zur Charakterisierung der Interphase tritt allerdings das Problem auf, dass die Spannungszone, die sich im Material in der Nähe des Eindrucks im weichen Material aufbaut, stark von dem steiferen Material der Verstärkungskomponente beeinflusst wird. Dies macht es schwer, die Interphasen-Eigenschaften von den Eigenschaften der Versteifung zu isolieren. Weiterhin besteht das praktische Problem, dass die geringe Schichtdicke der Interphase die Platzierung der Indents erschwert, denn sie sollen einerseits die Phase möglichst vollflächig bedecken, aber andererseits sich nicht gegenseitig überlappen.

Die vorliegende Arbeit beschreibt einen Proben- und Versuchsaufbau, der die Untersuchung von Interphasen zwischen Metall und Polymer mittels Nanoindentation erlaubt, wobei der Einfluss der versteifenden harten Metallphase weitgehend unterdrückt wird. Das Verfahren wird anhand eines Systems Epoxid-Kupfer-Epoxid vorgestellt. Die eine Epoxidschicht ist während ihrer Aushärtung mit Kupfer in Kontakt und kann ggf. eine Interphase aufbauen, während die andere beim Kontakt mit Kupfer bereits ausgehärtet ist und Referenz ohne Interphase herangezogen werden kann. Die gefundenen Unterschiede zwischen den beiden Kontaktflächen können auf den Einfluss der Interphase zurückgeführt werden, was auch mit FEM-Simulationen validiert werden konnte.

Die Mess-Methodik wurde um mehrere Aspekte erweitert. Zum einen wurde ein Regime der Platzierung der Indents eingeführt, das eine Überlappung und gegenseitige Beeinflussung ausschließt. Ferner wurde eine präzise symmetrische Orientierung des Indenters bezüglich seiner Lage zur Interphase sichergestellt. Vor diesem Hintergrund wurden zwei unterschiedlich aushärtende Epoxidsysteme untersucht, ein amin- und ein anhydrid-härtendes System, wobei sich zeigte, dass das chemische Regime erhebliche Auswirkung auf die Ausbildung der Interphase haben kann. Im Ergebnis zeigte sich, dass selbst eine 10 nm dicke Kupferschicht noch Auswirkungen auf die Kontaktsteifigkeit eines Indents hat, die nicht vernachlässigt werden können. Während mit dem amin-härtenden System mittels der

Nanoindentation keine Interphase nachgewiesen werden konnte, zeigte sich bei Vermessung des anhydrid-härtenden Systeme eine Schicht mit der Ausdehnung von $\sim 1.7 \mu\text{m}$.

Mittels der vorgestellten Versuchsführung ist es möglich, sowohl die Ausdehnung der Interphase, als auch deren relative Steifigkeit unabhängig von der Eindringtiefe des Indenters zu bestimmen. Sowohl FEM-Simulationen als auch AFM-Messungen bestätigen die Messungen mit der Nanoindentation. Insgesamt wird ein Verfahren vorgestellt, dass es erlaubt, die Kontaktschicht zwischen Polymeren und Metall zu untersuchen und hinsichtlich der Anwendung bei mehrphasigen Werkstoffen zu optimieren.

Acknowledgments

I would like to express my gratitude to *Prof. M. H. Wagner* for accepting to supervise, evaluate and grade this work.

I am further thankful to *Prof. Heinz Sturm* for the fruitful suggestions regarding the project and his generous regards in order to advance this doctoral work smoothly.

I would like to especially thank *Dr. Gerhard Kalinka* for organizing and providing a state-of-the-art project, being abundantly helpful and offering invaluable assistance, support and guidance throughout the research project.

Special thanks to *Dr. Dorothee Silbernagl* and *M.Sc. Media Ghasem Khorasani* for performing the AFM measurements and help analyzing the results.

I would also like to thank *Dipl.-Ing Titus Feldmann* for showing me how to run FEM calculations on ANSYS, and *Dipl.-Ing. (FH) Matthias Weise* for depositing the copper layers.

I would like to express my appreciation to my group members at BAM including:

Prof. Christian Marotzke for his support and kind care during my time at BAM,

Frau Martina Bistriz for helping in sample preparation via microtome,

Herr Thomas Linke for solving all IT-related issues,

Herr Lothar Buchta for being a nice and friendly office colleague,

Oliver Schwarze for showing me how to mix and cast bubble-free epoxy resins,

Fabian Roth and Nicolai Schmidt for their help in building the experimental setups.

I would also like to thank my friends in Egypt and Germany for their continuous support, especially *Sherif Madkour* for the reviving coffee breaks, and *Amr Abdeen* for the long PhD-related and unrelated Skype discussions.

Finally, I would like to thank my family. Especially my parents and my sister, without whom none of this would have been possible, and who have supported my passions and so often put my aspirations above all other considerations.

Table of Contents

Table of Contents	I
List of Figures	III
List of Tables.....	VII
1 Introduction	1
1.1 Objectives and Hypotheses.....	3
2 Theoretical Background.....	5
2.1 Epoxy Composites	6
2.1.1 Chemical Structure.....	8
2.1.2 Curing Mechanisms	9
2.1.3 Structure-Property Relationships	12
2.2 Interphases	14
2.2.1 Interphase Formation Mechanisms.....	16
2.2.2 The Role of Interphases in Polymer Composites.....	20
2.3 Mechanical Characterization of Interphases.....	24
2.3.1 Nanoindentation.....	24
2.3.2 Atomic Force Microscopy	36
2.3.3 Nanoindentation-AFM Comparison	39
3 Finite Element Modeling of Nanoindentation on Epoxy/Copper Interphases.....	41
3.1 Introduction.....	42
3.2 Experimental Work.....	45
3.3 Results and Discussion	49
3.4 Conclusion	61
4 Characterization of the Interphase in an Amine-cured Epoxy/Copper System.....	62
4.1 Introduction.....	63
4.2 Experimental Work.....	65
4.3 Results and Discussion	78
4.4 Conclusion	92

5	Characterization of the Interphase in an Anhydride-cured Epoxy/Copper System..	93
5.1	Introduction.....	94
5.2	Experimental Work.....	97
5.3	Results and Discussion	99
5.4	Conclusion	107
6	Concluding Remarks.....	108
	References	112

List of Figures

Figure 2.1: Epoxy ring structure with the typical bond angles and lengths	8
Figure 2.2: Epoxy ring opening mechanisms (Nu=Nucleophile, E= Electrophile)	8
Figure 2.3: Commercial preparation of diglycidylether of bisphenol-A (DGEBA)	9
Figure 2.4: Curing reaction of epoxy using amines	10
Figure 2.5: (a) Initiation, (b) propagation and (c) chain termination steps of the anhydride-epoxide copolymerization initiated by tertiary amines	11
Figure 2.6: Initial tensile modulus (E_y), fracture strength (σ_f) and fracture toughness (K_{IC}), as a function of the curing agent concentration.....	13
Figure 2.7: The fiber/matrix interphase. The arrows represent the directions in which the thermal, chemical or mechanical environments can reach the interphase.	15
Figure 2.8: Schematic representation of an epoxide (E)/amine (A) mixture, where the amine monomer adsorbs preferentially onto a carbon fiber surface	17
Figure 2.9: The concentration profile of sulfur-containing amine molecules in an amine/epoxy mixture cured while in contact with a copper substrate	19
Figure 2.10: Load cycles and the corresponding load-displacement curves for (a) elastic-plastic solid and (b) visco-elastic-plastic solid.....	25
Figure 2.11: Schematic illustration of indentation load-displacement data showing the important measured parameters.....	27
Figure 2.12: Schematic illustration of the unloading process, showing the parameters characterizing the contact geometry.....	27
Figure 2.13: Concepts used to understand and define the effective indenter shape.....	30
Figure 2.14: (a) Berkovich indenter geometry and (b) the corresponding projected area	32
Figure 2.15: (a) SEM image of a nominal 1 μm radius sphero-conical indenter. (b) AFM image showing surface profile of a 10 μm spherical indenter	32
Figure 2.16: Ratios between actual and ideal contact areas at different penetration depths....	33
Figure 2.17: (a) Cross-sectional view and (b) plan view for the effect of piling-up and sinking-in on the actual contact area for penetrations of the same depth.....	34

Figure 2.18: Schematic of the effect of load frame deflection by a displacement c during nanoindentation test.....	35
Figure 2.19: Schematic illustration of AFM setup.....	37
Figure 2.20: (a) An ideal force–distance curve. (b) The deflection data from (a) plotted with respect to time. (c) A schematic explanation of the different regions of the force-distance curve.	38
Figure 3.1: Plastic deformation zone, of width W_{pl} created by an indenter pressing into a ductile material.....	42
Figure 3.2: An increase of hardness (●) and elastic modulus (■) with indentation depth in nanoindentation made in close proximity to the fiber.....	44
Figure 3.3: Geometry of the Berkovich indenter used in the simulation.	46
Figure 3.4: Geometry of the epoxy/Cu/epoxy system.....	46
Figure 3.5: Geometry of the epoxy/Cu/epoxy system with an interphase (IP) in only one of the two epoxy sides.	47
Figure 3.6: Meshing of the system with a finer mesh around the copper.....	48
Figure 3.7: Finer meshing around the indenter tip using the sphere of influence meshing method.....	48
Figure 3.8: Force-displacement curves of 150 nm deep indents, applied on both sides of a perfect epoxy/Cu interface at different distances.	50
Figure 3.9: Variation of the elastic modulus values with distance from copper using 150 nm deep indentations.....	51
Figure 3.10: The von-Mises stresses accompanying a 150 nm deep indent, applied 800 nm away from the copper.	52
Figure 3.11: Force-displacement curves of 150 nm deep indents applied on both sides of copper, where a softer interphase with the epoxy is present in only one side.....	53
Figure 3.12: Variation of the elastic modulus values with the distance from copper in an epoxy/Cu/epoxy system with an interphase on only one side of the copper, using 150 nm deep indents. The diagrams below show the IAZ at the points when it (a) starts touching Cu, (b) stops touching copper and starts touching the IP only, and (c) stops touching the IP.....	54
Figure 3.13: The von-Mises stresses accompanying a 150 nm deep indent applied at 600 nm distance from the copper in the presence of a 400 nm interphase.....	56
Figure 3.14: Force-displacement curves of 60 nm deep indents applied on both sides of copper, where a softer interphase with the epoxy is present in only one side.....	57

Figure 3.15: Variation of the elastic modulus values with the distance from copper in an epoxy/Cu/epoxy system with an interphase on only one side of the copper, using 60 nm deep indents. The diagrams below show the IAZ at the points when it (a) starts touching Cu, (b) stops touching copper and starts touching the IP only, and (c) stops touching the IP.....	58
Figure 3.16: Comparing the mechanical property variation in the proposed model when the indentation depth applied is 60 or 150 nm.	60
Figure 4.1: Variation of elastic modulus across the interphase region between the fiber and matrix obtained by 50 nm depth indentations, and spacing of: (a) 800 nm and (b) 400 nm....	63
Figure 4.2: FMM amplitude profile of epoxy/copper interphase with Gaussian fit curves	65
Figure 4.3: Illustration of the sample preparation concept.....	66
Figure 4.4: The Teflon [®] mold used for casting the samples.	68
Figure 4.5: The procedure followed to prepare epoxy/Cu/epoxy samples.....	69
Figure 4.6: The sandwich sample shape (a) after trimming and (b) after cutting with the microtome.....	70
Figure 4.7: Illustration of the microtome setup and the involved clearance angle.	71
Figure 4.8: Schematic illustration of the TriboScope in use with a scanning probe microscope (SPM).	72
Figure 4.9: Schematic illustration for the temperature regulation cycle	74
Figure 4.10: Temperature profile inside the chamber over a period of 4 hours.....	75
Figure 4.11: Illustration of the method used to apply indentations across the copper.....	76
Figure 4.12: Mean and standard deviation of elastic modulus values resulting from different indentation forces.	78
Figure 4.13: Indentations approaching copper with increments of 200 nm using a force of 0.2 mN without overlap.....	79
Figure 4.14: Variation of the apparent elastic modulus values with the distance from the 100 nm thick copper layer when 0.2 mN indentations are applied with a spacing of 200 nm.	80
Figure 4.15: FEM calculations for 150 nm deep indentations applied across a perfect Cu interface using randomly oriented Berkovich indenter	81
Figure 4.16: Schematic illustration of the projected areas of two indentations applied on both epoxy sides at the same distance d from the copper, when the Berkovich indenter is oriented (a) symmetrically and (b) asymmetrically with respect to the copper line.	82

Figure 4.17: Imprints of 0.2 mN indentations that are aligned symmetrically with respect to the copper.	83
Figure 4.18: Apparent elastic modulus variation across the 100 nm thick copper, resulting from 0.2 mN indentations with 200 nm spacings.....	84
Figure 4.19: 0.2 mN indentations with a spacing of 200 nm performed across different copper thicknesses.....	85
Figure 4.20: Imprints of 50 μ N indentations approaching the copper interface with 50 nm increments.	86
Figure 4.21: 50 μ N indentations with a spacing of 50 nm performed across 75 nm thick copper.....	87
Figure 4.22: Separation of the two epoxy parts in order to investigate the interphase directly as a function of indentation depth	88
Figure 4.23: Multiple indentation series with different depths used for direct investigation of the interphase.	88
Figure 4.24: Apparent elastic modulus as a function of indentation depth for both sides of the amine-cured epoxy.	89
Figure 4.25: AFM topography image of the epoxy/Cu/epoxy sample with a copper thickness of 20 nm.	90
Figure 4.26: A stiffness map generated by applying AFM force-distance measurements across the copper	91
Figure 5.1: Apparent elastic modulus variation resulting from 0.2 mN indentations across the copper with 200 nm spacings.	99
Figure 5.2: Apparent elastic modulus variation resulting from 0.1 mN indentations across the copper with 150 nm spacings.	101
Figure 5.3: Apparent elastic modulus variation resulting from 0.08 mN indentations across the copper with 100 nm spacings.	101
Figure 5.4: Apparent elastic modulus variation resulting from 200 nm indentations with 200 nm spacings, across 40 nm thick copper.....	103
Figure 5.5: Apparent elastic modulus as a function of indentation depth for both sides of the anhydride-cured epoxy.....	104
Figure 5.6: AFM topography image of the epoxy/Cu/epoxy sample with a copper thickness of 10 nm.	105
Figure 5.7: A stiffness map of the anhydride-cured samples generated by applying AFM force-distance measurements across the copper.....	106

List of Tables

Table 2.1: Practical adhesion of epoxy systems cured on both degreased and chemically etched metallic substrates	23
Table 2.2: Projected areas, intercept corrections and geometry correction factors for various types of indenters.....	28
Table 3.1: Materials properties used for modeling.....	47
Table 4.1: Specifications of the used epoxy resin and amine-based hardener	67
Table 4.2: The PVD parameters used to deposit copper layers of different thicknesses.	69
Table 5.1: Epoxy/Cu interphase thicknesses reported in different studies, all using DGEBA based resins and aliphatic/cycloaliphatic amine-based hardeners.....	95
Table 5.2: The relation between different reaction regimes and the interphase formation.....	96
Table 5.3: Specifications of the used epoxy resin, anhydride-based hardener and accelerator	97

1

Introduction

In the last few decades, composites have been replacing conventional materials in a wide range of industrial applications. This is due to the superior properties they provide, which cannot be achieved solely by an individual component. Polymer matrix composites (PMCs) are by far the most widely used type of composites.¹ One of the major factors affecting the mechanical performance of PMCs is the effectiveness of the bond between the matrix and the reinforcement in transferring stress across the interface. However, such a well-defined matrix/reinforcement boundary barely exists; instead, a three dimensional heterogeneous region usually forms, now commonly referred to as the interphase.²

The interphase in PMCs is a transition region with a thickness that can range from a few nanometers to a few microns. The morphological features, chemical composition as well as mechanical properties of the interphase differ from those of the bulk matrix or the reinforcement.³ The nature of the interphase (e.g. size and properties) varies depending on the involved composite system. By engineering the interphase appropriately, it can be possible to notably improve the strength and toughness of a composite as well as its environmental stability.⁴ For example, an interphase that is less stiff than the polymer matrix would reduce the overall stiffness and strength of the composite, but increase its fracture resistance.^{3,5} On the other hand, an interphase that is more rigid than the surrounding polymer would reduce the fracture toughness of the composite, but make it stronger and stiffer.⁶ Therefore, a better understanding of the interfacial properties is necessary for evaluating and optimizing the overall performance of PMCs.

Thermosets, such as epoxies, are often used as a matrix material in PMCs. Moreover, epoxy is a widely used polymer material in multiple applications such as anticorrosive coatings or insulators. On the other hand, copper is a popular metal that is commonly used in the field of microelectronics, owing to its high electrical conductivity and relatively low cost. Epoxy/metal surfaces are commonly seen in microelectronics; for instance, in chip packaging where it acts as a protective material.⁷ In this case, the adhesion between the epoxy and the metal layer, and consequently the interphase properties, are crucial for the long-term durability of the product. In particular, characterizing the relative mechanical properties of the interphase can provide valuable information on the stability of the product, as it can be used to predict the stress distribution within the interphase.⁸

One approach for such characterization involves nanoindentation. Nanoindentation (also known as depth-sensing indentation) has gained increasing interest due to its ability to assess the material's mechanical properties on the micro and nano scales. This gives the method an advantage when it comes to testing small volumes,⁹ thin films,¹⁰ or different phases within a material.¹¹ Furthermore, when compared to other micromechanical testing methods, nanoindentation has relatively simple setup and sample preparation. However, applying nanoindentation in the interphase region can be hindered by a few challenges.

When nanoindentation is applied in the interphase region, where the indent is made in close proximity to the reinforcement, the indenter may touch the reinforcement directly, or the development of the plastic zone around the indenter may be constricted.¹²⁻¹⁴ Such a mechanical bias effect occurs within a zone of finite width, and it becomes difficult to differentiate between interphasial property variations and variations related to the mechanical bias effect. In particular, this impediment matters if the width of the interphase is smaller or comparable to the width of the mechanical bias effect zone.¹⁵ Moreover, it is difficult to apply multiple adjacent indentations in the interphase region without overlap.¹³ For these reasons, the clearest nanoindentation results relating to interphase properties are only for systems with a thick interphase region that is artificially created.^{15,16}

1.1 Objectives and Hypotheses

In this study, a system is proposed to investigate the relative mechanical properties and the thickness of the interphase formed between copper and epoxy using nanoindentation, while excluding the mechanical bias effect. The system is based on an epoxy/Cu/epoxy structure, where the copper layer thickness is in the order of only 100 nm or less, and where an interphase is formed on only one side of the copper. There are two hypotheses behind this system: First, when the thickness of the copper layer is very thin, it is not stiff enough to restrict the indenter or the stress zone formed around it. Second, even if such a constriction effect is exhibited by the copper, the presence of the interphase on only one of its sides allows using the other side as a reference for determining the indent affected zone (IAZ). This way, the IAZ can be taken into consideration on the interphase side in order to account solely for the contribution of the interphase to the mechanical property variations.

The validity of this system will be verified using the finite element method (FEM). Moreover, the system will be applied experimentally on two different epoxy systems; one that is amine-cured while the other is anhydride-cured, where the major difference between the two systems is in the curing conditions. A method for applying multiple indentations in the interphase region without overlap will also be proposed. Finally, atomic force microscopy (AFM) measurements will be carried out and compared with nanoindentation results.

In this thesis, an overview of the theoretical background is provided in chapter 2, which mainly covers epoxy, interphases and their mechanical characterization methods. In chapter 3 the proposed system is explained and verified using FEM. In chapter 4 and chapter 5, the proposed system is applied experimentally on amine-cured and anhydride-cured epoxy systems, respectively. This includes sample preparation, nanoindentation testing and AFM measurements. Finally, some concluding remarks and suggestions for future work are provided in chapter 6.

2

Theoretical Background

2.1 Epoxy Composites

A composite material can be defined as an unusual combination of two or more materials that results in specific properties, which cannot be achieved solely by one of the individual components. Thanks to their unique properties, composites can be found in a large and increasing number of commercial engineering applications, such as aerospace industry, electronic packaging, automobile and train structures, biomedical devices, sports and leisure equipment, and mechanical components such as brakes, tanks, pressure vessels and drive shafts. The two main constituents of a composite are the matrix phase, which is the continuous bulk phase, and the dispersed or reinforcement phase. The reinforcement phase can be a fiber, a particle or a laminate. It is usually stiffer, harder and stronger than the matrix phase.¹⁷

Composites are divided into three main categories based on the nature of their matrix phase: metal matrix composites (MMCs), ceramic matrix composites (CMCs) and polymer matrix composites (PMCs). MMCs are usually based on a low-density metal such as aluminum or magnesium, reinforced with particulates or fibers of a ceramic material, such as silicon carbide or graphite. MMCs provide higher specific strength, higher operating temperature and better wear resistance in comparison to unreinforced metals. However, MMCs also have some disadvantages in contrast with conventional metals; for example, higher cost of fabrication and lower ductility and toughness. Ceramics are known for their high compressive strength, high hardness and wear resistance and, most importantly, their high temperature capability which makes them attractive for extremely high temperature applications. A big disadvantage of ceramics, however, is their very low fracture toughness. This is where CMCs have an advantage, since the reinforcements provide toughness to an otherwise brittle matrix. The main reinforcements that are often involved in CMCs are carbon, glasses, glass-ceramics, oxides and non-oxides. A drawback of CMCs, however, is that their processing usually involves very high temperatures, which can only be employed with high temperature reinforcements. The difference in the thermal expansion coefficients between the two constituents can also lead to thermal stresses within the composite upon cooling from the high processing temperature.¹⁷

PMCs are by far the most widely used type of composites. They retain the main advantages of polymers such as ease of processing, low cost, low density, good electrical insulation and

good chemical resistance. However, the low modulus, low strength, and low operating temperatures of polymers can limit their use.¹ Unlike in CMCs where the function of the reinforcement is to provide toughness, the main aim of the reinforcement in PMCs is to provide the required strength and stiffness that are lacking in the polymer matrix. The reinforcement in a PMC can be fibers (continuous or discontinuous), particles, fabrics or laminates. The most commonly used reinforcements in PMCs are glass and carbon fibers. The function of the relatively weak matrix is to bond the reinforcements together, transfer the load between them and provide the necessary integrity for the whole composite.¹⁸

The matrix in PMCs is either a thermoplastic or a thermosetting polymer. Thermoplastic polymers consist of linear or branched molecular chains with strong intramolecular bonds but weak intermolecular ones. They are either amorphous or semicrystalline. By applying heat and pressure, it is possible to melt and reshape thermoplastics. Examples of thermoplastics are polyethylene, polypropylene, polystyrene, polycarbonate and nylons.¹⁸ On the other hand, thermosetting polymers are formed by crosslinking of liquid prepolymers, where the molecules in the system are connected together by covalent bonds, forming large network structures. Unlike thermoplastics, it is not possible to melt and reshape thermosetting polymers once crosslinked and solidified, as heating will cause them to decompose. Examples of thermosets are epoxies, polyesters, phenolics, melamine and ureas.¹⁸ Thermosetting polymers are more commonly used in composites than thermoplastics because of their reactive nature and ease of impregnation, with epoxy being one of the most widely used matrices in PMCs.¹⁹

Although the first products that would now be called epoxy resins were synthesized as early as 1891, it was only until the 1940s that epoxy resins were first commercialized.^{20,21} The term “epoxy resin” is commonly used to refer to both the prepolymer and the cured resins. Some of the characteristics that distinguish epoxy resins are their high chemical and corrosion resistance, good mechanical and thermal properties, outstanding adhesion to different substrates and good electrical insulating properties. Thanks to these properties, epoxy is being used in a wide range of industrial and structural applications such as laminates, composites, tooling, molding, casting, adhesives, and others.²⁰ There are also various fields that can require using epoxy with metals such as microelectronics, aerospace, automotive and food packaging. For example, epoxy can be used as a protective layer on metallic surfaces to protect them from corrosion, or as an adhesive in metal joints of aluminum, steel or titanium.

An epoxy/copper contact can be found often in microelectronics, specifically in the manufacturing of printed circuit boards and integrated chips. Copper is being used for its superior electrical properties, while epoxy acts as a dielectric layer to separate the copper circuitry while providing the necessary integrity for the whole structure.²²

The next sections will discuss the chemical structure of epoxy resins, their curing mechanisms as well as the associated structure-property relationships.

2.1.1 Chemical Structure

Epoxy resin molecules are characterized by having at least two epoxy (also known as oxirane) groups. These groups contain two carbon atoms and one oxygen atom, forming a three-element ring. Figure 2.1 shows the structure of an epoxy ring with the typical bond angles and lengths.

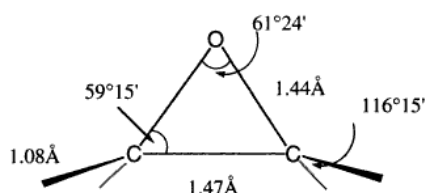


Figure 2.1: Epoxy ring structure with the typical bond angles and lengths.²³

During curing of epoxy resins, one of two ring-opening mechanisms might take place, either an electrophilic attack on the oxygen atom, or a nucleophilic attack on one of the ring carbon atoms. Figure 2.2 illustrates those two mechanisms.

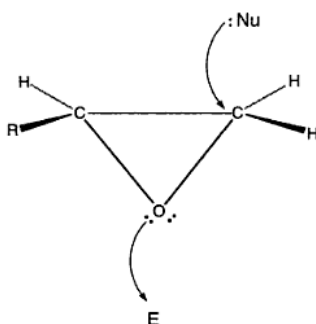


Figure 2.2: Epoxy ring opening mechanisms (Nu=Nucleophile, E= Electrophile).²³

Epoxy resins prior to curing are composed of monomers or short polymers; those monomers could be prepared in several ways. The most common commercial way is the dehydrohalogenation of halohydrins. In this process, a polyfunctional active hydrogen

compound such as an aromatic amine or a phenol reacts with epichlorohydrin (2,3-epoxypropyl chloride) in the presence of a strong base catalyst such as NaOH or KOH. The epoxy ring of the epichlorohydrin reacts easily with the active hydrogen forming chlorohydrin, and a new epoxy group is formed by dehydrochlorination with a stoichiometric amount of alkali. The process is illustrated in Figure 2.3. Multifunctional hydroxylic compounds are necessary for the production of epoxy resins, among which bisphenol-A is considered the most important one. This is due to its easy preparation from cheap starting materials, in addition to its high purity (>95%).²³

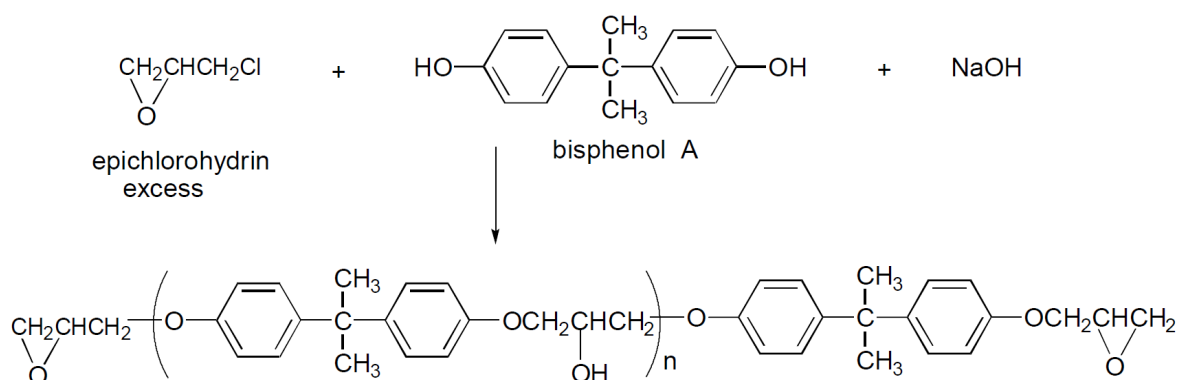


Figure 2.3: Commercial preparation of diglycidylether of bisphenol-A (DGEBA).²³

2.1.2 Curing Mechanisms

Curing reactions takes place as soon as the hardener is added to the resin, and continue while the epoxy part is molded. A wide range of curing agents such as amines, anhydrides, carboxylic acids and phenols can be used for curing epoxy resins, thus converting them into three dimensional insoluble networks. In some cases, the addition of other agents like accelerators, catalysts, fillers, solvents or tougheners is necessary in order to facilitate the curing process or to improve the final product properties. Curing can take place either at room temperature in an exothermic reaction, or might require heating up at elevated temperature depending on the curing agent being used. Amines are the most widely used curing agents for epoxy resins, including aliphatic, cycloaliphatic and aromatic amines.

In their work, Shechter et al.²⁴ explained how the addition of amine to epoxide ring proceeds. An epoxy group would react with a primary amine producing a secondary amine and a secondary alcohol (Figure 2.4a). The resulting secondary amine could then react with another epoxy group producing a tertiary amine (Figure 2.4b). This last reaction occurs with a slower

rate than the primary reaction, as the secondary amine is more sterically hindered than the primary amine. Shechter et al.²⁴ suggested that etherification, which is the reaction of an epoxide with the secondary alcohol (Figure 2.4c), is negligible for most stoichiometric amine concentrations. Etherification might be only observed for excess epoxy mixtures after the depletion of amines.²⁵

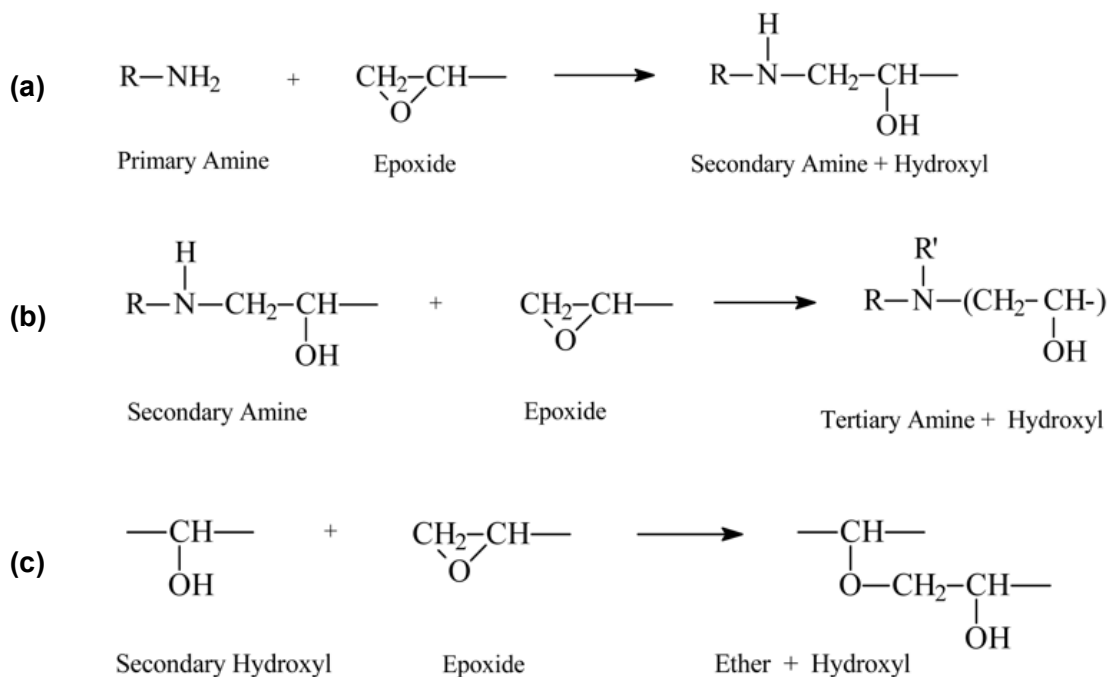


Figure 2.4: Curing reaction of epoxy using amines.²⁶

As the reaction proceeds, the glass transition temperature (T_g) approaches the curing temperature (T_{cure}), until the point where vitrification occurs ($T_g = T_{cure}$). Prior to that point, the reaction is kinetically controlled; after vitrification, the reaction becomes diffusion-controlled. At some point, the reaction stops without the secondary amines being converted yet. For this reason, post curing is necessary, where the mixture is heated up to a temperature higher than T_{cure} , allowing the remaining epoxy groups to react with the remaining secondary amines.²⁵

After amines, anhydrides come as the second most commonly used agents for curing epoxy resins. Similar to amines, anhydride-based curing agents could be aliphatic, cyclic or aromatic. The epoxies formed by the curing of DGEBA with cyclic anhydrides are widely used in the electrical industry as insulators.²⁷ The mechanism of an uncatalyzed reaction between epoxy resins and cyclic anhydrides was first introduced by Fisch and Hofmann.²⁸ In practice, however, the reaction between anhydrides and epoxies is very slow even at

zwitterion that contains a quaternary nitrogen atom and an alkoxide anion. The alkoxide reacts rapidly with an anhydride group, forming a compound with a carboxylate anion as its active center (Figure 2.5a). Propagation proceeds when the carboxylate anion further reacts with an epoxide group, forming an alkoxide anion as the active center. The alkoxide anion reacts successively and at a very fast rate with an anhydride group, renewing the carboxylate anion (Figure 2.5b). Propagation continues through the alternating reaction with epoxide and anhydride groups in a chain copolymerization process. A few studies have suggested the presence of termination and chain transfer reactions, as it was found that the gained molecular weights are lower than those that would be expected for an ideal living polymerization.^{32,33} A possible termination mechanism is shown in Figure 2.5c, where the formation of a tertiary amine is associated. This tertiary amine would be available then for initiating another chain.

2.1.3 Structure-Property Relationships

The hydroxyl groups that form during curing of epoxy resins give them the advantage of being able to adhere to different surfaces. The formed hydroxyl groups create high surface energy, which makes the surface favor bonding to another surface in order to decrease the whole energy of the system. This advantage particularly is the main reason why epoxy resins are being used widely as a matrix in composites, as they tend to form stronger bonds with the reinforcements compared to other thermosetting polymers. Epoxies are in general stronger and stiffer than most competitive resins, thanks to their high aromatic character and internal adherence of the molecules. They also exhibit good creep resistance because of the backbone stiffness caused by the aromatic groups and the high crosslinking density.³⁴

An important aspect to consider in epoxies is their toughness. In order to improve the other important mechanical properties (strength, stiffness etc.), high crosslinking densities (shorter segments) are usually involved. However, the high crosslinking density causes the polymer to be more brittle, as the shorter molecular segments lead to less flexibility in the macromolecules and consequently reduces the toughness. Usually long polymer chains of high molecular weights lead to a lower crosslinking density, since crosslinking only occurs at the chain ends. Therefore, in order to optimize toughness, stiffness and strength, both chain length and crosslinking density should be considered simultaneously. Furthermore, the chemical structure of the segments also plays an important role. For example, aromatic components result in less flexibility but improve the overall strength and stiffness. Common strategies for improving the toughness while maintaining a good strength and stiffness may

involve increasing the aliphatic groups within chain segments, or using flexible curing agents to form flexible crosslinks between the stiff chain segments.³⁴

It is important to take into consideration that the mechanical properties of epoxy are highly dependent on the curing agent concentration as reported by several studies. For example, Selby and Miller³⁵ found that maximum fracture surface energy was achieved at a ratio greater than the stoichiometric ratio, while the tensile and compressive moduli as well as the compressive yield stress reached a minimum at stoichiometry. Kim et al.³⁶ found that the composition had a slight effect on the tensile strength, modulus and elongation, and a larger effect on impact strength and fracture toughness. The mechanical properties of the cured epoxy tended to have relative maxima or minima near the stoichiometric point. Drzal et al.³⁷ have reported similar results as illustrated in Figure 2.6.

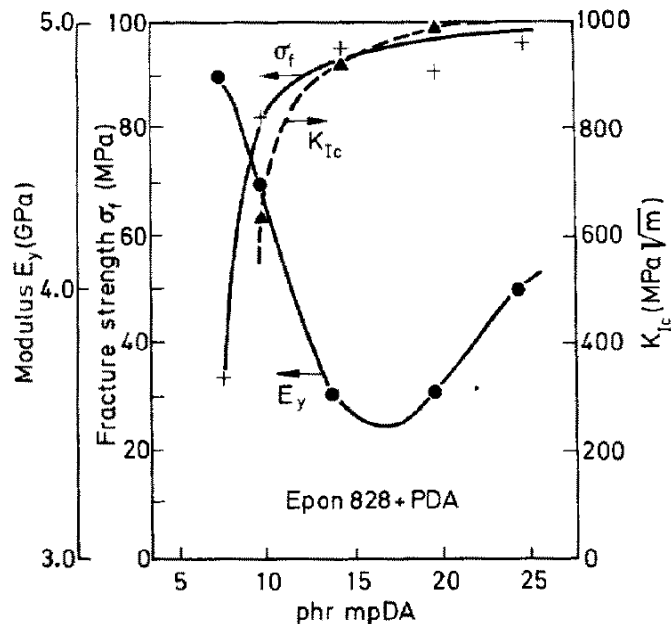


Figure 2.6: Initial tensile modulus (E_y), fracture strength (σ_f) and fracture toughness (K_{Ic}), as a function of the curing agent concentration.³⁷

The plot above shows the initial tensile modulus, fracture strength and fracture toughness of an epoxy system with a stoichiometric point of 14.5 parts per hundred resin (phr) as a function of curing agent concentration. While the fracture strength and fracture toughness reach a relative maximum at the stoichiometric point, the tensile modulus reaches a relative minimum.

Apart from the mechanical properties, epoxies are known for other interesting physical properties. For instance, epoxies have high thermal stability thanks to their high crosslinking

density, which results in a higher allowable use temperature. Epoxies also have good electrical resistance, which allows them to be used as insulators in many electrical applications. The reason behind that is the lack of solvent or monomer residues upon curing, which can become volatile when exposed to heat or strong electrical fields and degrade the electrical properties. Even the molecules of non-crosslinked epoxy resins or hardeners are large enough that they do not volatilize easily. The high aromatic content in epoxies provides them also with good flammability resistance. The aromatic materials tend to char rather than burn freely, which results in a reduction in the ability of the material to be ignited as well as the rate at which it burns.³⁴

2.2 Interphases

As explained earlier, composites consist of two main constituents, the matrix phase and the reinforcement phase. The durability of a composite relies on three main factors: strength and modulus of the reinforcement, strength and chemical stability of the matrix, and the effectiveness of stress transfer across the interface between them.³⁸ In PMCs, whether the reinforcing element is glass or carbon fiber, or metal as in the case of adhesive joints, the bonding of the reinforcement with the surrounding matrix is an essential factor.³

The interface within a composite can be defined as the boundary between the two different constituent phases. In reality, however, such a well-defined boundary rarely exists since chemical interactions usually take place at that boundary, forming a new phase with distinctive properties different from those of either phase.³⁹ This newly formed three-dimensional zone is called the interphase, a term which was first given by Sharpe² and is now being widely used to point out the existence of a chemically and/or mechanically altered zone between two adjacent phases.

Drzal et al.⁴⁰ demonstrated the complexity of the interphase region in fiber-reinforced composites using the schematic model shown in Figure 2.7. Drzal³ defines the interphase as: “The region that exists from some point in the fiber where the local properties begin to change from the fiber bulk properties, through the actual interface into the matrix where the local properties again equal the bulk properties”.

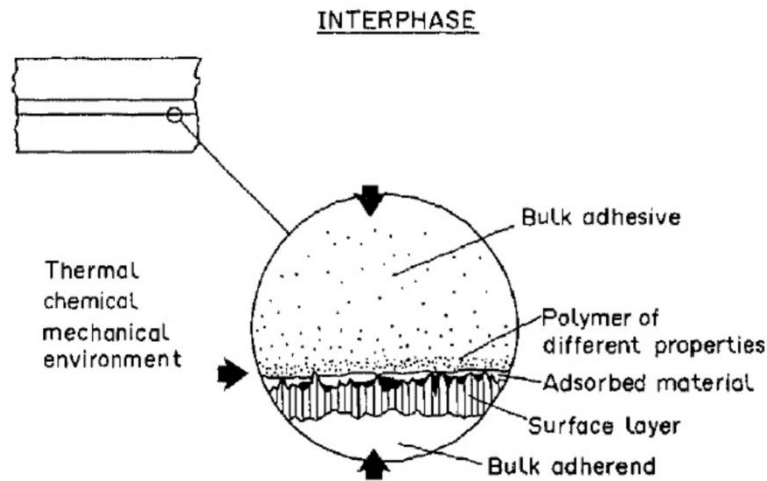


Figure 2.7: The fiber/matrix interphase. The arrows represent the directions in which the thermal, chemical or mechanical environments can reach the interphase.⁴⁰

Drzal³ further demonstrated the presence of various factors with known and unknown effects that can influence the thickness and properties of the interphase region. The reinforcement might have a different morphology near the surface than in the bulk. The area of the surface can be much greater than its geometrical value because of the presence of voids or cracks. Furthermore, the molecular and atomic composition at the surface of the reinforcement can be different from the bulk. For example, in the case of fiber-reinforced polymers, surface treatments of the fibers are usually introduced in order to enhance the adhesion between the fiber and the matrix. These treatments can add chemical groups or remove the original surface, resulting in a new region of a different structure and chemistry. In addition, exposure of the reinforcement surface to the air before processing can allow foreign species to adsorb onto it, causing an alteration or elimination of certain beneficial surface reactivity. If the composite is heated up during fabrication, these adsorbed species can further desorb and disrupt the interface if the composite is heated up during fabrication. Moreover, the preferential adsorption of one of the yet unreacted matrix components onto the reinforcement surface can influence the reactivity, thus altering the local morphology and structure as well.³

Some or all of the factors mentioned above can coexist in an interphase with different magnitudes of influence, resulting in interphases with different properties and different thicknesses that range from a few nanometers to several micrometers, depending on the materials involved in the system and the processing conditions.³ Because the interphase is the region where the bonding between the matrix and the reinforcement happens, the size and properties of the interphase in PMCs are crucial for the durability of the entire composite. It is

necessary to achieve a high bond strength between the matrix and the reinforcement as well as a smooth transition of properties from one phase to the other.⁴¹ Better understanding of the physical and chemical interactions at the interphase as well as the associated interfacial mechanical properties can help engineer the interphase in a way that serves the composite performance. The next section will provide an overview about the formation mechanisms of interphases in different PMC systems, with a focus on interphase formation in epoxy-based composites.

2.2.1 Interphase Formation Mechanisms

In PMCs, the matrix phase can be either a thermoplastic or a thermoset. In the case of thermoplastic composites, the reinforcement is surrounded by the previously polymerized molecular chains. The mechanism of structural accommodation of such chains onto the solid surface is complex. If the whole surface of the reinforcement is capable of adsorption and the molecules are short or flexible enough, the entire molecule might be able to fit onto the surface forming a flat dense layer. Otherwise, only some parts of the chain will be able to adsorb onto the surface, while the other parts will have to readjust their conformation.⁴² Pangelinan et al.⁴³ found that such readjustments will cause the chains to lose their conformational freedom in comparison with other chains in the bulk, resulting in a decrease in the entropy. Therefore, a molecular weight segregation derived by entropic force will occur, where lower molecular weight species tend to accumulate closer to the surface forming an interphase.⁴³ Chains with lower molecular weight are also able to crystallize more readily than higher molecular weight ones.⁴⁴ The degree of crystallinity of the polymer at the interfacial region influences the interaction between the matrix and the reinforcement. Peacock et al.⁴⁵ investigated this influence and found that localized crystallinity at the interface improves the adhesion between the fiber and the matrix.

In thermosets, however, the polymerization mechanism is different. Thermosets are prepared from low molecular weight components (mainly the prepolymer and the curing agent), resulting in a low-viscosity mixture. The small size of the molecules provides them with high mobility and hence, they could achieve large diffusion lengths.⁴⁶ When polymerization occurs in the presence of a reinforcement (e.g. a fiber), and if one of the components has a stronger affinity towards the introduced surface than the other components, a concentration gradient may evolve in the interface vicinity, leading to a stoichiometric imbalance and consequently a different crosslinking density.⁴⁷ Several factors can influence this phenomenon, such as the

surface energy of the fiber and the interaction of the different components with each other and with the fiber surface.⁴⁷ Since it is a diffusion-derived process, the characteristic diffusion length of the components plays a key role as well.⁴⁶ The ongoing crosslinking process is associated with an increase in the average molecular weight. This corresponds to an increase in the viscosity of the mixture and a decrease in the mobility of the molecules, leading to the formation of a concentration gradient. There is no specific rule for the influence of this phenomenon on the interphase properties in comparison with the bulk. While some studies have reported that the interphase is stiffer than the bulk,^{48,49} others have suggested the formation of a softer interphase region.^{6,50}

Interphase Formation in Epoxy Systems

Epoxy systems are a typical example for the formation of interphases in thermosetting-based composites caused by the affinity of one of the components towards the surface of the reinforcement. Palmese and McCullough⁵¹ performed a thermodynamic analysis to quantify the relative interactions of epoxy and amine monomers with carbon fibers. The results showed that there is a thermodynamic driving force encouraging a preferential adsorption of the amines onto the surfaces of the carbon fibers. The same behavior was also reported by Garton et al.⁵² This phenomenon is illustrated in Figure 2.8.

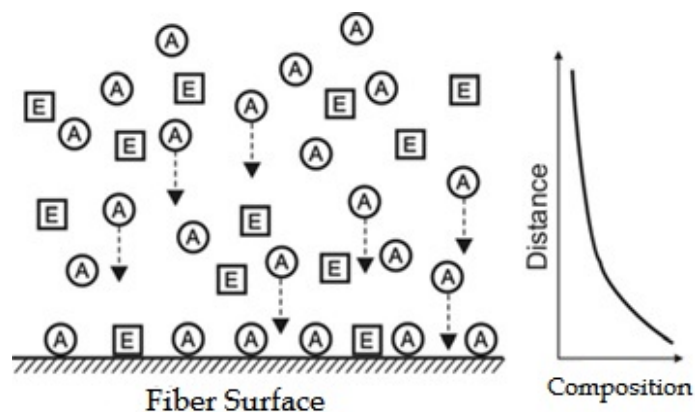


Figure 2.8: Schematic representation of an epoxide (E)/amine (A) mixture, where the amine monomer adsorbs preferentially onto a carbon fiber surface.⁵¹

Fitzer et al.⁵³ also reported a higher affinity of the amine molecules than the epoxy molecules towards graphite fibers. In addition, they compared the wetting behavior of both amine and epoxy to graphite fibers by measuring contact angles. They found that amines were wetting the graphite fibers much easier than the epoxy molecules.

When it comes to epoxy/metal systems, it is important to take into consideration that the surfaces of most metals involved in industry (aluminum, iron, magnesium, nickel, copper, etc.) are in fact metal oxides. As soon as the metal surface is exposed to the atmosphere, an oxide layer will form, whose thickness and structure are dependent upon the nature of the metal and the environmental conditions.⁵⁴ When epoxy systems are cured while in contact with a metal substrate (or metal oxide), preferential adsorption of the curing agent molecules onto the metal surface is usually reported. Hong and Tsai⁵⁵ used diffuse reflectance infrared spectroscopy to study the adsorption behavior of an epoxy/amidoamine system onto the surfaces of iron, aluminum and zinc oxides. They found a preferential adsorption of the amidoamine curing agent onto the three metal oxide surfaces. The amount of adsorbed amidoamine was in the order of iron oxide>zinc oxide>aluminum oxide. They related this behavior to the possible acid-base interactions between the metal surfaces and the curing agent. Nakame et al.⁵⁶ also reported a preferential adsorption of curing agent molecules based on aromatic amines onto the surface of oxidized aluminum particles. The interactions at the cured epoxy resin/oxidized aluminum interface were also acid-base interactions formed between the amino groups and the acidic sites on the oxidized aluminum. Additionally, Boerio and Hong⁵⁷ indicated that dicyandiamide (DICY) curing agent was adsorbing preferentially from the epoxy/DICY mixture onto the surface of silver substrate forming a DICY abundant interface.

The segregation of the curing agent molecules at the interface between epoxy and copper and copper oxides was also reported in several studies.^{3,58-60} After the epoxy mixture is brought into contact with copper, amine molecules preferentially adsorb onto copper while the epoxy/amine reaction is taking place at the same time. Because of the migration of the amine molecules from the bulk to the interface and the formation of an amine enriched zone, an adjacent depletion zone might form which is to be refilled from the bulk.^{61,62} If the curing reaction is slow compared to the rate of diffusion of the molecules, there will be enough time for the needed mass transport and a complete refilling will occur, resulting in a monotonic concentration of amines with respect to the interface. However, if the viscosity increases at a high rate, the mobility of the molecules will decrease and the diffusion will be restricted. Therefore, a non-monotonic concentration profile will form, starting with a zone of high amine concentration followed by a zone of depleted amine concentration, located between the enrichment zone and the bulk epoxy.³ In order to investigate this phenomenon, Chung et al.⁵⁸ used an amine-based curing agent containing sulfur atoms. The spatial variations in

concentration of the curing agent were analyzed by detecting the sulfur content using scanning electron microscopy (SEM) combined with energy dispersive analysis of X-rays (EDX). The results confirmed the presence of an amine enrichment zone that extends up to $\sim 1.4 \mu\text{m}$ from the interface with copper followed by an amine depletion zone until $\sim 3 \mu\text{m}$ before it reaches the bulk region at $\sim 4 \mu\text{m}$ as shown in Figure 2.9.

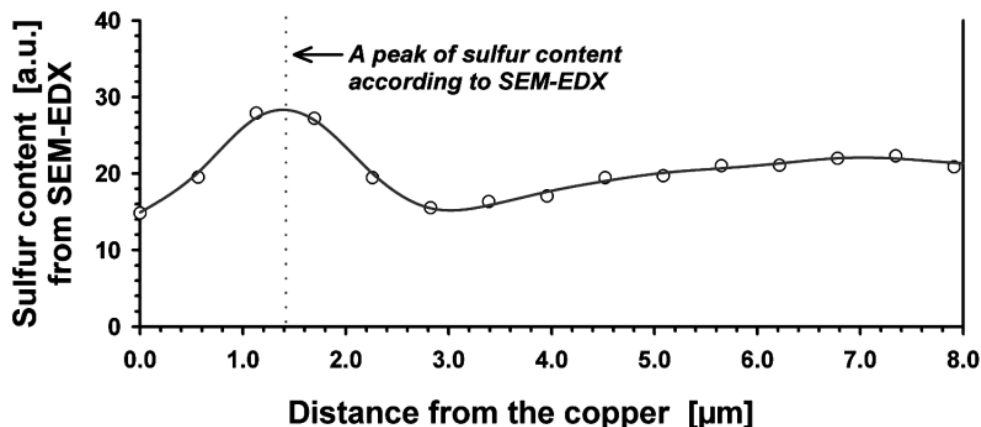


Figure 2.9: The concentration profile of sulfur-containing amine molecules in an amine/epoxy mixture cured while in contact with a copper substrate.⁵⁸

The preferential adsorption of one of the components of an epoxy system onto the reinforcement surface can also be noticed when anhydride-based curing agents are used. Ondrus et al.⁶³ examined the molecular structure of interphases formed when an epoxy/anhydride and epoxy/tertiary amine systems were cured while in contact with metal substrates (aluminum and steel) pretreated with γ -aminopropyltriethoxysilane (γ -APS) primer thin films. The tertiary amine molecules showed minimal interdiffusion with the silane and a relatively sharp interface was formed. On the contrary, the anhydride-based curing agent experienced considerable interdiffusion with the silane and an interphase with a complex molecular structure was obtained. The anhydride reacted with the silane, forming amide and imide structure. Furthermore, the anhydride reacted with the oxidized surface of the metal substrates forming metal salts. Similar results were reported by Boerio and Ondrus⁶⁴ when they used reflection-absorption infrared spectroscopy (RAIR) and X-ray photoelectron spectroscopy (XPS) to investigate the interphases in epoxy/anhydride adhesives on aluminum and copper substrates. The anhydride adsorbed onto the surface of the aluminum oxide substrates forming surface carboxylates. However, when brought into contact with the copper substrate, the anhydride curing agent did not solely react with the cuprous oxide (Cu_2O), but

the cuprous ions were further removed from the oxide and oxidized, forming a thick film of carboxylate salt at the interphase which was described as a weak boundary layer.

When preferential adsorption of a component onto the surface occurs, the ratio between the components at the interface becomes different than the stoichiometric ratio in the bulk. Kelber et al.⁵⁹ suggested that crosslinking is hindered at the interfacial region. This can obviously alter the mechanical properties at the interphase. However, the local mechanical properties are not necessarily directly related to the local concentration variations. For instance, some amine-epoxy systems provide a minimum value of Young's modulus at the stoichiometric ratio.^{3,60}

There are many parameters that can influence the preferential adsorption of one of the system components onto the surface of the reinforcement, thus affecting the size and the properties of the formed interphase. These include the nature of the used curing agent (aliphatic, aromatic or cycloaliphatic), the stoichiometric ratio, the processing parameters (temperature and time) and the surface conditions such as metal oxidization or fiber surface treatment. Since there are two processes occurring simultaneously; the crosslinking and the diffusion of one component towards the surface, the final width of the interphase depends strongly on the ratio of the curing rate to the diffusion rate, which is also known as the Damköhler number.^{51,65} This could be the reason why there are significant differences in the epoxy interphase widths reported in the literature, from a few nanometers to several micrometers.^{16,46,66,67} The influence of the size and properties of the interphase on the matrix/reinforcement interfacial bonding, and subsequently on the whole composite performance will be discussed in detail in the following section.

2.2.2 The Role of Interphases in Polymer Composites

The interface and interphase between the reinforcement and the matrix are considered to be crucial aspects in polymer composites. It is the region where stress concentrations can evolve because of differences in thermal expansion coefficients between the reinforcement and matrix phases, because of the loads applied on the whole structure, or because of shrinkage upon curing in thermosetting matrices and crystallization in some thermoplastic matrices.⁶⁸ In some cases, interfacial interactions are even considered to be the main determinant of the performance and properties of a composite.^{68,69}

In high performance composites, the typical diameter of fibers is 6-10 μm and they usually occupy around 60 volume percent. These systems exhibit a very high fiber surface area to matrix volume ratio; thus, even if the interphase region is small, it might still be representing a considerable portion of the polymer matrix. The volume fraction of interphase material (V_{mi}) in the matrix phase could be estimated using equation (2.1), where (λ) is the interphase size, (d) is the fiber diameter, and (V_f) is the fiber volume fraction.⁵¹

$$V_{mi} = 4 \left(\frac{\lambda^2 + \lambda d}{d^2} \right) \left(\frac{V_f}{1 - V_f} \right) \quad (2.1)$$

This means that if there is a composite system with fibers of 6 μm diameter and an interphase that is 0.1 μm thick, this will result in 10% of the matrix being composed of interphase material. Therefore, even from a geometrical point of view only, small interphases can have a crucial influence on the properties of a composite.

The interphase size and properties can significantly influence the strength and toughness of composites as well as their environmental stability. Drzal⁴⁹ has shown that in epoxy/carbon fiber composites, there is a 200 nm thick interphase whose modulus is higher than that of the polymer matrix. In contrast, Piggott⁷⁰ reported that the interphase might be less rigid than the bulk material. However, there is an agreement on the influence of the mechanical properties within the interphase on the performance of the whole composite. If the interphase is softer than the surrounding polymer, it would result in a reduced overall stiffness and strength, but improved resistance to fracture.³ On the other hand, an interphase that is stiffer than the bulk material would give the composite less fracture resistance but make it strong and stiff.⁶

This relation was confirmed by Di Anselmo et al.⁷¹ when they used the finite element method (FEM) to study the influence of the interphase properties on epoxy/glass fiber composites. They showed that by increasing the interphase stiffness from 0.1 to 2 times the polymer matrix stiffness, a 400% increase in the interfacial shear strength could be achieved. These results also agree with the work of Tsai et al.,⁷² where they concluded that while a weaker interphase might reduce the strength of the composite, it would improve the fracture resistance and result in a tougher composite. Furthermore, the interphase thickness was shown to be influential as well, since smaller interphase thicknesses were correlated with higher composite toughness.

Interphases also play a major role when it comes to the environmental stability of a composite when exposed to a moist environment. This is particularly important in glass fiber reinforced polymer composites, as glass fibers are highly hygroscopic.⁷³ Since the interphase is a region of chemical inhomogeneity, it is often more susceptible to thermal and chemical degradation than the other phases in the composite.⁷⁴ The absorbed moisture on the interphase region can negatively influence the interfacial strength between the fiber and the matrix and thus the performance of the composite. On the one hand, the moisture-induced swelling at the interphase would reduce the mechanical interlocking between the fiber and the matrix. On the other hand, and due to the absorbed moisture, T_g at the interphase can be reduced and the interphase can be degraded if the service temperature exceeds the wet T_g at the interphase.⁷⁵ It was shown that by introducing surface modifications to the fibers and thus altering the interphase properties, the interphase behavior when exposed to moisture can be controlled, and hence, the composite performance can be optimized.⁷⁶

The role of interphase is not of any less importance when it comes to polymer/metal composites. Polymer/metal composites can be found in a wide range of applications such as microelectronics, food packaging, aerospace and automotive industries. Just as in the case of polymer/fiber composites, it is also crucial to achieve the necessary adhesion between polymers and metals in order to ensure the long-term durability of the composite. This is very challenging due to the fact that metals and polymers are of a totally different nature. For example, the cohesive energy in metals is typically two orders of magnitude higher than that of polymers.⁷⁷ Metals are densely packed crystalline solids with a high cohesive energy thanks to their strong metallic bonds, while cohesion in polymers is induced by the very weak van der Waals forces. Moreover, the thermal expansion of polymers is 2-8 times higher than that of metals.¹⁷ These big property differences can lead to adhesion difficulties and further cause adhesion failure at the interface.⁷⁸

Bouchet and Roche⁷⁹ studied the interphases between epoxy and different metallic substrates (aluminum and titanium). By altering the curing conditions (time, temperature and heating/cooling rate), they were able to control the extent of interphase formation. They further investigated the role of interphase formation on the practical adhesion before and after hydrothermal aging. A 3-point flexural test was used for this aim, where either the ultimate load (F_{max}) or the ultimate displacement (d_{max}) was used to evaluate the practical adhesion. The metallic substrates were either degreased or chemically etched, and aging was done by

immersing the samples in water at 40 °C for 24 hours. The results of the flexural test for different samples before aging are shown in Table 2.1. The interphase formation at the different substrates with the different surface treatments resulted always in a decrease in the practical adhesion. This was related to the residual stresses created at the interphase during the polymerization process.

Table 2.1: Practical adhesion of epoxy systems cured on both degreased and chemically etched metallic substrates.⁷⁹

With interphase formation				Without interphase formation			
Aluminium							
Degreasing		Chemical etching		Degreasing		Chemical etching	
F_{\max} [N]	d_{\max} [mm]	F_{\max} [N]	d_{\max} [mm]	F_{\max} [N]	d_{\max} [mm]	F_{\max} [N]	d_{\max} [mm]
$46.3 \pm 11\%$	$0.2 \pm 14\%$	$89.3 \pm 9\%$	$0.22 \pm 3\%$	$112 \pm 12\%$	$0.21 \pm 14\%$	$255 \pm 10\%$	$0.45 \pm 12\%$
Titanium							
Degreasing		Chemical etching		Degreasing		Chemical etching	
F_{\max} [N]	d_{\max} [mm]	F_{\max} [N]	d_{\max} [mm]	F_{\max} [N]	d_{\max} [mm]	F_{\max} [N]	d_{\max} [mm]
$17.7 \pm 10\%$	$0.12 \pm 7\%$	$28.3 \pm 8\%$	$0.32 \pm 3\%$	$68.9 \pm 12\%$	$0.48 \pm 14\%$	$110 \pm 11\%$	$0.59 \pm 13\%$

After aging, there was a considerable decrease in the practical adhesion of the samples without an interphase. On the contrary, the interphase formation kept the practical adhesion quite constant. The reason behind this was suggested to be that the organo-metallic complexes within the interphase act as a barrier against water diffusion inside the system.^{79,80}

In the field of microelectronics, interfacial bonding between metals and the polymers is a serious issue. In electronic packaging, delamination is a common failure mode between the lead frame (e.g. copper) and the molding compound such as epoxy molding compounds (EMC). Several studies were carried out to investigate the influence of different processing parameters or surface treatments on the interfacial bonding. Lee and Park⁸¹ found that the fracture toughness of the lead frame/EMC interface is almost zero between cupric oxide (Cu₂O) and the EMC. However, it increased almost proportionally with the thickness of the cuprous oxide (CuO) layer, until it reached a saturation value at 2 minutes oxidation time. Chung et al.⁸² also found a linear relationship between the CuO content and the adhesion force obtained at the interface. Chan et al.⁸³ examined the influence of moisture levels at elevated temperatures on the interfacial adhesion between copper and epoxy. They found that

the interfacial adhesion decreases as the moisture level increase. They related that to the locking of the water molecules at the epoxy/copper interface.

The examples mentioned above show how crucial the interfacial properties can be in composites. A properly engineered interphase can be the key to enhancing the performance and long-term durability of the whole composite. However, this needs a better understanding of the interphase properties and the different factors that may influence it, which in turn, is dependent on the available methods of characterization and their continuous development.

2.3 Mechanical Characterization of Interphases

A wide range of techniques can be used to characterize the interphase, depending on the type of the required information. This includes microscopic, spectroscopic, thermodynamic and mechanical techniques.⁸⁴ The characterization methods can also be classified more broadly into direct and indirect methods. Indirect methods include single fiber model composite micromechanical test, dynamic mechanical analysis, inverse gas chromatography, differential scanning calorimetry, Raman spectroscopy stress field analysis, Laser Raman spectroscopy, voltage-contrast X-ray photoelectron spectroscopy, acoustic emission and others.^{12,85} On the other hand, direct characterization includes mostly mechanical characterization methods, such as single fiber pull out test, single fiber fragmentation test, nanoscratch test, nanoindentation and atomic force microscopy (AFM) in different operating modes.^{12,86}

Recently, nanoindentation and AFM have been frequently used for interphases characterization, since they are considered to be moderately straightforward methods. Each of the two methods has its own advantages and disadvantages. The two methods are commonly accompanied with FEM, which is being used as a reference for the behavior to be expected from a perfect interface line.⁷⁹ The next sections will explain the two methods and their implementation in interphase characterization, with a primary focus on nanoindentation and the challenges faced when it is applied in the interphase region.

2.3.1 Nanoindentation

In the last few decades, nanoindentation test (also known as depth-sensing indentation) has gained increasing interest due to its ability to assess the material's mechanical properties at the micro and nano scales. This gives the method an advantage when it comes to testing small

volumes,⁹ thin films,¹⁰ or different phases within a material.¹¹ Furthermore, when compared to other micromechanical testing methods, nanoindentation has a relatively simple setup and sample preparation. Since the resulting imprints are very small, nanoindentation is commonly considered a relatively non-destructive test.⁸⁷

The test involves pressing a very small sharp spherical, conical or pyramidal indenter (usually made of diamond) into the material, where the load (P) and penetration depth (h) are being measured simultaneously. The test results in a residual imprint of a certain depth (h_r). The load cycle typically includes applying a certain load, holding at maximum load for a few seconds, and then unloading. During the holding time at maximum load, viscoelastic materials like polymers will exhibit creep, represented by an increasing indentation depth while the applied load is held constant. Figure 2.10 shows typical load functions and the resulting load-displacement curves for different materials, where t_l , t_h and t_u are the loading, holding and unloading times, respectively.

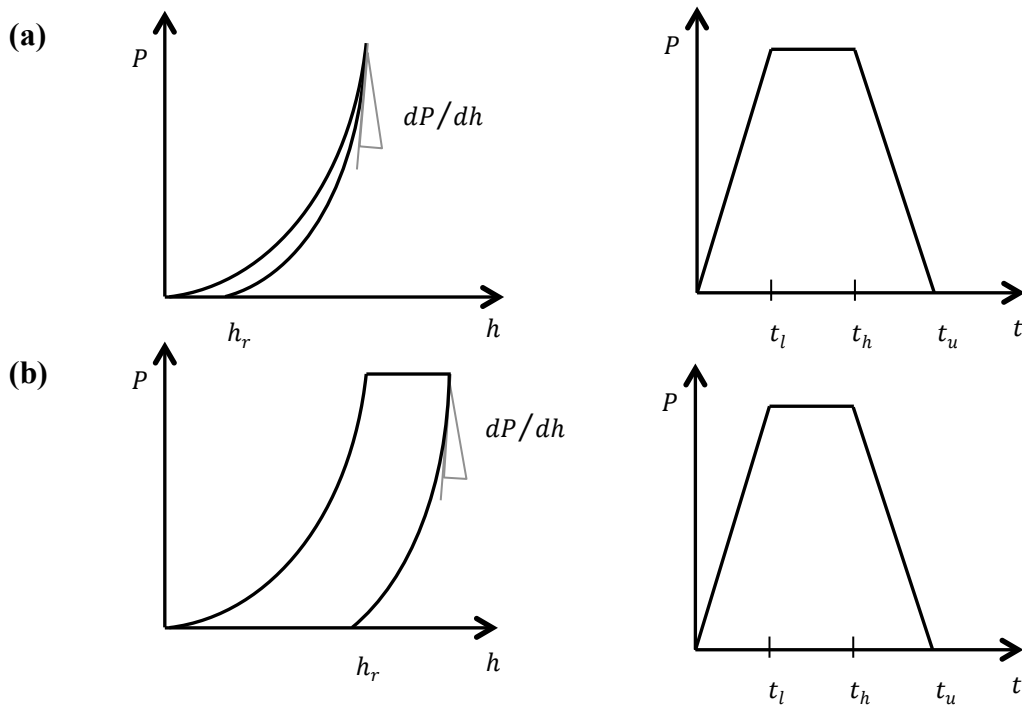


Figure 2.10: Load cycles and the corresponding load-displacement curves for (a) elastic-plastic solid and (b) visco-elastic-plastic solid.

The main differences between nanoindentation and conventional hardness tests are that the applied loads are only in the range of micronewtons to millinewtons ($10^{-6} - 10^{-3}$ N), and the indentation depths are only in the range of nanometers (10^{-9} m). The obtained load-displacement curves can be used for indirect measurement of the contact area at full load,

from which the mean contact pressure, and thus the mechanical properties of the material such as Young's modulus and hardness can be estimated.⁸⁸ The accuracy of the calculated values depends largely on the analysis procedure used to process the raw data and how it accounts for the different systematic errors that are associated with the test. The following few sections will discuss the typical evaluation procedure of the experimental results, and an overview about the common sources of errors will be provided.

Analysis of Nanoindentation Test Data

The analysis of nanoindentation test data in order to obtain materials' elastic and inelastic properties is associated with understanding the contact mechanics between two solid bodies. The first satisfactory analysis for the induced stresses at the contact of two elastic bodies was introduced by Hertz⁸⁹ in 1881, when he found a solution for the elastic contact between two spheres of different radii. A few years later, Boussinesq⁹⁰ studied the stresses and displacements in an elastic body loaded by an axisymmetric rigid indenter using potential theory methods, which later proved to be a breakthrough in understanding the indentation problem. In 1948, and based on Boussinesq's approach, Sneddon⁹¹ derived a load-displacement relationship for a conical indenter, and later, he developed the load-displacement relationship to fit any indenter that can be described as a body of revolution.⁹² His analytical solutions were based on three strict assumptions: (1) the specimen is an infinite half-space, (2) the indenter has an ideal geometry with well-defined parameters (cone, sphere, etc.), and (3) the material is linearly elastic and incompressible. However, during the indentation of a real material, plasticity begins once a critical shear stress is reached underneath the indenter and the loading becomes elastic-plastic.⁹³ Doerner and Nix⁹⁴ modified Sneddon's analysis and applied it to nanoindentation. They observed that on the load-displacement curves, the initial unloading part seemed to be somewhat linear. They hypothesized that during the initial stage of unloading, the contact area between the indenter and the sample remains constant.

Nowadays, the most commonly used analysis for interpreting the load-displacement curves is the one proposed by Oliver and Pharr⁹⁵ in 1992. They showed that the initial unloading behavior is rarely linear and therefore, the contact area is not constant. The unloading curve rather fits to a power law which is represented as:

$$P = \alpha(h - h_f)^m \quad (2.2)$$

where P is the load, h_f is the final displacement at unloading, and α and m are the power law fitting constants. Oliver and Pharr⁹⁵ further provided the following analysis: The stiffness of the elastic contact (S) is the derivative of equation (2.2), dP/dh , calculated at maximum load P_{max} and maximum indentation depth h_{max} as shown in Figure 2.11.

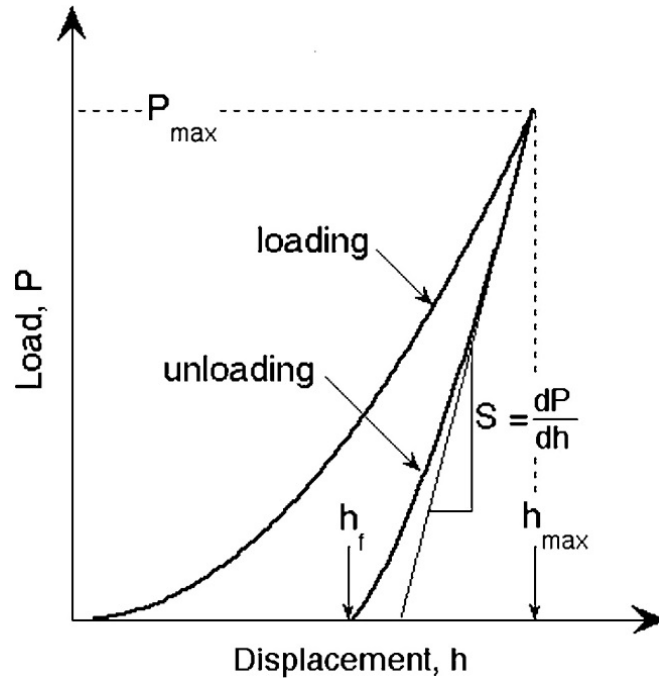


Figure 2.11: Schematic illustration of indentation load-displacement data showing the important measured parameters.⁹⁵

The further procedure used to calculate the elastic modulus (E) and the hardness (H) is based on the unloading process of a conical indenter with a half-included angle $\phi = 70.3^\circ$, which gives the same depth-to-area ratio as a Berkovich indenter. The unloading process is schematically represented in Figure 2.12.

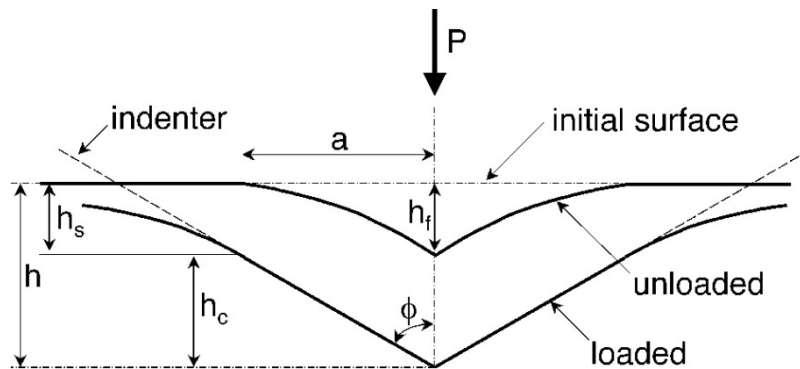


Figure 2.12: Schematic illustration of the unloading process, showing the parameters characterizing the contact geometry.⁹⁵

If the indenter used is a flat punch, the contact stiffness S could be used directly to calculate the surface displacement (h_s). However, for conical or pyramidal indenters, a correction intercept factor (ε) has to be introduced in order to account for the geometry-induced effects. Accordingly, h_s is given by:

$$h_s = \varepsilon \frac{P_{max}}{S} \quad (2.3)$$

Using equation (2.3), and according to the geometry shown in Figure 2.12, the depth along which the contact exists between the indenter and the specimen (h_c) is equal to $h_{max} - h_s$, which translates into:

$$h_c = h_{max} - \varepsilon \frac{P_{max}}{S} \quad (2.4)$$

Based on that, the contact area can be expressed as:

$$A = F(h_c) \quad (2.5)$$

where $F(h_c)$ is an area function that relies on the indenter geometry and describes the projected area of the indenter at a certain distance from the indenter tip. The area functions of the most commonly used indenters as well as the intercept corrections and other important geometrical aspects are represented in Table 2.2. It is important to consider that in reality, these area functions must be calibrated in order to account for the deviations from non-ideal indenter geometry. These deviations can be crucial especially close to the tip.

Table 2.2: Projected areas, intercept corrections and geometry correction factors for various types of indenters.⁸⁸

Indenter type	Projected area	Semi-angle θ (deg)	Effective cone angle α (deg)	Intercept factor ^a ε	Geometry correction factor β
Sphere	$A \approx \pi 2R h_c$	N/A	N/A	0.75	1
Berkovich	$A = 3\sqrt{3}h_c^2 \tan^2 \theta$	65.27°	70.3°	0.75	1.034
Vickers	$A = 4h_c^2 \tan^2 \theta$	68°	70.3°	0.75	1.012
Knoop	$A = 2h_c^2 \tan \theta_1 \tan \theta_2$	$\theta_1 = 86.25^\circ$, $\theta_2 = 65^\circ$	77.64°	0.75	1.012
Cube corner	$A = 3\sqrt{3}h_c^2 \tan^2 \theta$	35.26°	42.28°	0.75	1.034
Cone	$A = \pi h_c^2 \tan^2 \alpha$	α	α	0.727	1

By determining the contact area, it should be possible to calculate the hardness (H) from:

$$H = \frac{P_{max}}{A} \quad (2.6)$$

In addition, and based on its relationship with the contact area and the contact stiffness, the elastic modulus (E) can be calculated using the following equation:

$$S = \beta \frac{2}{\sqrt{\pi}} E_r \sqrt{A} \quad (2.7)$$

where β is another correction factor which accounts for the variations in axial stresses induced by non-axisymmetric, polygonal indenter shapes (see Table 2.2), and E_r is a reduced modulus that was introduced earlier by Hertz;⁸⁹ it accounts for the elasticity of both the indenter and the substrate. The reduced modulus is described as:

$$E_r = \left[\frac{1 - \nu^2}{E} + \frac{1 - \nu_i^2}{E_i} \right]^{-1} \quad (2.8)$$

where E and ν , and E_i and ν_i are the elastic modulus and Poisson's ratio of the sample and indenter, respectively. It is important to notice that equation (2.7) is not limited to a specific indenter geometry.⁹⁶ Despite being originally derived for elastic contact only, it was shown to apply well for elastic-plastic contact as well.⁹⁶

The effective indenter shape was studied by Pharr and Bolshakov⁹⁷ and it is a major factor for understanding the analysis concept behind the model of Oliver and Pharr. They assumed that there is a half-sphere of an elastic-plastic material around a rigid conical indenter as shown in Figure 2.13. With this assumption, every indent of any indenter geometry can be treated as a half-sphere, and the correction factor ϵ is introduced for adjusting the internal stiffness of this half-sphere.

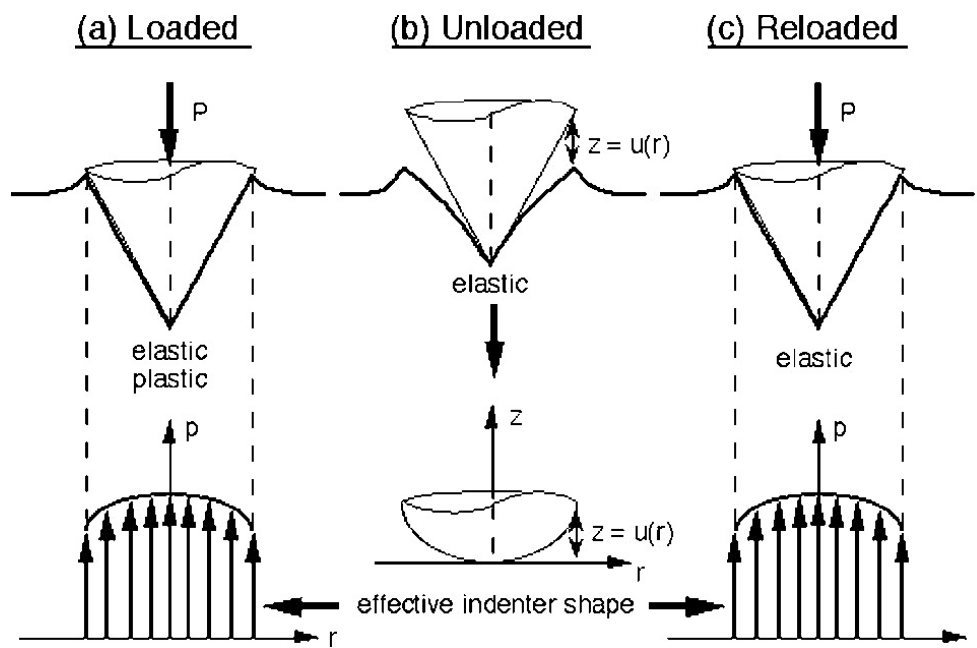


Figure 2.13: Concepts used to understand and define the effective indenter shape.⁹⁷

During loading, both elastic and plastic deformation of the specimen take place and the deformed surface takes the exact shape of the indenter (Figure 2.13a). Simultaneously, a half sphere of compressed material builds up. When the unloading process starts, the deformed material starts retaining part of its shape due to elastic recovery (Figure 2.13b). It should be noted that the indentation shape after unloading is not perfectly conical, but it has a convex curvature instead. If the indenter is reloaded again, a gradual increase in the contact area takes place until full-load is reached (Figure 2.13c). This process should be expected to happen reversely during unloading. This continuous change in contact area is the reason why non-linear unloading curves are obtained from the experiment. The effective indenter shape is described by a function $Z = u(r)$, where $u(r)$ is the distance between the conical indenter and the unloaded deformed surface, while r is the radial distance from the center of contact.⁹⁷

2.3.1.1 Factors Influencing Nanoindentation Test

Various errors could occur during the nanoindentation testing procedure. Some of them appear as offsets from the depth measurements, while others happen because of environmental changes during the test or the non-ideal shape of the indenter. There are also some material related issues such as piling-up or sinking-in. In this section, some of the most common error sources will be reviewed.

Indenters and Real Indenter Shape

In nanoindentation test, the indenter is of a great importance, since it is the part involved directly in the measurement. The indenter shape and material can directly influence the obtained raw data; the indenter stiffness plays a role in determining the reduced modulus, and local adhesion can occur between the tip and the substrate. The indenters used in nanoindentation are usually made from diamond, which is very hard yet very brittle and prone to getting chipped or broken. For the analysis of nanoindentation test data, the elastic modulus value and Poisson's ratio of a diamond indenter are usually assumed to be 1000 GPa and 0.07, respectively.⁸⁸

Common indenter shapes include flat punch, conical, spherical and pyramidal indenters. This last category includes several indenter shapes such as cube corner, Knoop and Berkovich indenters. Each of those indenters has its own advantages, and the choice of the indenter depends on the information to be obtained from the test. For instance, the flat punch requires a relatively simple analysis since the contact area is constant. However, a contact angle might still exist between the indenter and the substrate on a small scale, which can greatly influence the measured data. On the other hand, spherical indenters are known for their smooth transition from elastic to elastic-plastic contact; they are particularly useful when it comes to testing soft materials or replicating contact damage in in-service conditions. Conical indenters have the advantage of being axisymmetric. It is common to treat pyramidal indenters as conical ones with a cone angle that provides the same contact area to depth relationship as the actual indenter, thus allowing using the axisymmetric models to provide solutions for non-axisymmetric indenters.⁸⁸

Berkovich indenter is an example of pyramidal indenters and it is the most widely used indenter for micro- and nano-scale studies. It has an aspect ratio of 1:8 and a face angle of 65.3° , which gives it the same depth to area relationship as the commonly used Vickers hardness indenter. The main difference between the tip shapes of the two indenters is that the Vickers tip is a 4-sided pyramid while the Berkovich tip is 3-sided. The advantage of the Berkovich indenter, however, is that it is easier to achieve a single meeting point for the edges of the pyramid during manufacturing in comparison to the unavoidable line that occurs in other pyramidal indenters. The radius of curvature of the tip is typically smaller than 50 nm for most available commercial indenters.⁹⁸ Thanks to its sharp tip, the Berkovich indenter is also ideal for high resolution in-situ scanning probe microscopy (SPM) imaging. The

geometry of a Berkovich indenter and the corresponding projected area are illustrated in Figure 2.14.

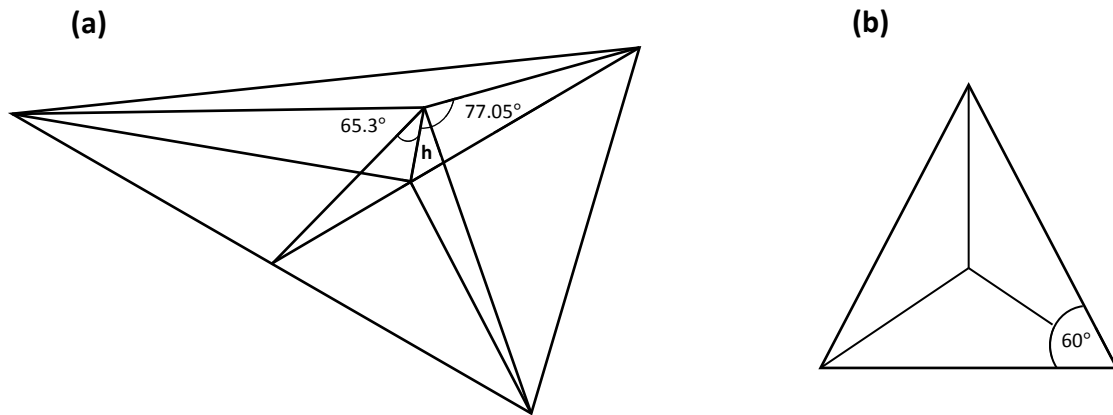


Figure 2.14: (a) Berkovich indenter geometry and (b) the corresponding projected area.

Another important factor to consider when it comes to the indenter used in a nanoindentation test is the real indenter shape. As mentioned before, in nanoindentation the contact area at a certain penetration depth is related to indenter geometry. The values given in Table 2.1 assume that the indenter shape is perfect for all indentation depth, which is not the case in reality. Deviations from the ideal indenter geometry are illustrated in Figure 2.15.

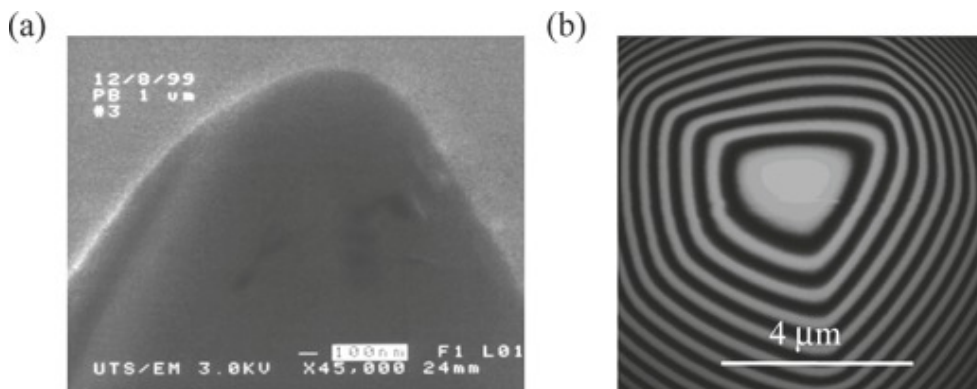


Figure 2.15: (a) SEM image of a nominal 1 μm radius sphero-conical indenter. (b) AFM image showing surface profile of a 10 μm spherical indenter.⁸⁸

In order to take the non-ideal indenter geometry into account, a correction factor could be applied to the equations in Table 2.1. If the actual area of contact is A and the ideal area of contact is A_i , then a correction factor A/A_i should be applied as shown in Figure 2.16. It is noticed that the actual area of contact is usually larger than the ideal one. The error is more pronounced for smaller indentations, since the indenter tip is more prone to wear.

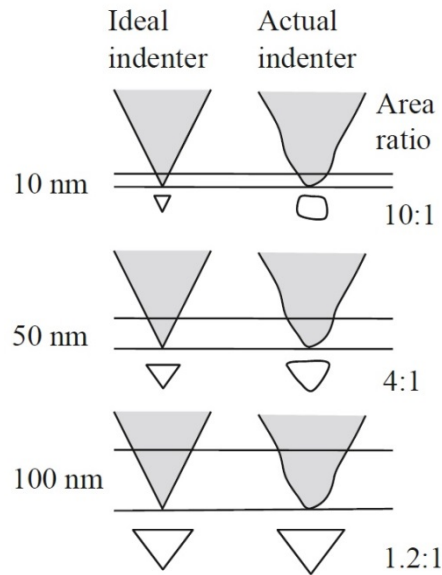


Figure 2.16: Ratios between actual and ideal contact areas at different penetration depths.⁸⁸

A convenient method for applying the area correction factor is to express the contact area as a mathematical function of the depth in the following form:

$$A = C_1 h_c^2 + C_2 h_c + C_3 h_c^{1/2} + C_4 h_c^{1/4} + \dots \quad (2.9)$$

where the first term represents the ideal area function.

Experimentally, the area function can be calibrated by applying indentations at different depths on a material of a known elastic modulus.⁹⁹ The area function could be then plotted versus the indentation contact depth, and a correction factor could be introduced in order to fit the induced area functions so that their processing would lead to the presumed elastic modulus value. In other words, it is the reverse of Oliver and Pharr's analysis, since in this case the elastic modulus is already given and the actual area function at different indentation depths is calculated. This corrected area function can be further used to calculate the elastic modulus of other materials.

Pile-up and Sink-in

In the Oliver-Pharr model, it is assumed that the material is perfectly elastic around the indentation impression. However, in reality, a part of the surrounding material deforms plastically in the form of piling-up or a sinking-in, depending on the material being tested. The flow of material can considerably influence the contact area (Figure 2.17). Errors in

contact area can be as high as 60%.¹⁰⁰ Consequently, a large deviation in the obtained mechanical properties can occur. Fischer-Cripps⁸⁸ reported this behavior in aluminum, where he found that the measured elastic modulus value was much less than expected. Moreover, the time-dependent behavior of a material (viscoelasticity) can also influence the pile-up/sink-in phenomena. For instance, Rar et al.¹⁰¹ found that when the same material is allowed to creep for a longer duration, higher values of sink-in/pile up were obtained.

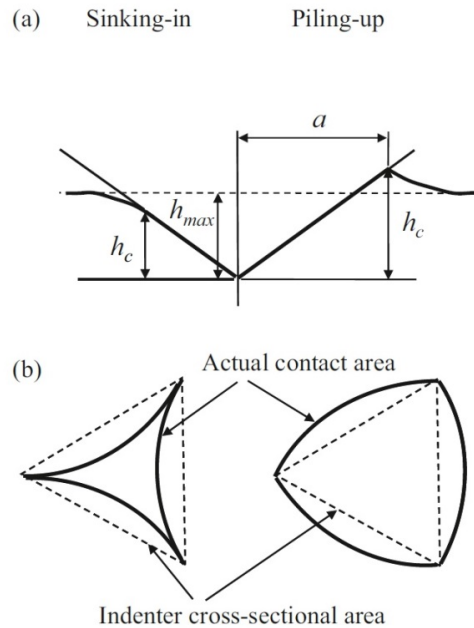


Figure 2.17: (a) Cross-sectional view and (b) plan view for the effect of piling-up and sinking-in on the actual contact area for penetrations of the same depth.⁸⁸

The level of influence of this behavior depends on the ratio between the elastic modulus E and the yield strength σ_y , as well as the strain-hardening behavior of the material. In their study using finite element analysis, Bolshakov and Pharr¹⁰⁰ showed that in the case of non-strain-hardened materials with a high E/σ_y ratio, piling-up occurs and results in a larger effective contact area, while in materials that exhibit strain-hardening and have a low E/σ_y ratio, the material around the indent exhibits sinking-in and a smaller effective contact area is generated. A pile-up parameter can be used to identify the piling-up or sinking-in behavior of the material, which is given by the ratio of the contact depth h_c to the total depth h_{max} .

There are several proposed methods for correcting the error induced by pile-up/sink-in behavior.^{100,102,103} However, if prior information about the mechanical properties of the

sample is available, the error can be corrected using the same method mentioned earlier for correcting the area function.

Machine Compliance

Another important factor that can affect the displacement measurements during a nanoindentation test is the deformation of the instrument itself during the test as schematically illustrated in Figure 2.18.

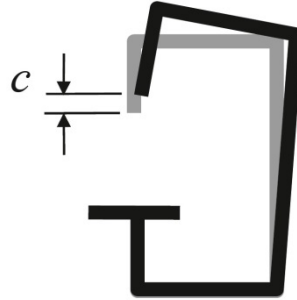


Figure 2.18: Schematic of the effect of load frame deflection by a displacement c during nanoindentation test.⁸⁸

The instrument compliance C_f can be defined as the deflection of the instrument c , divided by the load P . The contact stiffness measured from the unloading curve does not represent solely the specimen response; it also includes a contribution from the instrument. The instrument compliance C_f is influenced by the loading frame, the indenter shaft and the specimen mount. The compliance of the indenter material, $1/S$, is accounted for in the reduced modulus E_r . The specimen/indenter combination and the load frame can be treated as springs in series, where the compliance of each can be added separately to give the total compliance dh/dP measured by the instrument as follows:⁸⁸

$$\frac{dh}{dP} = \frac{1}{S} + C_f \quad (2.10)$$

The instrument compliance can be similarly taken into account using the method mentioned earlier for correcting both the pile-up/sink-in induced errors as well as the indenter shape imperfections, where different loads are applied on a sample of a known elastic modulus, and the value of C_f is adjusted so that the indentations at different depths would give the same value of E .⁸⁸

Creep and Thermal Drift

Thermal drift occurs when the whole nanoindentation system is not in thermal equilibrium because of environmental changes or the heat generated from the involved electronic devices. Such changes may further lead to thermal expansion or contraction while the experiment is running. Since nanoindentation instruments are very large compared to the displacements they measure, errors in measuring indentation displacements arising from thermal drifts could be very pronounced. A drift of only a few nanometers per second over a test cycle which takes only few minutes can introduce large errors to the results.¹⁰⁴ These errors can be avoided by placing the whole system in an insulated or temperature controlled chamber, so that the thermally induced drifts are limited.

On the other hand, deformation caused by creep occurs when viscoelastic materials such as polymers are being tested. This can be noticed when the indentation depth keeps on increasing while the force is held constant (illustrated earlier in Figure 2.10). The creep phenomenon can greatly influence the measured mechanical properties. This influence can be minimized by holding at maximum load for a certain period of time. At the beginning of the test, the creep rate can be several nanometers per second, but after 10-20 seconds, it usually decreases to less than 1 nm/s.¹⁰⁵

2.3.2 Atomic Force Microscopy

Atomic-force microscopy (AFM) or scanning-force microscopy (SFM) is a type of scanning probe microscopy (SPM), which was invented by Binnig et al. in 1986.¹⁰⁶ Since then, it has been widely used as a useful tool for imaging and studying surface interactions by means of force-distance curves.¹⁰⁷ The AFM is based mainly on a cantilever with a microfabricated tip that deflects upon interaction with a sample surface. By moving the sample using a piezo actuator scanner, the cantilever deflection can be measured in order to produce a topography image of the sample surface. The AFM cantilever is typically made of silicon or silicon nitride. It can also be either rectangular or V-shaped.¹⁰⁷

The cantilever deflection can be detected through the interferometric method, the electro tunneling method or the optical lever method which is the most commonly used.¹⁰⁷ In the optical lever method a laser beam is focused on the backside of the cantilever and the reflected beam is detected by means of a position-sensitive photodetector (PSPD) sensor,

which is usually a quartered photodiode. The AFM setup is illustrated schematically in Figure 2.19.

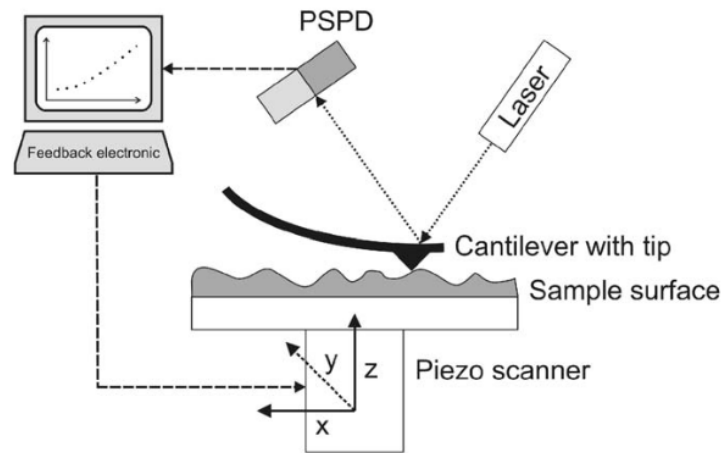


Figure 2.19: Schematic illustration of AFM setup.¹⁰⁸

Due to the extremely small size of the tip, AFM has a very high lateral (25 nm), vertical (0.1 Å) and force (1 pN) resolutions.¹⁰⁷ This allows the AFM to be a powerful tool for investigating different phases within the material as in the case of the interphase. AFM in different operating modes has been used in various studies to investigate the interphase properties. For example, interphases have been investigated by utilizing AFM as a nanoindentation device.^{109,110} Another operating mode that was successfully used to characterize the interphasial properties is the tapping mode phase imaging. In this mode, the AFM tip is oscillated at its resonance frequency, so that at each oscillatory cycle the tip impacts the sample surface briefly and lightly.¹⁰⁸ This technique is particularly useful when it comes to testing soft materials such as polymers, because the tip-sample interactions are much less damaging than in other operating modes.¹⁰³ During the tapping interaction between the probe and the specimen, an amount of energy gets dissipated, which results in a phase lag of the cantilever oscillation relative to the signal sent to the piezo actuator driving the cantilever.¹¹¹ This is called the phase angle and its value is sensitive to the elastic properties of the specimen. The resulting phase angle data can be used to distinguish the different regions with different mechanical properties. For instance, a softer material would result in a bigger phase shift and appear brighter in the phase image.⁵ AFM in force modulation mode (FMM) can also be used to study interphases; it involves an oscillating cantilever tip that indents into the sample surface, which allows obtaining qualitative information about the local sample surface elasticity.¹²

In this work, the AFM force-distance curves will be used to monitor the stiffness variation within the interphase region. A force-distance curve is a plot of the tip-sample force versus the piezo actuator displacement. Figure 2.20a-c shows the plotting of deflection data versus both displacement and time, as well as a schematic illustration of the corresponding piezoelement movements, cantilever deflection and surface deformation.

Figure 2.20a presents an ideal force-distance curve in the conventional trace-retrace manner. The x-axis represents the distance between the tip and the surface, where a larger piezoelement position value means farther distance. Furthermore, it expresses the interaction between the tip and the sample.¹¹¹ The first step is the approach (trace), which is represented by the solid line in Figures 2.20a and b, and where the piezoelement starts moving in the extension direction. Line 1-2 is called the extension zero line and it corresponds to the distance that the piezoelement covers before the sample comes into contact with the tip.

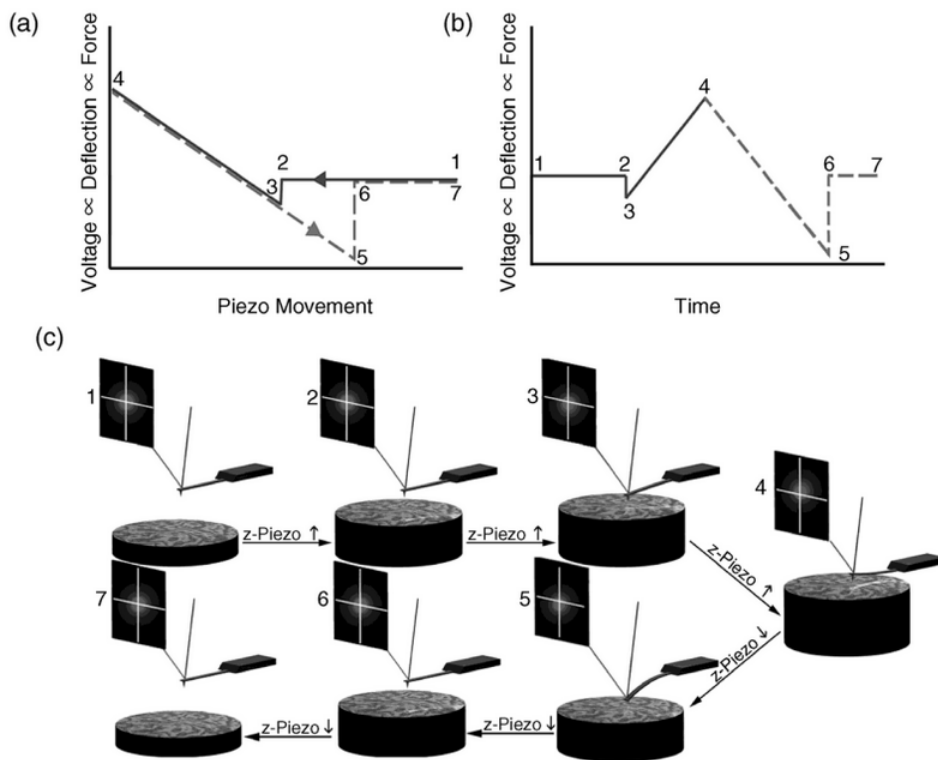


Figure 2.20: (a) An ideal force–distance curve. (b) The deflection data from (a) plotted with respect to time. (c) A schematic explanation of the different regions of the force-distance curve.¹¹¹

At some point, the tip gets attracted to the sample surface and the cantilever bends downwards. This is called the “jump contact” region and is represented by line 2-3. The

piezoelement further moves towards the tip, until the cantilever passes the zero deflection again and starts bending upwards.

Line 3-4 corresponds to the deflection of the cantilever when the tip is in physical contact with the sample surface. This line is linear for purely elastic deformation and its slope is directly related to the surface stiffness.¹¹¹ If the sample is of infinite stiffness, the slope would be 1, as the cantilever deflection is exactly equal to the piezoelement displacement. Point 4 is the point where the approach ends and the retraction starts. Ideally, lines 3-4 and 4-5 will partially overlap and have the same slope during approach and retraction.¹¹¹ Line 5-6 is called the “snap-from contact” region. It represents the adhesion force between the tip and the sample. This line is vertical in ideal cases.¹¹¹ Finally, the cantilever becomes free from contact with the surface and comes to its neutral position as represented by line 6-7.

In AFM measurements, the applied force can be only indirectly measured via the cantilever deflection, which is monitored from the movement of the laser spot on the photodiode. The photodiode sensitivity is expressed in units of nm/V and must be calibrated before each set of measurements. According to Hooke’s law, the cantilever deflection is directly proportional to the applied force via the spring constant which is typically expressed in units of N/m or nN/nm. This spring constant must be similarly calibrated before each set of experiments.

The elastic modulus of the sample can be calculated through processing the obtained force-distance curves in different contact mechanics models such as the Hertzian, Sneddon and JKR models.¹¹¹ However, if the absolute mechanical properties are not required, the stiffness variation can be analyzed by a simple linear fitting of the raw force–distance curves.¹¹² It is also possible to generate a spatial map of force-distance curves collected along the selected surface area by pixel-to-pixel motion, forming what is called a force or stiffness map.¹¹¹

2.3.3 Nanoindentation-AFM Comparison

Although AFM is considered to be a more sensitive technique because of its smaller tip and higher resolution, nanoindentation also has its own advantages in comparison with AFM. In his book, Fischer-Cripps⁸⁸ discusses some drawbacks of AFM which makes the method unsuitable for precise determination of material properties. In an AFM, the tip is usually made from silicon and it has a radius in the order of 5-10 nm. However, the precise geometry of the tip is unknown, since the instrument is designed primarily for imaging where knowing the exact tip geometry is not necessary. Another disadvantage in AFM is that the cantilever to

which the tip is mounted is very compliant in order to provide large deflections in response to surface forces. Therefore, unlike a conventional nanoindentation instrument, when AFM is used to perform nanoindentation test, a large part of the obtained load-displacement curve is accounted for by the compliance of the cantilever instead of the indentation into the sample, the latter being the main signal to be used for nanoindentation analysis. Instrumented techniques such as AFM and nanoindentation employ the conversion of analog data into digital data. In the case of AFM, a considerable loss in the resolution of the signal of interest (the indentation depth) can occur, since it represents only a small portion of the total signal.

Another major difference between AFM and nanoindentation is that in a conventional nanoindentation instrument, the indenter travels vertically, while in AFM it travels slightly tangential to the surface. Therefore, the results measured using AFM include a factor from the tangential penetration that has to be accounted for.¹¹³ In addition, because the indentation depths in the case of nanoindentation are considerably larger than those of AFM, larger deviations in the results are to be expected from AFM as it is more prone to being influenced by the surface roughness.¹¹⁴

3

Finite Element Modeling of Nanoindentation on Epoxy/Copper Interphases

3.1 Introduction

As explained earlier, nanoindentation is very useful when it comes to investigating the mechanical small volumes, thin films, or different phases within the material. Similarly, increasing research efforts are being directed at using nanoindentation to characterize interphases, since it is a relatively straightforward method for assessing the variations in the interfacial mechanical properties. These attempts have been quite successful in the cases where the interphase thickness was relatively large (several micrometers), or when there was no significant difference between the mechanical properties of the different composite constituents (e.g. in polymer/polymer composites).

For example, Munz⁴⁶ used nanoindentation to characterize the interphase between epoxy and polyvinylpyrrolidone (PVP). He found a very large interphase that extended over $\sim 235 \mu\text{m}$. This interphase was divided into three different zones: a zone stiffer than the bulk, followed by an intermediate zone with a stiffness close to that of the bulk, and a final zone that features a wide shallow minimum and levels off at the bulk stiffness. Safavi-Ardebili et al.¹¹⁵ also used nanoindentation to investigate the interphase properties in an epoxy/aluminum system. They indicated an interphase of $\sim 6 \mu\text{m}$ thickness that was harder and stiffer than the bulk.

However, when smaller interphase thicknesses are being investigated (which is usually the case), using nanoindentation to characterize the interphase can be difficult. When nanoindentation is performed, a stress field develops underneath the indenter. This stress field is associated with the formation of a plastic deformation zone of width W_{pl} as illustrated schematically in Figure 3.1.¹¹⁶

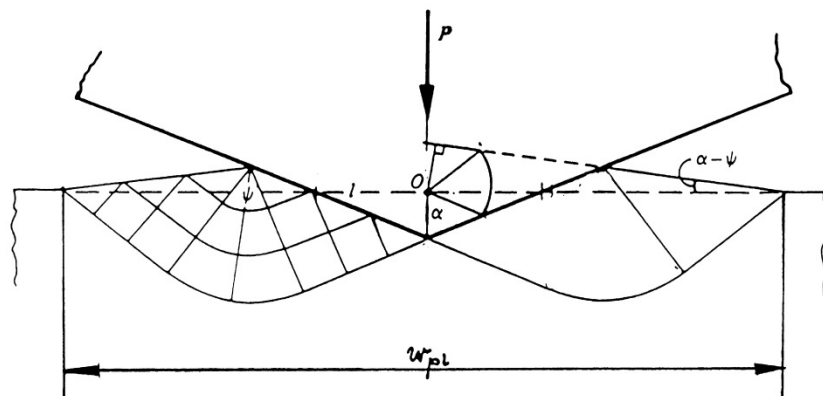


Figure 3.1: Plastic deformation zone of width W_{pl} , created by an indenter pressing into a ductile material.¹¹⁶

Hodzic et al.¹⁵ studied the lateral extent of the formed stress zone. They reported that the width of the stress zone is approximately twice as wide as the indentation width. For a Berkovich indenter and based on its geometry, the indentation width is given by:

$$s = 2h(\tan 65.3^\circ)/(\tan 30^\circ) \quad (3.1)$$

where s is the width of indentation and h is the indentation depth. They suggested that the creation of the plastic deformation zone and the corresponding stress field could be affected by the presence of interfaces, inclusions, or an interphase with distinct properties from those of the matrix. When indentations are applied in the bulk matrix at large distances from the interface, the influence of these interactions is negligible. However, in the vicinity of the interface, and because of the significant difference in the elastic moduli of the two constituents (the matrix and the reinforcement), the constriction on the development of the plastic zone becomes more pronounced. This can result in higher stiffness and hardness values than the bulk. This phenomenon is called the ‘boundary effect’, and it leads to a difficulty in distinguishing solely the interphasial mechanical properties.

This problem was reported in various studies performed on different composite systems. Kumar et al.¹⁴ used nanoindentation to investigate the interphase in an epoxy/fiber glass system. They suggested the presence of a fiber bias effect, which was confirmed by applying indentations in the presence and absence of a fiber. They found that this effect was proportional to the indentation loads used; lower loads helped minimize the fiber bias effect. Furthermore, they found that cutting the sample surface at an angle to the fiber axis helped as well in reducing the fiber bias effect. Gao and Mäder¹² also suggested using low indentation forces in order to avoid the boundary effect. The fiber bias effect was also reported by Yedla et al.¹¹⁷ in their investigation of the interphase in silane coated glass fiber-reinforced polyester matrix composites. They used both a Berkovich indenter and a parabolic tungsten indenter and found that using the latter eliminated the fiber bias effect. Downing et al.¹¹⁸ used nanoindentation to examine the mechanical properties of the interphases in PMCs. They found a stiffness gradient across the interface, but they suggested that it was caused solely by the relatively stiff fiber. When they removed the fiber by chemical etching, that gradient reversed itself. They concluded that nanoindentation was not adequate for measuring the actual interphase properties.

In their work, Lee et al.¹³ tried to investigate the mechanical properties of the interphase in a cellulose fiber-reinforced polypropylene composite using nanoindentation. They found an interphase of around 1 μm thickness. However, three-dimensional finite element analysis showed that a perfect interface without property transition has almost the same width as the one measured by nanoindentation. The boundary effect was confirmed when they applied indentations of different depths at a certain distance from the interface and obtained increasing elastic modulus and hardness values as shown in Figure 3.2. They concluded that using the existing nanoindentation techniques, it would be difficult to calculate the exact mechanical properties without the effect of neighboring material properties in a region that is at least 8 times smaller than the indent size.

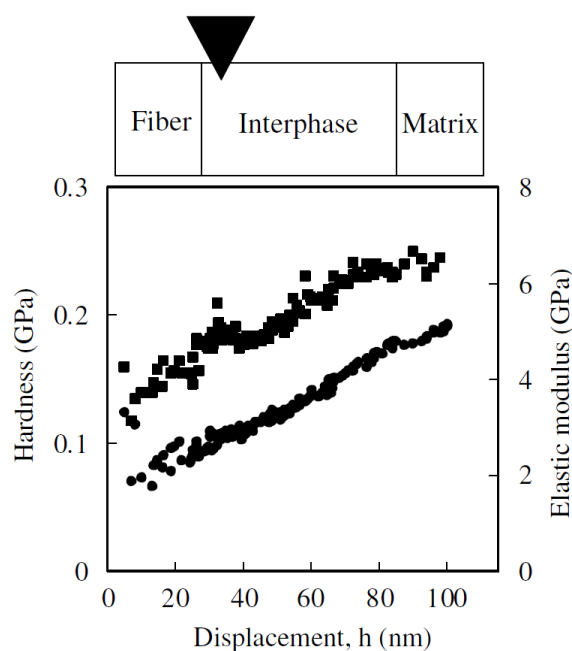


Figure 3.2: An increase of hardness (●) and elastic modulus (■) with indentation depth in nanoindentation made in close proximity to the fiber.¹³

The boundary effect exists in polymer/metal composites as well. It was studied by Li et al.¹¹⁹ in their investigation for the interphase properties in epoxy-aluminum joints. In order to determine the extent of the boundary effect, they applied indentations at different distances from the interface line using a conical indenter, and monitored the point at which the softer material (epoxy) is stiffened due to the restriction of the neighboring harder phase (aluminum). They defined the distance between this point and the interface line as the radius of the indent affected zone (IAZ). The IAZ was reported to be significantly larger than the surface radius of the indenter and it increases with the indent depth.

In this study we propose a system that would allow using nanoindentation for investigating the size and properties of the interphase between a polymer and a metal (e.g. epoxy and copper) while avoiding the boundary effect, or at least distinguishing the variations in mechanical properties caused by the interphase from those caused by the stiffness of the metal. The concept of this system is based on an epoxy/Cu/epoxy sandwich structure, which is prepared in a way that allows having the interphase between the copper and only one epoxy side. Moreover, the thickness of the copper layer is only 100 nm or less. We hypothesize that when the copper is made very thin, it would not cause constriction on the indenter or on the formation of the deformation zone around it. In addition, even if such constriction happens, the side of the epoxy that does not include an interphase with the copper can be used as a reference for detecting the IAZ. The system will be explained in detail in the following sections.

In this chapter, the proposed system will be verified using FEM. FEM is a numerical method for solving partial differential equations (PDEs). It is a commonly used technique among engineers nowadays. In different engineering problems, it is important to develop a mathematical model to describe the behavior of a system under certain conditions. This model can be further used as a reference, when the system is exposed to those conditions experimentally. Within FEM, the system is broken down into smaller elements that are connected together by nodes. By formulating an algebraic expression for each of these nodes, an approximate solution can be generated for the whole system.

3.2 Experimental Work

In the present work, the indentation procedure is simulated by a static structural analysis using the Mechanical APDL of ANSYS Workbench 16.1. It is assumed that the material is isotropic and linearly elastic. Since the main aim is to verify the validity of the represented model geometrically rather than investigating the exact material behavior, the materials properties were assumed to be elastic; the plasticity and time-dependent properties were not accounted for.

Geometry

A 3D model was used to simulate the proposed nanoindentation system. The model was drawn using DesignModeler provided by ANSYS Workbench. The Berkovich indenter was

drawn by extruding a square with a side dimension of $5\ \mu\text{m}$ and extrusion depth of $2.5\ \mu\text{m}$. Three slices were then cut at three planes with angles of 0° , 120° and 140° to the y-axis, and a 65.3° angle to the x-axis, resulting in the geometry shown in Figure 3.3.

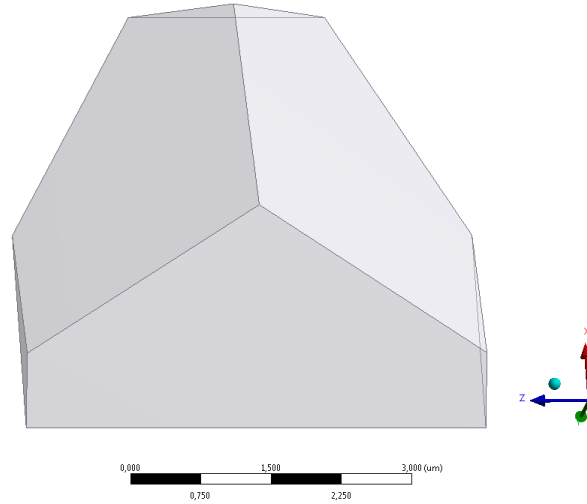


Figure 3.3: Geometry of the Berkovich indenter used in the simulation.

The epoxy/Cu/epoxy system with a perfect interface is shown in Figure 3.4. The two epoxy sides (namely epoxy A and epoxy B) were drawn by extruding a rectangle with the dimensions of $10\ \mu\text{m} \times 20\ \mu\text{m}$ and an extrusion depth of $10\ \mu\text{m}$, while the copper was inserted in between using the same dimensions but a thickness of only $100\ \text{nm}$.

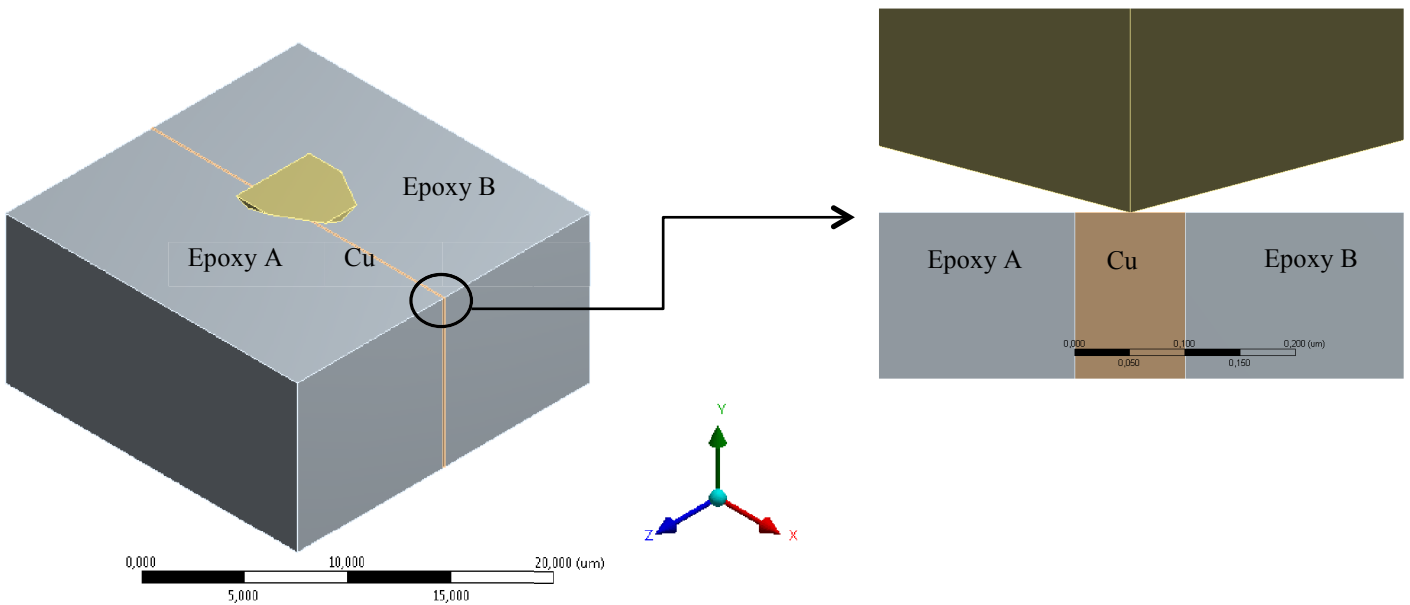


Figure 3.4: Geometry of the epoxy/Cu/epoxy system.

For modeling the same system in the presence of an interphase (IP) in one of the two epoxy parts (epoxy B), another rectangle was extruded between the copper and epoxy B, with the same dimensions in the x and y axes, and a thickness of 400 nm as illustrated in Figure 3.5. A 400 nm thick interphase was selected based on Chung et al.,⁵⁸ who reported an interphase extending over 1.9 μm between copper and epoxy, with a 400 nm region next to the copper interface exhibiting lower stiffness than the bulk.

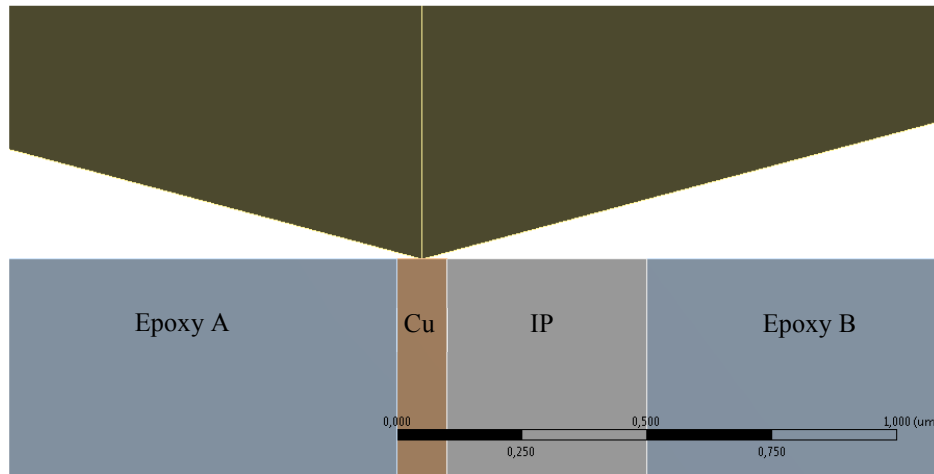


Figure 3.5: Geometry of the epoxy/Cu/epoxy system with an interphase (IP) in only one of the two epoxy sides.

Material Properties

As mentioned before, the whole system was assumed to be purely elastic for simplification; all materials were defined as isotropic linearly elastic. The materials properties are provided in Table 3.1. The epoxy properties were determined by a tensile test, while the copper values were previously measured by nanoindentation. The interphase between copper and epoxy was reported to be softer than the bulk epoxy in a previous study. Therefore, the mechanical properties of the interphase were assumed accordingly.⁵⁸

Table 3.1: Materials properties used for modeling.

Material	Elastic Modulus (GPa)	Poisson's ratio
Epoxy	3.4	0.35
Copper	35	0.3
Interphase	1	0.35
Diamond (Indenter)	1000 ⁸⁸	0.07 ⁸⁸

Mesh

The model was meshed with tetrahedral elements using a patch conforming algorithm. The element size inside the copper was chosen to be $0.25\ \mu\text{m}$ and the rest of the model elements were adjusted accordingly (Figure 3.6). Since the region around the indenter tip is the main region of interest, it was meshed using a sphere of influence with a radius of $0.4\ \mu\text{m}$ and element size of $15\ \text{nm}$ as shown in Figure 3.7.

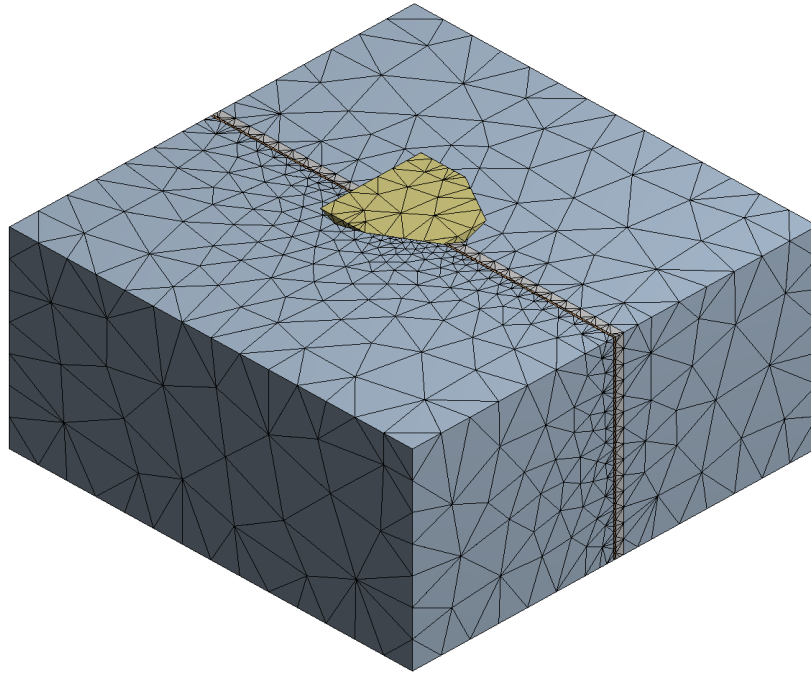


Figure 3.6: Meshing of the system with a finer mesh around the copper.

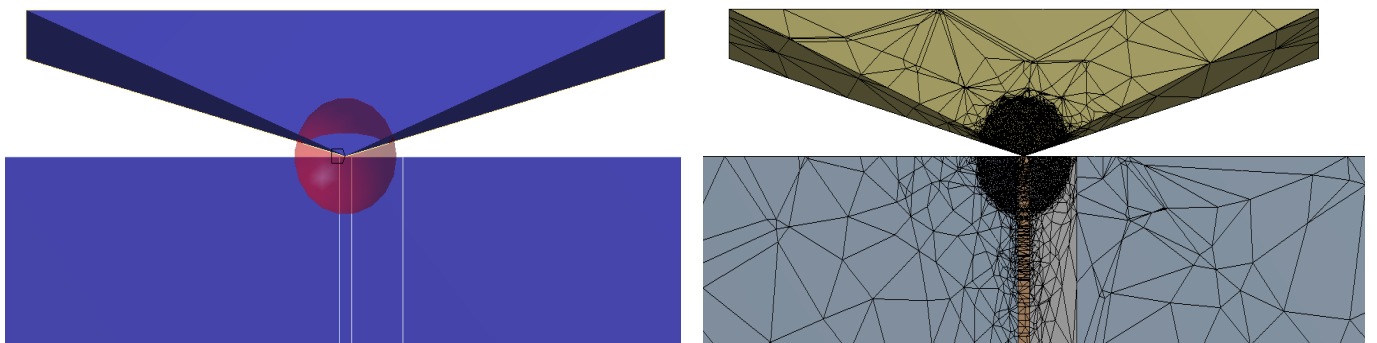


Figure 3.7: Finer meshing around the indenter tip using the sphere of influence meshing method.

Contact

Frictionless contact was defined between the three sides of the indenter and the upper surface of each of the epoxy parts, the copper and the interphase.

Boundary Conditions

The base and the four sides of the system, including the sides of the epoxy, the copper and the interphase are constrained by fixed boundary conditions; i.e. all sides except the surface. The nodes of those sides cannot move in any direction. All the nodes on the upper surface of the indenter are coupled together, so that they would all have the same displacement in the y-direction.

Load Step and Sub Steps

Since only the elasticity of the system is taken into account, only one load step was applied (the loading and unloading are identical). The loading process in nanoindentation was simulated by increasing the indenter displacement along the y-axis in small increments, until it reaches the required maximum indentation depth from the point of contact with the bulk material. The maximum number of sub steps was 100, while the actual number of sub steps was either 10 or 8, depending on the final indentation depth to be reached.

3.3 Results and Discussion

Investigating the Mechanical Properties around a Perfect Interface

The first hypothesis regarding the proposed system is that when the copper is introduced in a relatively small thickness (100 nm), it would not have a pronounced constriction influence on the indentations in its vicinity. In order to investigate this, indentations of 150 nm depth were applied at different distances from the center of the copper layer, ranging from 0 to 1 μm with 200 nm increments, followed by a further indent at a distance of 2 μm . This procedure was applied to the epoxy/Cu/epoxy model with a perfect interface; i.e. without involving an interphase. The indentations were performed on both sides of the copper and the resultant indentation forces were calculated by ANSYS. Figure 3.8 shows a plot of the different force-

displacement curves obtained by the indentations applied at different distances from the copper.

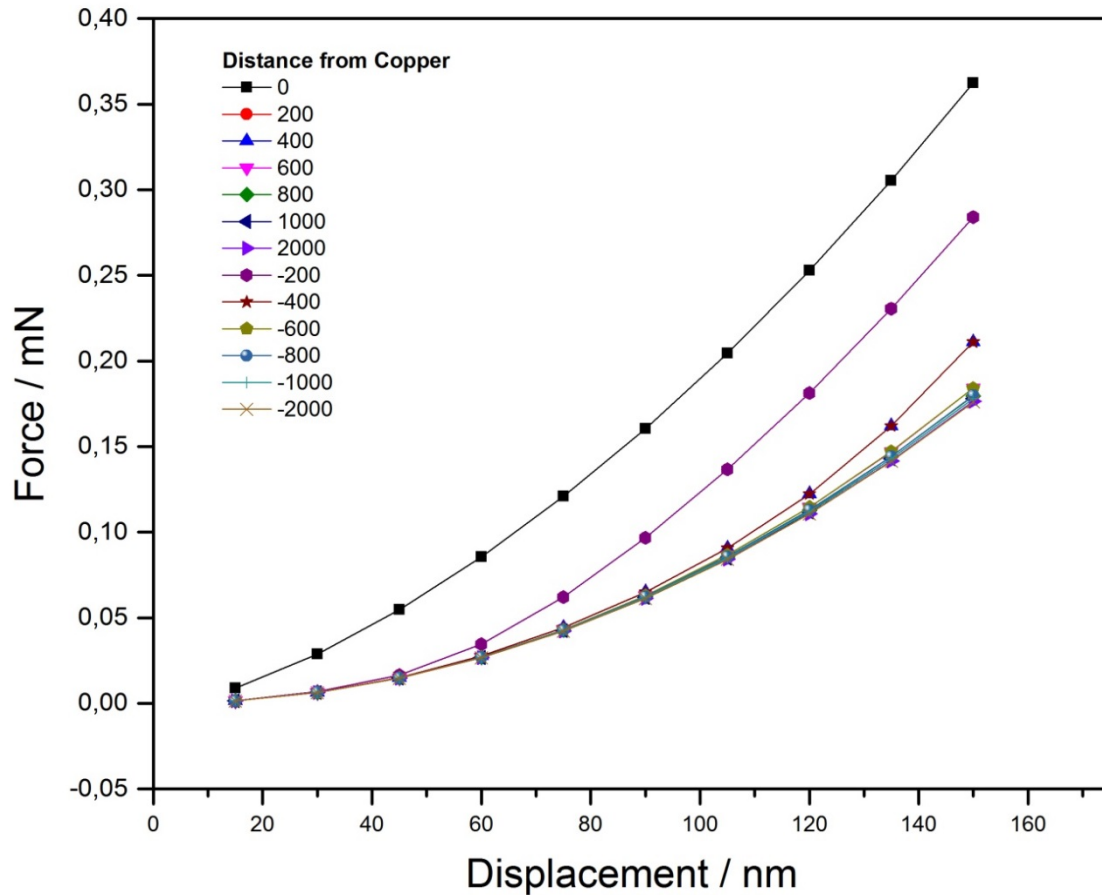


Figure 3.8: Force-displacement curves of 150 nm deep indents, applied on both sides of a perfect epoxy/Cu interface at different distances.

The first thing to be noticed from this plot is that because of the symmetry of the problem (Figure 3.4), the force-displacement curves resulting from the indentations performed on both epoxy sides at equal distances from the copper coincide. Moreover, the indentations applied on the center of the copper or close to it resulted in considerably higher forces than those generated by indentations farther from the copper. This influence was clear until a distance of 400 nm from the copper, after which the force values started getting closer to each other. These curves suggest that the copper does have a mechanical influence on the indenter even with such a small thickness. For a more detailed analysis, the curves were analyzed using Oliver-Pharr method; the slope of the upper part of the curves between the last 3 sub steps was used to obtain the contact stiffness needed for the analysis. Figure 3.9 shows the calculated apparent elastic modulus values corresponding to the indentations at different

distances from the center of the copper. An apparent elastic modulus is used, since the measured elastic modulus includes contributions from different phases.

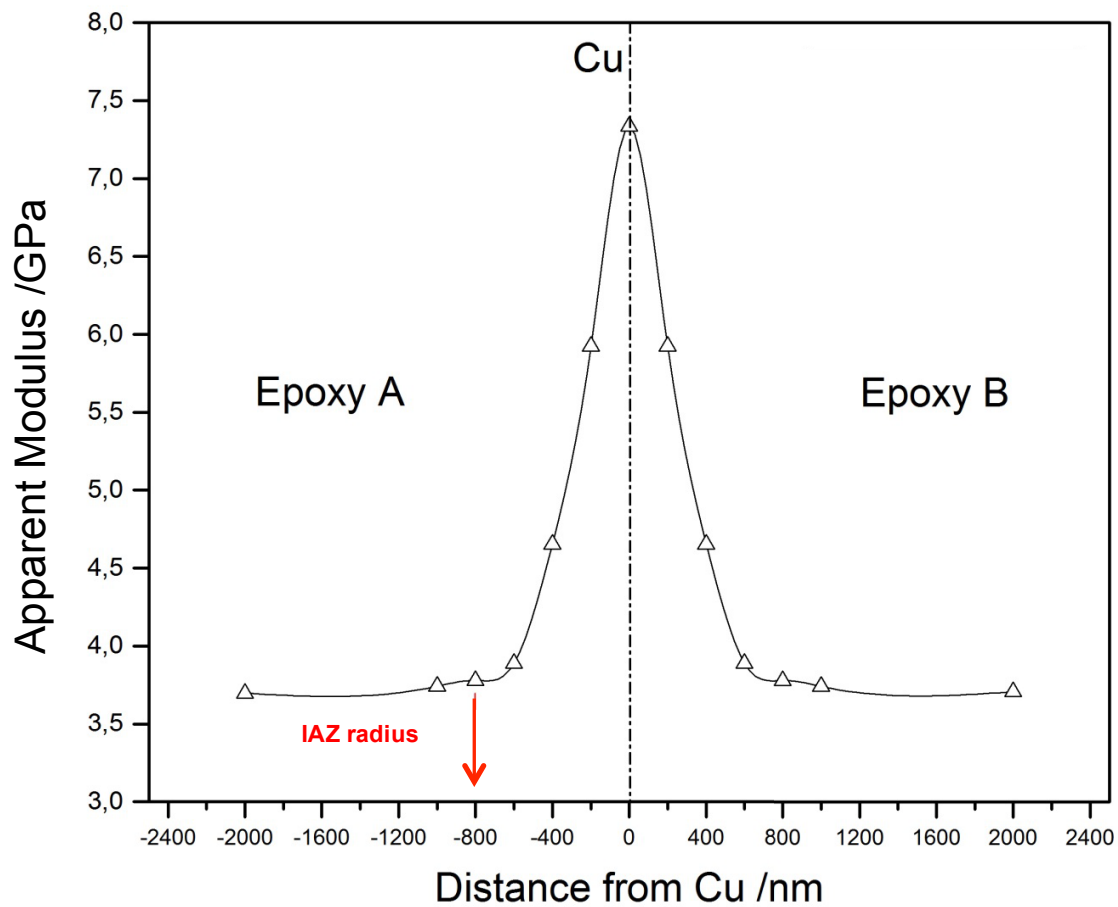


Figure 3.9: Variation of the elastic modulus values with distance from copper using 150 nm deep indentations.

Figure 3.9 clearly shows the influence of the copper on the indentations performed in its vicinity. The apparent elastic modulus value is almost constant for indentations at 1 μm from the copper and further. However, as the indentations get closer to the copper, the value of the elastic modulus starts increasing until it reaches its peak at the copper, where it becomes approximately two times higher than the value of the bulk epoxy. This behavior means that even with a thickness of only 100 nm, the copper is stiff enough to constrain the indentations in its vicinity. This agrees with several other studies that showed that the mechanical property variations around the interface are caused mainly by the boundary effect and not solely the interphase.^{12-14,109} The boundary effect starts to be significant at around 800 nm from the copper and closer, which means that at 800 nm, the indenter (or at least the stress zone accompanying it) starts touching the copper layer. This point can be used to determine the

radius of the IAZ. Figure 3.10 shows a plane section of the indentation performed at 800 nm from the copper as well as the associated stresses. It can be seen that at a distance of 800 nm from the copper, although the indenter itself is not touching the copper, the associated stress zone starts interacting with the copper. That is why the value of the elastic modulus in Figure 3.9 starts increasing at 800 nm from the copper. Therefore, in the proposed model and for indentations with a depth of 150 nm, the IAZ radius is ~ 800 nm.

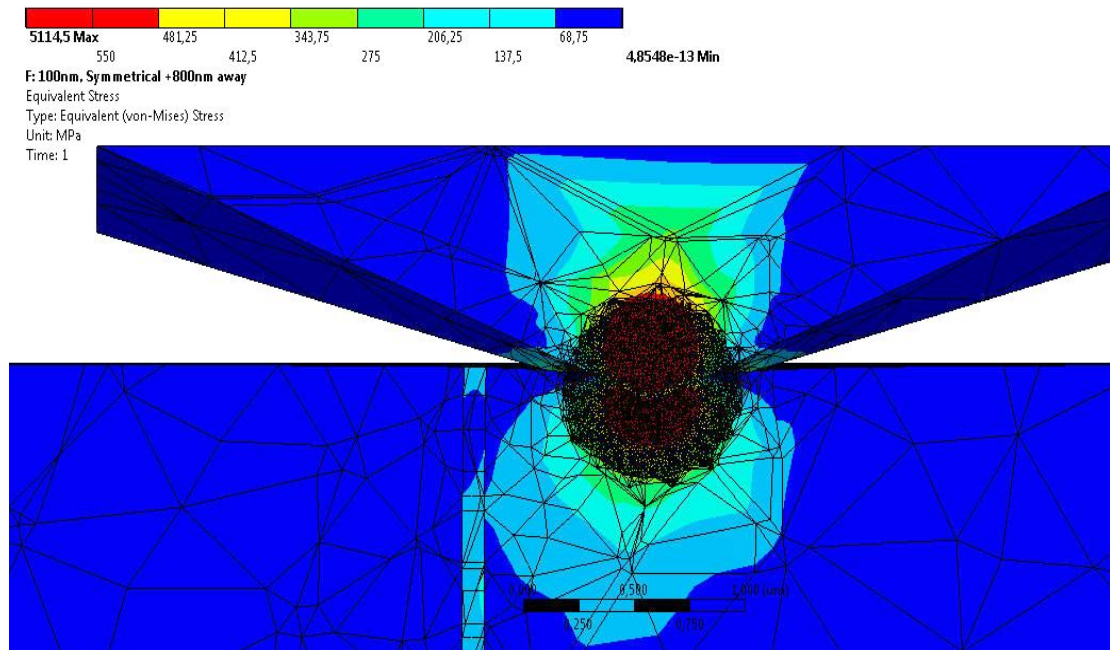


Figure 3.10: The von-Mises stresses accompanying a 150 nm deep indent, applied 800 nm away from the copper.

Inserting an Interphase

The second hypothesis regarding the proposed model is that even if the copper is having a constriction effect on the indentations in its vicinity, it should be possible to determine and exclude the extent of this effect from the interphase investigation, by having the interphase on only one side of the copper, while using the other side as a reference. To verify this hypothesis, a lower stiffness region with a thickness of 400 nm was introduced at the interface between the copper and epoxy B as shown earlier in Figure 3.5. The same indentation procedure was applied, as in the case of the pure interface; performing indentations of 150 nm depth with 200 nm increments away from the copper on both sides. More indentations were applied on the side of epoxy B (where the interphase is), since it is the side of interest. The resulting force-displacement curves are shown in Figure 3.11.

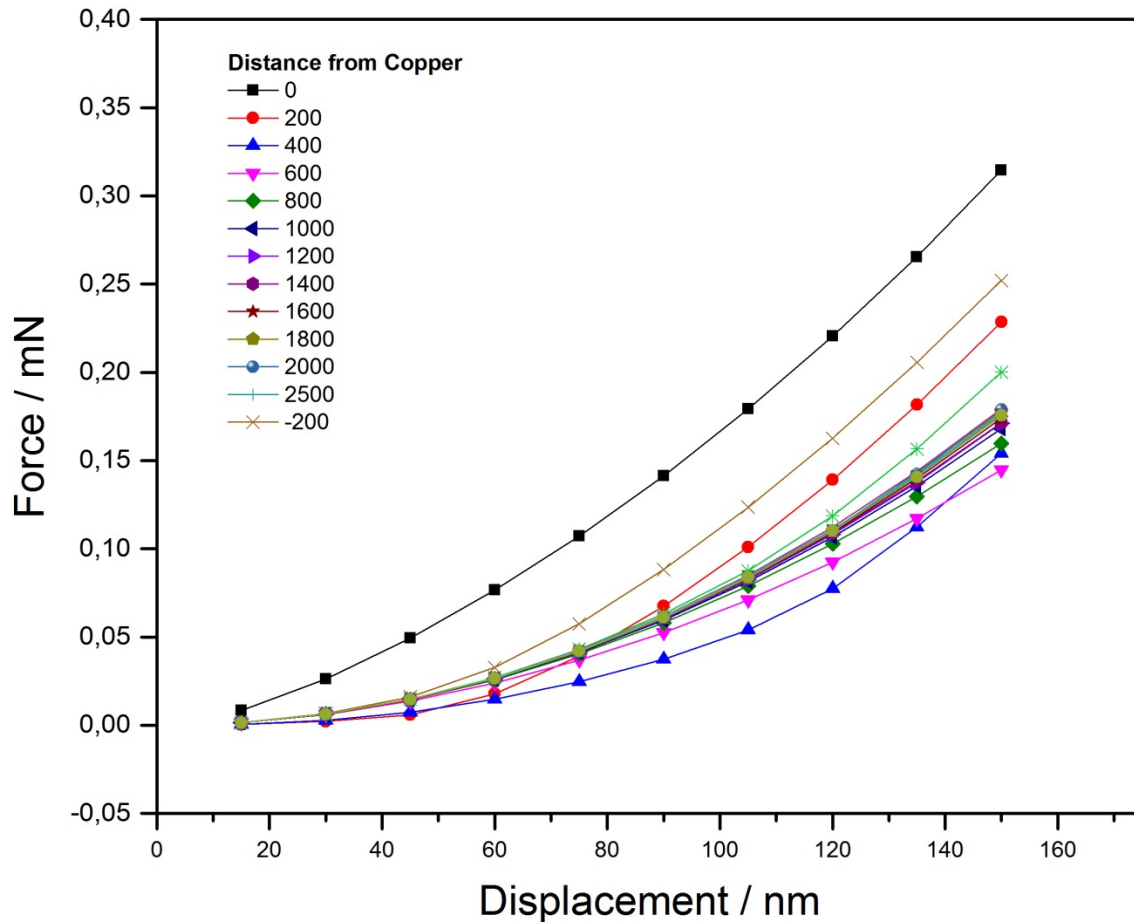


Figure 3.11: Force-displacement curves of 150 nm deep indents applied on both sides of copper, where a softer interphase with the epoxy is present in only one side.

The force-displacement curves show an obvious deviation from the ones obtained in the case of the perfect interface (Figure 3.8), which suggests a considerable influence caused by the introduction of the interphase. These curves were further analyzed using Oliver-Pharr method, where the upper part of the curves between the last 3 sub steps was used to obtain the contact stiffness needed for the analysis. Figure 3.12 shows a plot of the calculated apparent elastic modulus values corresponding to the indentations at different distances from the center of the copper. The arrow shows the direction of indentation, while the diagram at the x-axis shows the corresponding materials of the model and their thicknesses; epoxy A has a perfect interface with the copper, then a 100 nm layer of copper, followed by a soft interphase of 400 nm thickness between the copper and epoxy B.

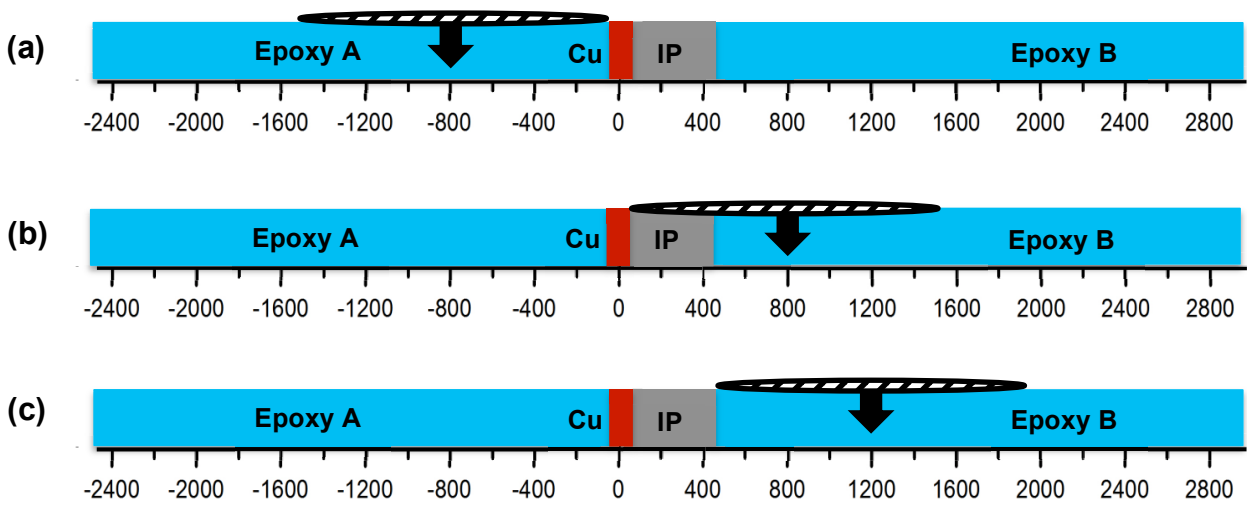
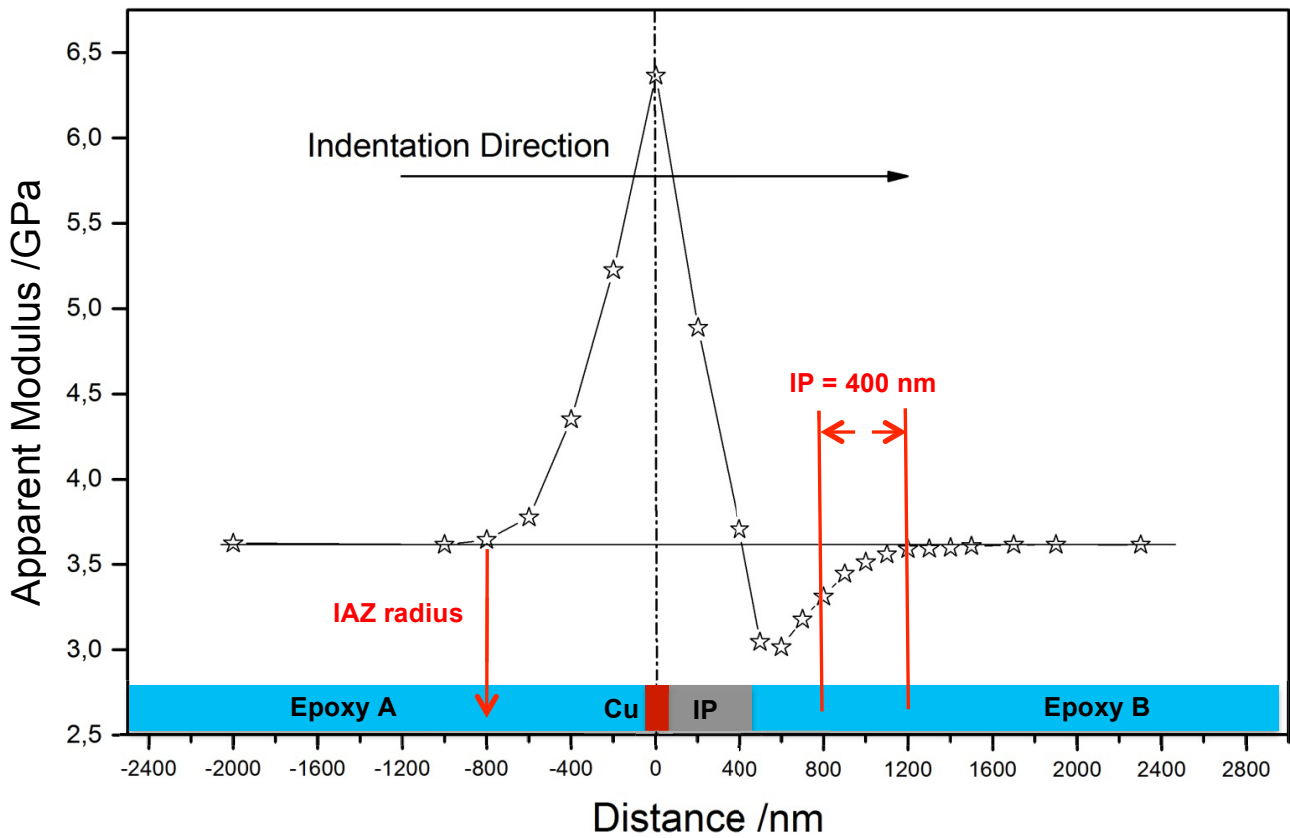


Figure 3.12: Variation of the elastic modulus values with the distance from copper in an epoxy/Cu/epoxy system with an interphase on only one side of the copper, using 150 nm deep indents. The diagrams below show the IAZ at the points when it (a) starts touching Cu, (b) stops touching copper and starts touching the IP only, and (c) stops touching the IP.

In the plot above, and when compared to the modulus variations in the case of a perfect interface (Figure 3.9), an additional region in epoxy B can be seen where the values of the apparent modulus decrease significantly. This is a result of introducing a soft region representing the interphase. Similar to the case of the model with a perfect interface, at a distance of 800 nm to the left of the copper (Epoxy A region), the value of the apparent modulus starts increasing from the bulk epoxy value, which means that the copper starts to restrict the formation of a stress zone around the indenter. This point is considered a reference for determining the IAZ, which is represented in Figure 3.12a.

By mirroring this point to the other side of the copper where the interphase exists (Figure 3.12b), it would translate into the point where the IAZ is not touching the copper anymore. Therefore, starting from this point, the IAZ is interacting with the interphase only. This means that starting from this point, any variations in the apparent elastic modulus on the plot are caused solely by the interphase. By tracing the variation in the apparent modulus value from this point until it becomes constant again at the bulk, it should be possible to determine the thickness of the interphase. The point at which the apparent elastic modulus value becomes constant again on the plot is 1200 nm, which is represented in Figure 3.12c as the point where the IAZ stops touching the interphase. By subtracting the distance between this point (1200 nm), and the point where the IAZ stops touching the copper (800 nm), the interphase thickness can be calculated as 400 nm, which is the correct thickness that was provided in the model.

Figure 3.12 shows the apparent modulus value hits a minimum at around 600 nm from the copper at the side of epoxy B. Figure 3.13 shows this indentation as well as the associated stresses. It could be seen that the indenter is quite large in comparison to the phases in question. Although the interphase provides a maximum contribution to the measured value at this point, this value is not a result of the interphase only and cannot be used to determine the absolute mechanical properties within the interphase. This explains the difference between the apparent elastic modulus value measured at this point (~3 GPa) and the provided value for the model (1 GPa).

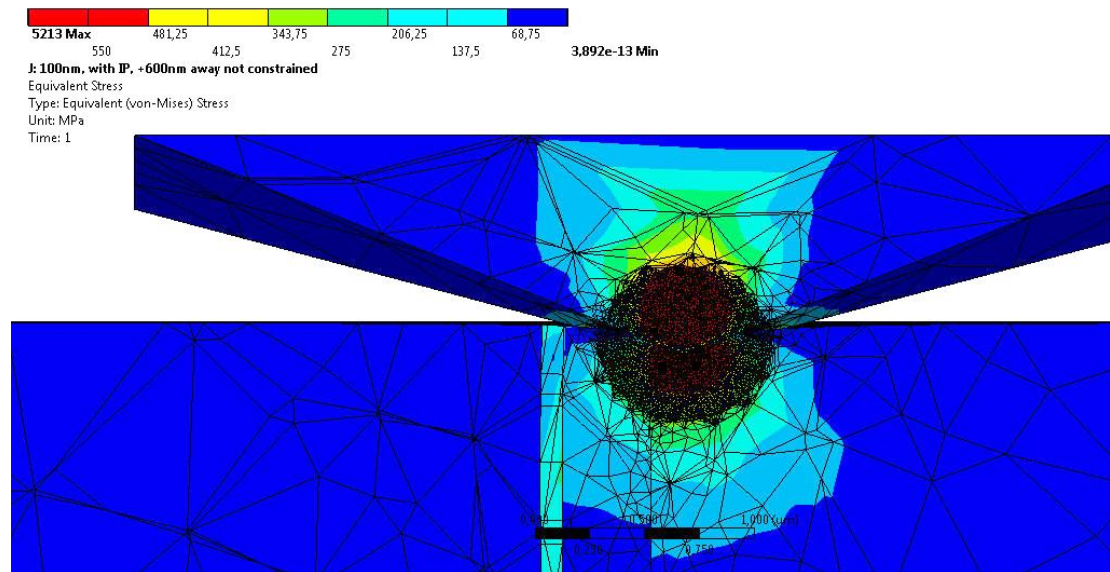


Figure 3.13: The von-Mises stresses accompanying a 150 nm deep indent applied at 600 nm distance from the copper in the presence of a 400 nm interphase.

Influence of Indentation Depth

Although it might not be possible to use the proposed model to determine the exact properties within the interphase region due to the relatively large size of the indenter, this model would still be quite useful in determining the thickness of the interphase as well as its relative behavior with respect to the bulk (e.g. if it is softer or harder than the bulk). Moreover, by performing smaller indents, the IAZ gets smaller as well, and the contribution of the interphase only among the other phases in the system should be more pronounced. In order to investigate this, another series of indents with an indentation depth of only 60 nm was applied to the same model. In this case, the indentations were applied along a distance of 1 μm from the copper, on both epoxy sides, with smaller spaces (100 nm) between the indentations on the side of epoxy B, since it is the side where the interphase lies. The resulting force-displacement curves are shown in Figure 3.14.

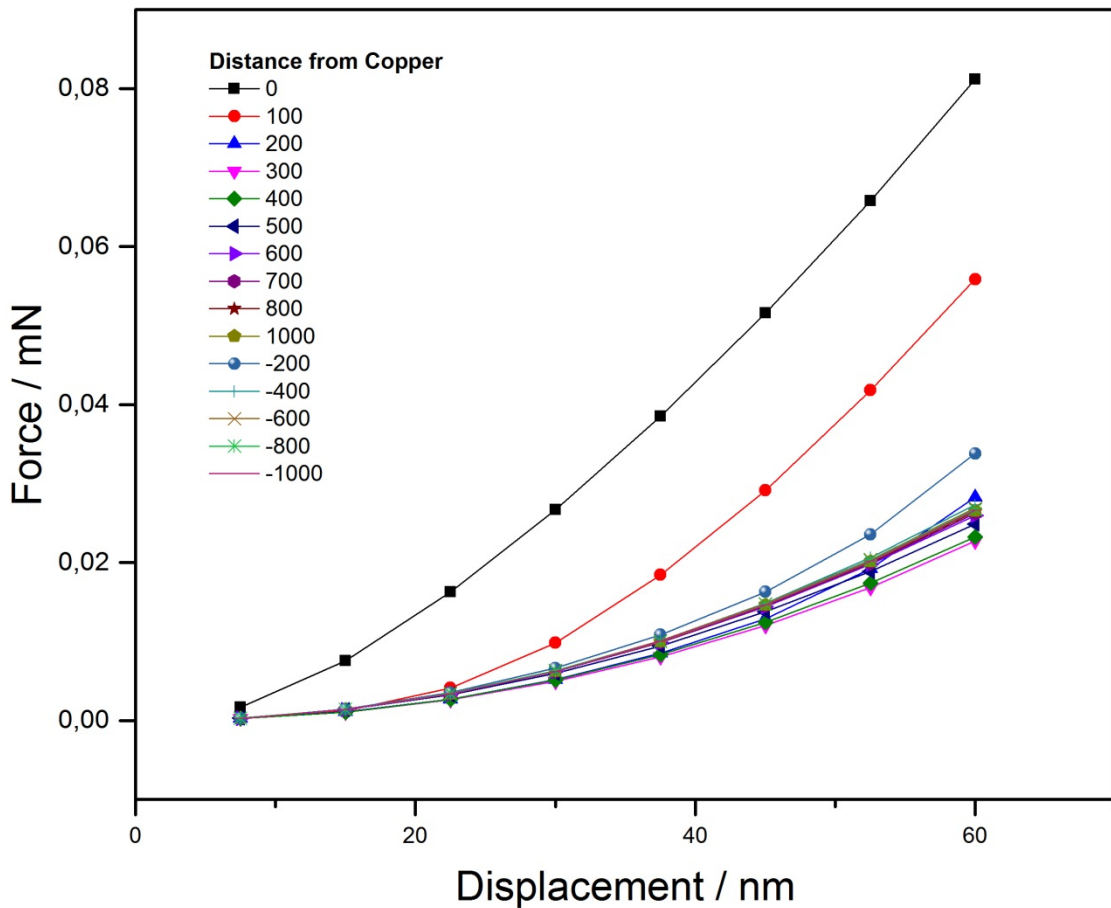


Figure 3.14: Force-displacement curves of 60 nm deep indents applied on both sides of copper, where a softer interphase with the epoxy is present in only one side.

The force-displacement curves shown above were further analyzed using Oliver-Pharr method. Similarly, the upper part of the curves between the last 3 sub steps was used to obtain the contact stiffness needed for the analysis. Figure 3.15 shows a plot of the calculated apparent elastic modulus values corresponding to the indentations at different distances from the center of the copper. The arrow shows the indentation direction, while the diagram at the x-axis shows the corresponding materials of the model and their thicknesses; epoxy A has a perfect interface with the copper, then a 100 nm layer of copper, followed by a soft interphase of 400 nm thickness between the copper and epoxy B.

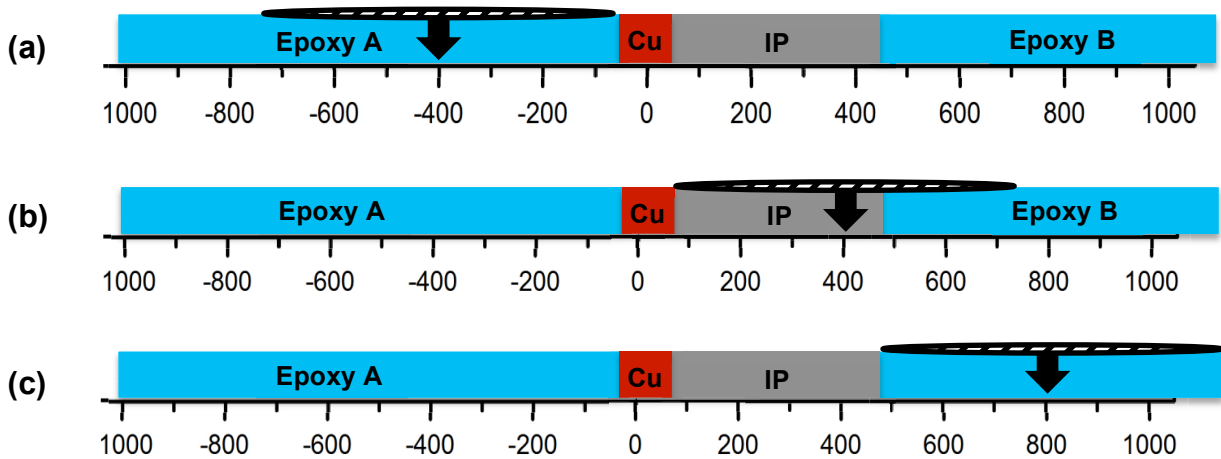
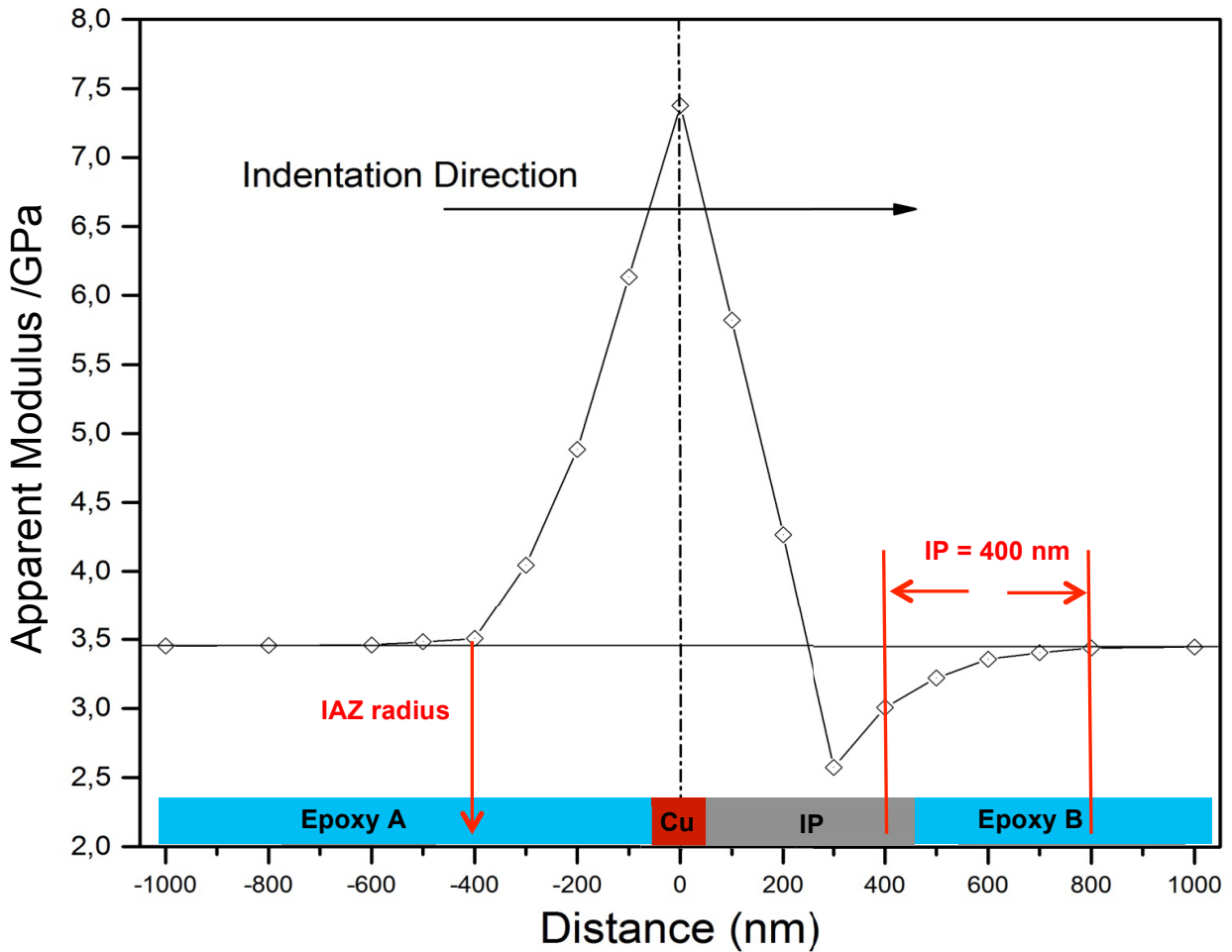


Figure 3.15: Variation of the elastic modulus values with the distance from copper in an epoxy/Cu/epoxy system with an interphase on only one side of the copper, using 60 nm deep indents. The diagrams below show IAZ at the points when it (a) starts touching Cu, (b) stops touching copper and starts touching the IP only, and (c) stops touching the IP.

In Figure 3.15, and similar to the plot in Figure 3.12 resulting from 150 nm deep indentations, the thickness of the interphase can be measured by determining the IAZ radius from the side of epoxy A, and accounting for it on the side of epoxy B. At a distance of 400 nm to the left of the copper (Epoxy A region), the value of the apparent elastic modulus starts increasing from the bulk epoxy value, which means that the copper starts to restrict the formation of a stress zone around the indenter. This can be used to determine an IAZ with a radius of 400 nm as represented in Figure 3.15a. Using this information, both points on the side of epoxy B at which the IAZ stops interacting with the copper (Figure 3.15b) and the interphase (Figure 3.15c) can be determined. Accordingly, an interphase thickness of 400 nm can be measured, which is the correct thickness that was provided initially in the model.

The size of the stress zone associated with a certain indent was reported by Hodzic et al.¹⁵ to be double the indentation width, which is directly related to the indentation depth. The results shown above for the 60 nm indentations combined with the results shown earlier for the 150 nm indentations confirm the validity of the proposed model regardless of the indentation depth being used. Although the 150 nm indentations are relatively large, it was possible to use them successfully to obtain the same results as the 60 nm indentations regarding the interphase thickness. This is because the IAZ size is different in both cases, but the influence of its interaction with only the interphase is the same.

In order to demonstrate this idea, the 2 plots from the two indentation series are combined in Figure 3.16, and the curve of the 150 nm indentations was slightly shifted upwards so that the curves coincide at the bulk region. The IAZ associated with a larger indent on one side of the copper will start getting constrained by the copper at a larger distance. Similarly, the constriction will also end on the other side at a later point compared to a smaller indent. The point at which this constriction ends, no matter where it is, will be also the point where the interphase starts contributing solely to the mechanical property variation from the bulk. The extent of this contribution is the same regardless of the indentation depth and can be used to determine the interphase thickness. The only difference is that it will be shifted to different distances from the copper. For example, in the case of 60 nm indents, the interphase was identified on the plot between 400 and 800 nm from the copper, while in the case of 150 nm indents it was identified between 800 and 1200 nm.

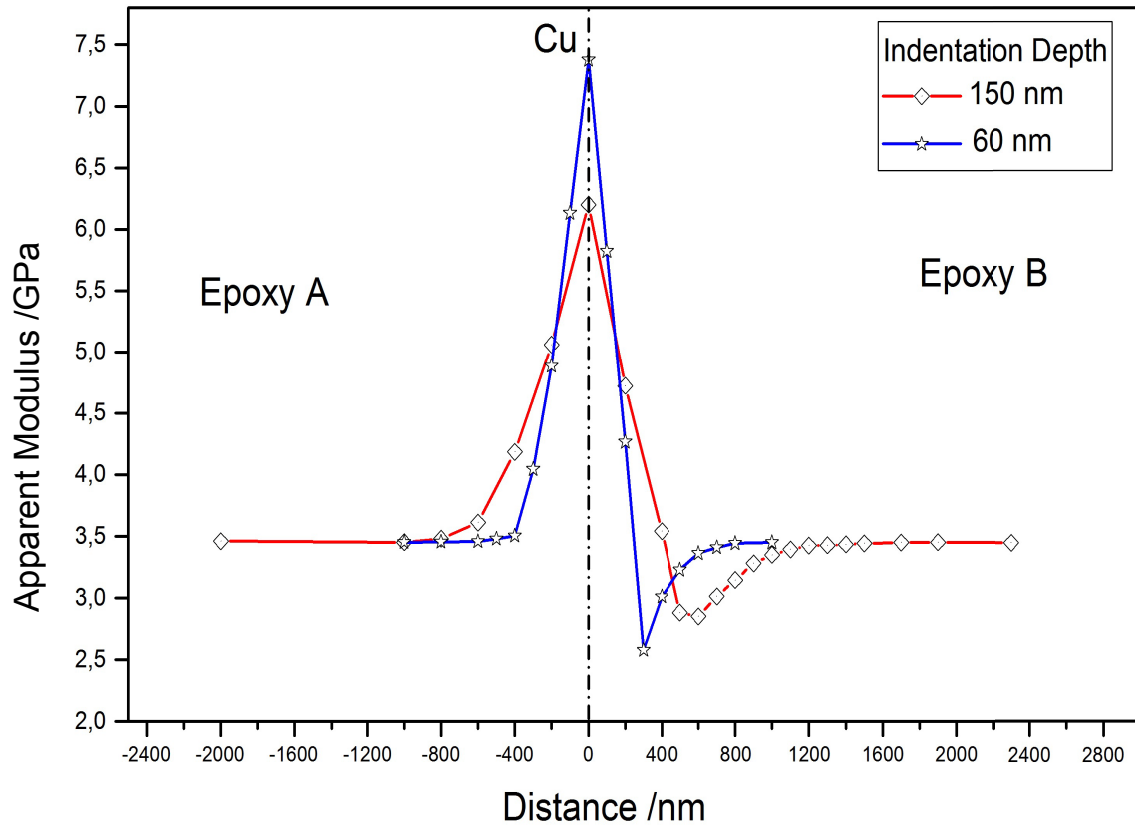


Figure 3.16: Comparing the mechanical property variation in the proposed model when the indentation depth applied is 60 or 150 nm.

The second important thing to notice about the plots above is the obvious relation between the intensity of the different peaks and the indentation depth; a smaller indentation depth results in higher peak intensity. This means that the contribution of a certain phase in the system (e.g. copper or interphase) becomes more pronounced when a smaller indentation depth is applied. This can be useful in real experiments for easier identification of the interphase, since any change in the mechanical properties from the bulk will be more obvious. Moreover, applying smaller indentation depths would provide more information about the extent of mechanical property change within the interphase compared to the bulk. This agrees with several studies that highlighted the necessity of reducing the indentation depth as much as possible.^{12–14}

3.4 Conclusion

One of the main problems associated with applying nanoindentation in interphases is that the indenter and stress zone formed around it get constrained by the stiff reinforcement in the composite. An epoxy/Cu/epoxy model was proposed, where the copper layer is very thin and the interphase is located at only one epoxy side. There were two hypotheses behind this model: First, when the thickness of the copper layer is very thin (100 nm), it should not be stiff enough to restrict the indenter. Second, even if the copper exhibits such constriction, the presence of the interphase at only one of its sides will allow using the other side as a reference for detecting the radius of the IAZ. This way, it would be possible to account solely for the mechanical property variations caused by the interphase on the other side. The finite element method was used to verify the validity of those assumptions. The results showed that a copper layer with a thickness of only 100 nm is still stiff enough to restrict the formation of a stress zone in its vicinity. Despite this effect, it was possible to successfully determine the extent of the IAZ, which further allowed identifying the thickness and variation of mechanical properties within the interphase.

The FEM calculations also showed that this method can be used to determine the interphase size and relative properties regardless of the indentation depth. Because of the relatively large size of the indenter compared to the interphase thickness, it is difficult to determine the absolute mechanical properties in the interphase region, since the measured property values will always be influenced by the other phases in the system as well. However, it was shown that by decreasing the indentation depth, the contribution of the interphase to the measured values will increase and the variation of the interphase mechanical properties from the bulk properties becomes more pronounced.

4

Characterization of the Interphase in an Amine-cured Epoxy/Copper System

4.1 Introduction

In the previous chapter, a system was presented that allows distinguishing the variations of the mechanical properties around an interface caused by the stiffness of the reinforcement, from those caused by the presence of an interphase when nanoindentation is used. The system was verified using an FEM model, where the system was assumed to be purely elastic. However, experimentally, it is difficult to apply several adjacent indentations within the interphase zone due to plastic deformation. For example, in their attempt to investigate the interphase mechanical properties in a polypropylene/cellulose fiber system, Lee et al.¹³ performed adjacent indents in the interphase region with an indentation depth of 50 nm using a Berkovich indenter. According to equation (3.1), this indentation depth would result in an indentation width of ~ 376 nm. In order to avoid the overlap between two adjacent indents, a space equivalent to at least twice this indentation width should be left between the indents. When they applied indentations with 800 nm spaces in between, only one indent was found to be in the interphase region (Figure 4.1a). Therefore, they had to decrease the spaces between the indents to 400 nm, which is not big enough to avoid the overlap, but small enough to locate 2-3 indents in the interphase region (Figure 4.1b).

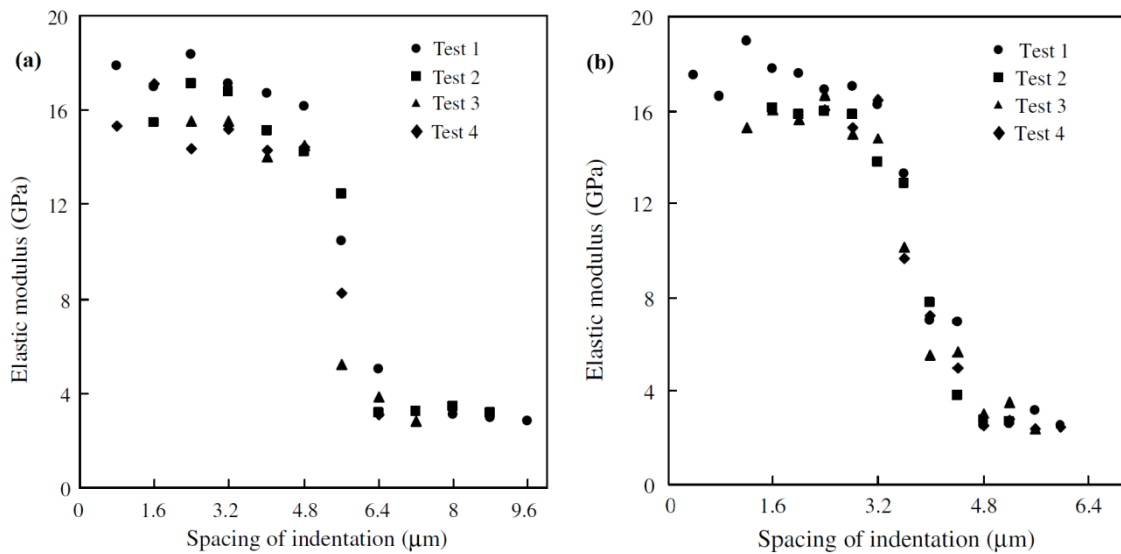


Figure 4.1: Variation of elastic modulus across the interphase region between the fiber and matrix obtained by 50 nm depth indentations, and spacing of: (a) 800 nm and (b) 400 nm.¹³

Similarly, Chung¹²⁰ attempted to measure the mechanical properties of the interphase between epoxy and copper using nanoindentation. He reported that the thickness of the applied indentations was around 6 μm, which is too big in comparison with the interphase thickness.

He concluded that nanoindentation technique is not sensitive enough to investigate the interphasial properties.

The common challenges that hinder using nanoindentation successfully for investigating interphases are usually less pronounced when AFM is used. Because of its very high lateral and vertical resolution, AFM in its different operating modes has proven useful in characterizing the mechanical properties of the interphase. Vanlandingham et al.¹⁰⁹ developed a technique that utilizes AFM as a nanoindentation device in order to investigate the interphases in three different systems: polysulfone/epoxy adhesive system, graphite fiber/polyimide and carbon fiber/epoxy. In the polysulfone/epoxy system, they found a different response at the interphase from that of the bulk epoxy or the bulk polysulfone, which was used to estimate an interphase of ~ 3 μm width. However, the finite element based calculations showed that the different indentation responses near the fibers in the other composites were a result of the mechanical constraint of the fiber on the local plastic deformation. Bogetti et al.¹¹⁰ reported that the interphase thickness in an unsized carbon fiber/epoxy system is as small as 3 nm based on finite element analysis and AFM nanoindentation. However, the sized fibers exhibited larger interphases of 50-200 nm, which were large enough to conduct useful AFM nanoindentation measurements.

Downing et al.¹¹⁸ used phase imaging AFM for probing the interphases in PMCs. They found a softer interphase than the bulk with a thickness of 2.4-2.9 μm . Gao and Mäder¹² also used phase imaging AFM to examine the mechanical properties of the interphase in glass fiber reinforced polypropylene and epoxy resin composites. Both harder and softer interphases were reported depending on the type of the fiber sizing. The interphase thicknesses varied between less than 100 nm and 300 nm depending on the type of the fiber sizing and the matrix material.

Mai et al.¹²¹ used AFM in force modulation mode (FMM) to examine the interphase between both sized and unsized glass fibers and an epoxy matrix. They were able to determine interphase thicknesses of 1 and 3 μm for sized and unsized fibers, respectively. Munz et al.¹²² also used AFM-FMM to investigate the interphase in a carbon fiber/epoxy system and reported an interphase thickness of 20-80 nm. Chung et al.⁵⁸ used AFM-FMM to investigate the stiffness variation in the interphase in amine-cured epoxy adjacent to copper microstructures. They found a high-stiffness region next to the interface with copper,

followed by a low-stiffness region compared to the bulk until a point of minimum stiffness, and then increasing again towards the bulk. The whole width of the stiffness variation was $\sim 1.9 \mu\text{m}$ with a local minimum point at $\sim 0.43 \mu\text{m}$ as shown in Figure 4.2.

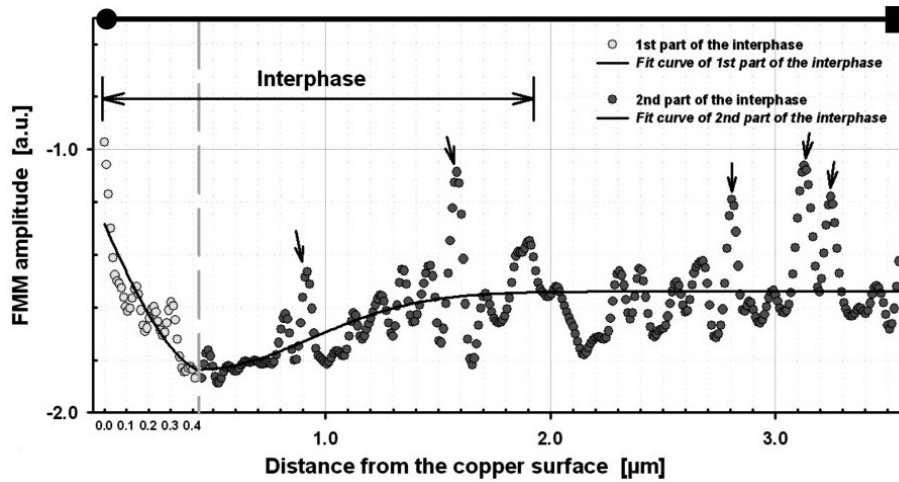


Figure 4.2: FMM amplitude profile of epoxy/copper interphase with Gaussian fit curves.⁵⁸

In this chapter, we verify the validity of the proposed system experimentally. A sample preparation method is utilized, which allows having a smooth continuous surface of an epoxy/Cu/epoxy system with an interphase at only one side of the copper. The experimental setup of nanoindentation is explained, as well as the procedure followed in order to minimize the common errors associated with a nanoindentation test. A method of applying nanoindentation near the interface is introduced, which would allow applying multiple indentations in the region in question without overlap. Moreover, some geometrical aspects regarding the Berkovich indenter and its application near interfaces are discussed. Finally, AFM measurements are carried out as a reference method, and the results are compared to those obtained from nanoindentation.

4.2 Experimental Work

Sample Preparation Principle

In order to produce epoxy/Cu/epoxy samples with an interphase on only one side of the copper, a concept for sample preparation was developed as illustrated in Figure 4.3.

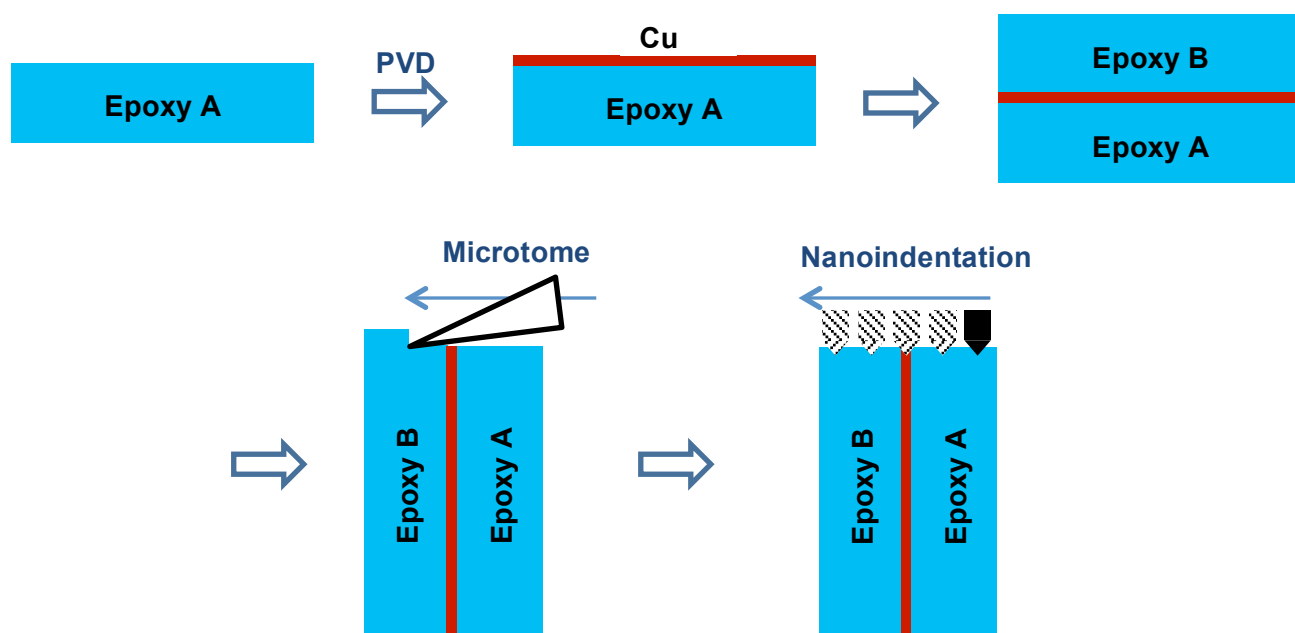


Figure 4.3: Illustration of the sample preparation concept.

The method involves preparing one epoxy block (epoxy A) with a smooth surface. Afterwards, the surface of the already cured epoxy A is coated with a very thin copper layer of 100 nm thickness or less. Because the copper layer is bonded to epoxy A physically, it is supposed that there will be no interphase in between. Another epoxy layer (epoxy B) is then cast on top of the copper layer, so that it cures while in contact with copper. This allows a chemical interaction to happen between epoxy B and the copper, providing a chance for an interphase to form. Finally, the surface of the epoxy/Cu/epoxy sample is cut using microtome in order to obtain a smooth continuous surface, on which nanoindentation or AFM measurements can be performed across the copper layer.

Materials

The epoxy system used in this study is an amine-cured epoxy that is prepared from the commercial products: EPIKOTE™ Resin MGS® RIM 135 and EPIKOTE™ Curing Agent MGS® RIM H 137, which are provided by Momentive Inc. The epoxy system is described by the supplier as a low viscosity system with a pot life of approximately 0.5 - 4 hours, which can be processed and cured at relatively low temperatures (10-50 °C).¹²³ Both the resin and the hardener have a very low vapor pressure, which allows them to be processed under vacuum even at high temperatures. Some specifications of the system components are presented in Table 4.1.

Table 4.1: Specifications of the used epoxy resin and amine-based hardener.¹²³

	Resin: RIM 135	Hardener: RIMH 137
Density [g/cm ³]	1.13 – 1.17	0.93 – 0.98
Viscosity [mPas]	700 - 1.100	10 - 50
Epoxy value [equivalent/100g]	0.54 – 0.60	-
Amine value [mg KOH/g]	-	400 - 600
Refractory index	1.548-1.552	1.460 – 1.463

The RIM 135 epoxy resin is a combination of bisphenol A diglycidyl ether (DGEBA) and 1,6-hexanediol diglycidyl ether, while the RIMH 137 hardener is mainly composed of alkyl ether amine and isophorone diamine.¹²⁴

Sample Preparation

The first step is to prepare the first epoxy part (epoxy A), which will act as a substrate for the copper layer. Before mixing the resin and the hardener, if the resin shows signs of crystallization (cloudiness), it should be preheated at 50 °C for two hours while stirring. This would allow decrystallization of the resin without influencing its quality.¹²³ The resin and the hardener were then added into a beaker with a ratio of 100:30 as recommended by the supplier. The mixture was homogenized by stirring vigorously for 10 min. Because stirring results in incorporation of bubbles, the mixture was then placed in a vacuum chamber for 25 min, after which no bubbles were visible anymore.

For casting the samples, a Teflon[®] mold was used to facilitate detaching the samples after curing (Figure 4.4). The mold consists of a feeding channel (gate) through which the mixture is cast, parallel vertical mold cavities where epoxy bars will be formed with 1 cm width and 4 mm thickness, and a sealing channel where a rubber cord is inserted. Finally, a PMMA cover was clamped into the mold using four metal clamps. The epoxy/PMMA cover contact while curing helps obtain samples with smooth surfaces.

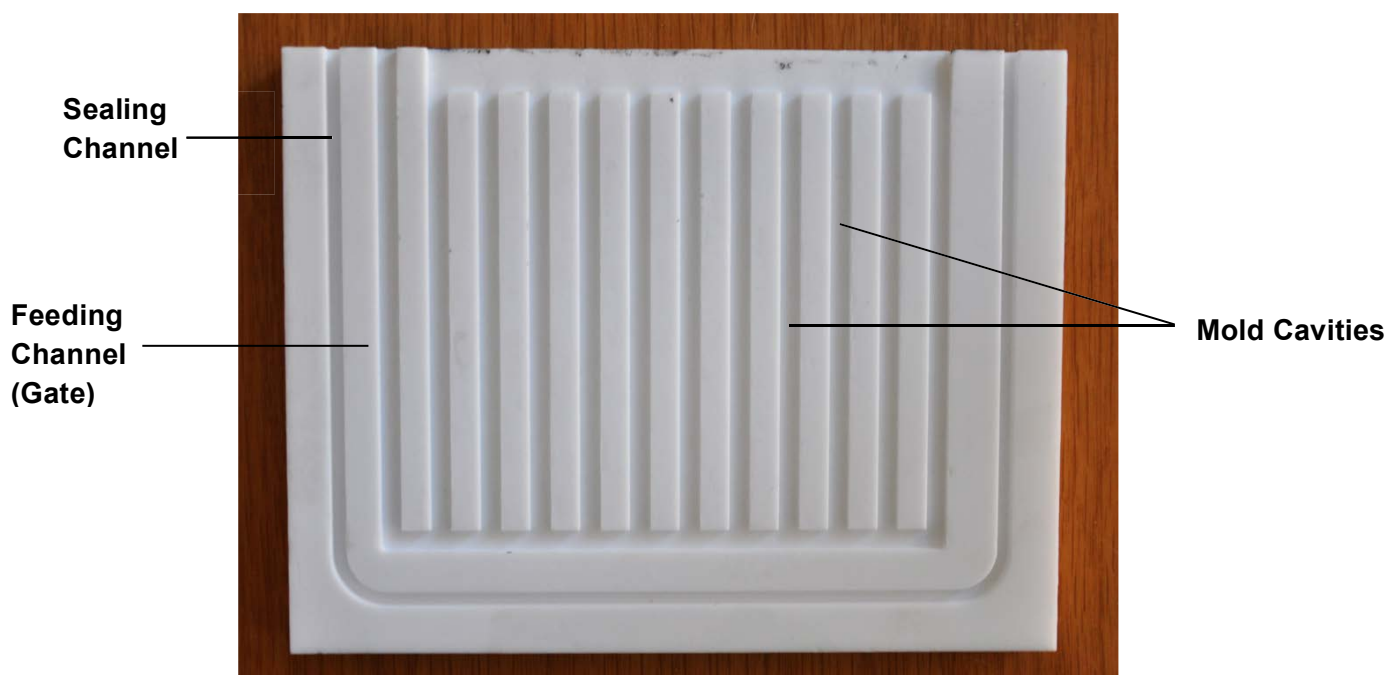


Figure 4.4: The Teflon[®] mold used for casting the samples.

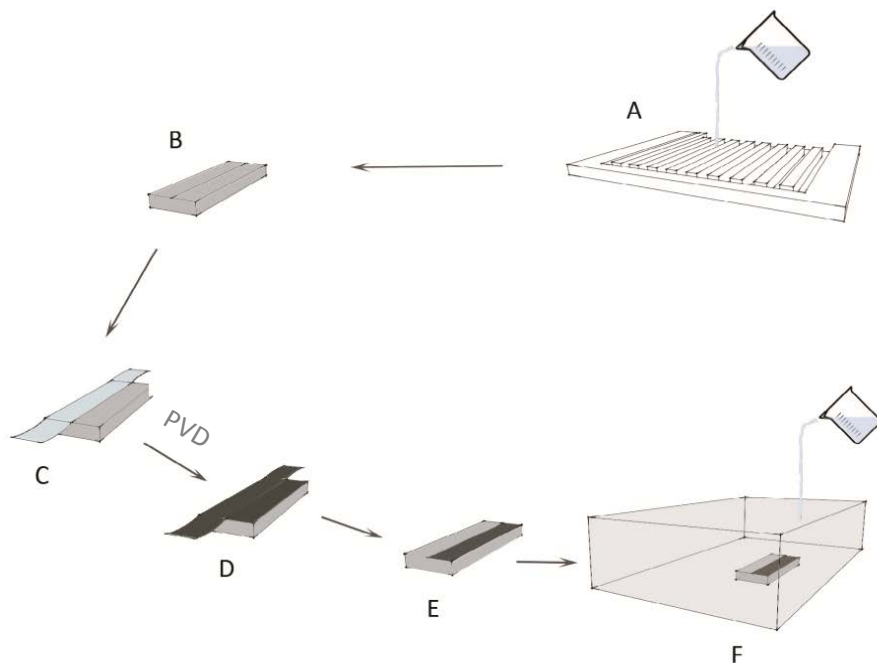
Curing took place at room temperature over 48 hours. Afterwards, the samples were detached from the mold and post-cured by placing them in the oven for 15 hours at 80 °C. Finally the cured epoxy bars were cut into smaller samples of equal length of 4 cm.

The second step is to deposit copper layers of different thicknesses on the surfaces of the prepared epoxy blocks. The copper layers were deposited using physical vapor deposition (PVD). For this aim the coating module (Roth & Rau), part of a CS 730 ECS cluster coating system (VON ARDENNE) was used. The sputtering gas used was Argon 5.0 under a pressure of 10^{-3} mbar. By altering the operating power and the sputtering time, it was possible to deposit copper layers of different thicknesses. Silicon wafers were sputtered simultaneously, and the thickness of the deposited layers was then measured using an Ambios XP2 profilometer. The sputtering parameters used to achieve the different desired thicknesses as well as the corresponding measured thicknesses are represented in Table 4.2. In this study, the desired thicknesses will be used to refer to the different samples.

Table 4.2: The PVD parameters used to deposit copper layers of different thicknesses.

Desired Thickness (nm)	Operating Power (W)	Sputtering Time (s)	Measured Thickness (nm)
100	1000	14	102
75	1000	10	78
40	1000	4	38
20	300	5	17
10	200	1	10

The copper-coated samples were then placed in bigger PMMA molds. The second epoxy layer (epoxy B) was prepared in the same way described earlier, cast on the coated samples, and was cured under the same conditions forming epoxy/Cu/epoxy sandwich samples. It is worth mentioning that the two epoxy parts tended to separate from each other at the copper interface. To avoid this problem, half of the surface of epoxy A was covered using cellophane tape during sputtering, so that only half of the surface gets coated. This allows having a strong bonding between the two bare epoxy surfaces and provides the necessary integrity for the whole structure. The whole sample preparation process is illustrated schematically in Figure 4.5.


Figure 4.5: The procedure followed to prepare epoxy/Cu/epoxy samples.

In order to prepare a smooth continuous flat surface for nanoindentation, the samples were cut using ultramicrotome. The sandwich samples were first cut into smaller cubes of suitable sizes and glued onto a metal sample holder. The specimen trimmer Leica EM Trim was then used to mill two sides of the cube at an angle of 45° , forming a pyramid with a sharp edge (Figure 4.6a). Trimming was adjusted so that the copper layer passes at that sharp edge.

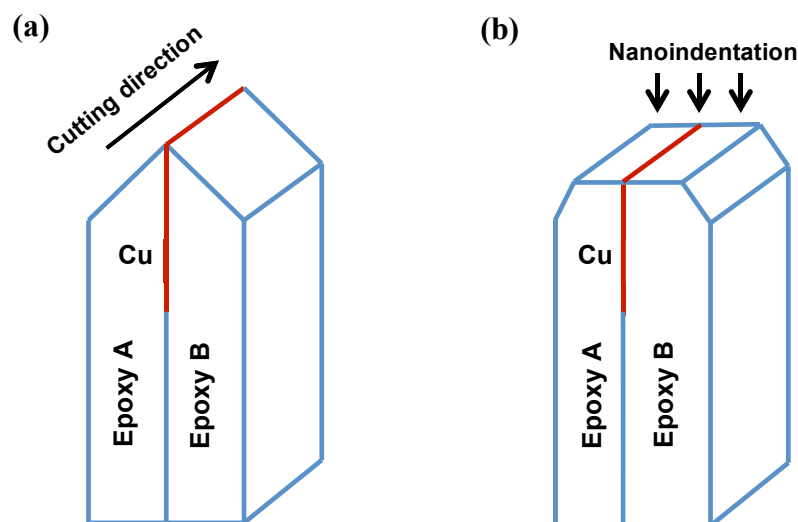


Figure 4.6: The sandwich sample shape (a) after trimming and (b) after cutting with the microtome.

After trimming, the sample is ready to be cut using the microtome. The microtome used in this work is the ultramicrotome Leica Ultracut UCT, equipped with an ultra DiATOME diamond knife with an included angle of 45° . The final shape of the samples after cutting with the microtome is shown in Figure 4.6a. The upper epoxy/Cu/epoxy horizontal surface is used for nanoindentation, while the epoxy-epoxy interface at the lower part of the sample provides the sample with the needed structural integrity due to its strong bonding.

The microtome cutting parameters are crucial and need to be considered carefully. These include mainly the section thickness, the cutting speed and the clearance angle (Figure 4.7). For example, cutting sections of bigger thicknesses was found to improve the surface roughness of the samples. However, it resulted often in the separation of the two epoxy parts at the copper interface. Moreover, due to the higher forces involved, cutting thicker sections would also shorten the life of the diamond knife.¹²⁵ A section thickness of 200 nm was found to be optimal and was used for cutting all samples. On the other hand, cutting at high speeds can cause artifacts such as undulations. Therefore, the cutting speed was fixed at 1 mm/s as recommended by the manufacturer.¹²⁶

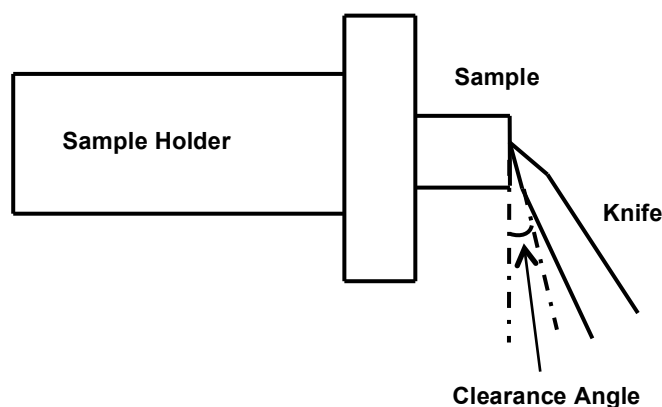


Figure 4.7: Illustration of the microtome setup and the involved clearance angle.

The clearance angle is also an important factor in microtomy. If the clearance angle is too wide, the knife will scrape the sample causing chatter and wrinkled surfaces will be obtained. On the other hand, a narrow clearance angle can cause the sections to be dragged over the knife edge, which influences the quality of the surface as cutting goes on.¹²⁵ An optimized clearance angle was found to be 6° and was used for preparing all the samples.

Nanoindentation Instrumentation

In this study, a Hysitron TriboScope® (Hysitron, Minneapolis, MN) was used for performing the nanoindentation experiments. The Hysitron TriboScope is an add-on nanoindentation system to a commercial scanning probe microscope (SPM). This provides the system with the capability of performing in-situ SPM imaging, which allows accurate positioning of the indenter relative to certain features or phases in the material. Moreover, an image of the indentation imprints can be immediately obtained by using the same indenter tip to scan the surface without the need to reposition an imaging instrument again over the tested region. The instrumentation is illustrated schematically in Figure 4.8. The main part of the Hysitron TriboScope is a head to which a diamond Berkovich indenter is attached. This head can be replaced easily by an optical microscope to determine the initial region of the sample to be tested. Inside this head, there is an electrostatic transducer based on a three-plate electrical capacitor (Figure 4.8).¹²⁷ The indenter is mounted to the middle plate, which is suspended by flexible springs, while the other two plates are fixed.

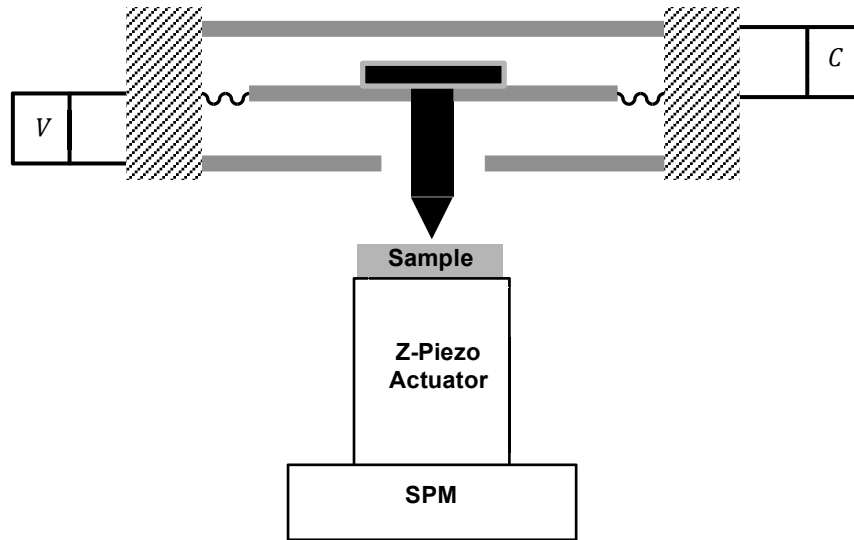


Figure 4.8: Schematic illustration of the TriboScope in use with a scanning probe microscope (SPM).

The typical way this three-plate system works, is that a voltage (V) is applied between the lower and the middle plate, creating an electrostatic attraction force which causes the middle plate (and the indenter) to move down. The value of the electrostatic force (F_{el}) is proportional to the square of the applied voltage as follows:¹²⁸

$$F_{el} = k_e \cdot V^2 \quad (4.1)$$

where k_e is the electrostatic force constant and it is determined and supplied by the manufacturer. It depends on the plate area and the distance between the middle and the lower plates. Simultaneously, the control system measures the capacitance (C) between the middle and the upper plates, which is inversely proportional to the distance between them. This way, the indentation force can be controlled and the corresponding indentation depth can be measured.

In the principle explained above, the indentation force is the resultant of both, the electrostatic force and the force of the springs holding the middle plate. The spring force should be subtracted in order to obtain the actual force applied on the sample as follows:

$$F_{ind} = F_{el} - F_{spring} \quad (4.2)$$

and according to Hooke's law, the spring force is a function of the vertical displacement:

$$F_{spring} = k_s \cdot d \quad (4.3)$$

where d is the displacement and k_s is the spring constant.

The spring constant, however, can be a likely source of error. This error can even be nonlinear due to the system configuration and continuous changes over in-service time can result in considerable measurement errors. It is recommended by the manufacturer that calibration should be done prior to every single measurement.¹²⁹ In order to avoid such an error, a modification to how the transducer operates was introduced. This modification encompasses holding the middle plate fixed at zero-position. The middle plate (and the mounted indenter) does not approach the sample. Instead, the sample approaches the fixed middle plate using the piezo actuator in the z-axis. Once the sample and the indenter are brought into contact, and as the sample keeps moving up, a voltage is applied between the lower two plates in order to create an electrostatic force that opposes this movement and keeps the middle plate fixed. From the point of contact, any further movement of the z-axis piezo actuator would translate into indentation depth inside the sample. Similarly, the created electrostatic force corresponds to the indentation force. By introducing this modification, the springs holding the middle plate are not involved in the measurements anymore, and the associated errors can be avoided.

Scanning the Surface Topography

The SPM feature can be used to scan the surface topography. The sample is brought into contact with the indenter and the distance in the z-direction is held constant, while the piezo actuators move the sample in the x- and y-directions. Because the displacement in the z-direction is held constant, any changes in the surface topography would result in changes in the measured electrostatic force. These changes can be used to produce a force map that provides useful information about the sample topography and indicate the exact regions to be investigated. A full-size scan would result in images with a size of 200 μm x 200 μm . The image resolution is determined by the scanning velocity as well as the number of points per scanning line.

Temperature Regulation

In order to minimize thermal drift errors, the whole indentation setup explained above is placed inside a temperature regulation chamber. The chamber is built from Styrofoam walls with a thickness of 10 cm. The temperature inside the chamber is set to a specific value which is 3-5° above room temperature, as it is easier to regulate the temperature through heating up rather than cooling down. Inside the chamber, a fan forces air to circulate through an aluminum tube, through which it cools down. The lost temperature during circulation is compensated by three sources of heat: the heat produced by the fan itself, the heat produced by the indentation instrument and a heating coil. The heating coil provides the necessary heat so that the temperature measured at the sensor located next to the indentation device is always kept constant and equal to the set temperature through closed loop control. A schematic illustration for the regulation cycle is provided in Figure 4.9.

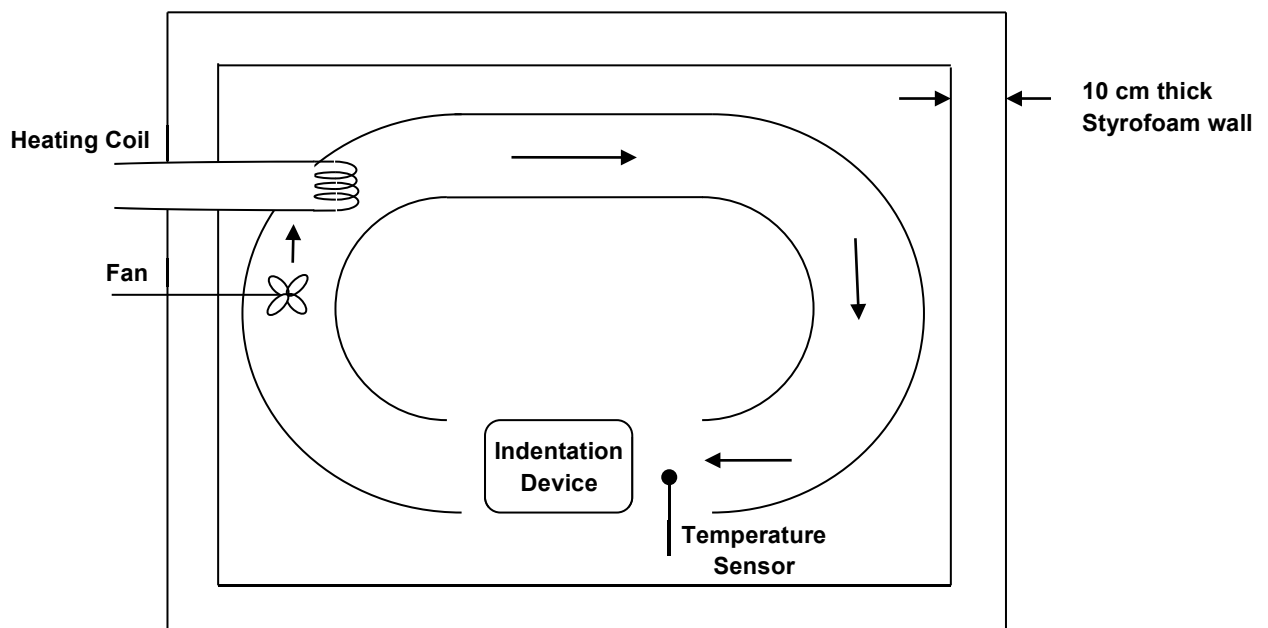


Figure 4.9: Schematic illustration for the temperature regulation cycle.

The temperature system has proved to be very efficient, as it provides constant temperatures over long periods of time with deviations of less than ± 0.02 °C as shown in Figure 4.10.

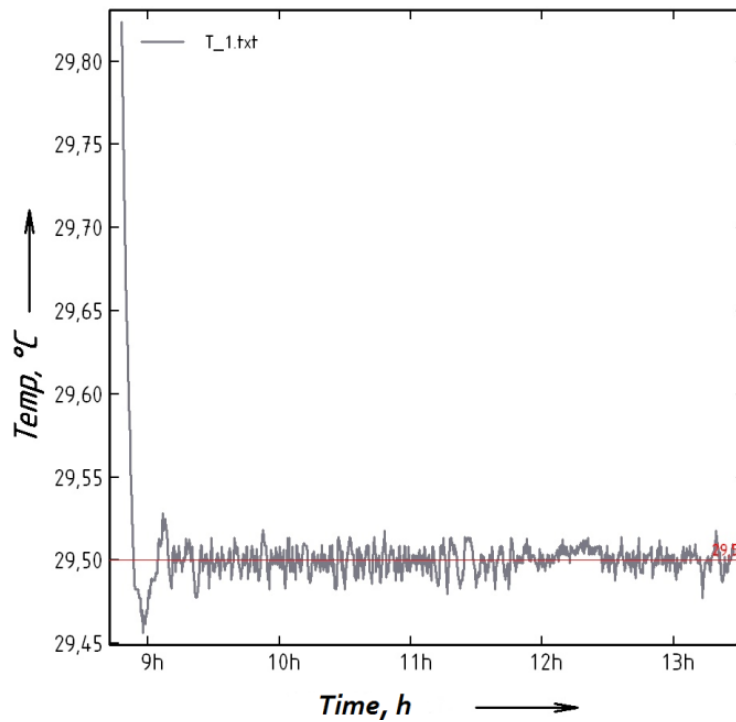


Figure 4.10: Temperature profile inside the chamber over a period of 4 hours.

Area Function Calibration

In order to calibrate the area function of the indenter, and to account for the errors induced from pile-up/sink-in effects or machine compliance, the epoxy itself was used as a reference material. The mechanical properties of the used epoxy were measured by performing a tensile test according to ISO 527-1. The elastic modulus and Poisson's ratio were found to be 3.365 GPa and 0.39, respectively. Pure epoxy samples were then prepared using the microtome in the same way explained earlier, and multiple series of indentations were applied at a range of different indentation forces similar to those used later for the measurements. The area function was then plotted versus the resulting indentation depth and fitted according to the presumed elastic modulus values. The area function was saved and used for evaluating further measurements.

Investigating the Influence of Surface Roughness

In order to investigate the influence of surface roughness on the measurements, pure epoxy samples were prepared using the microtome, and multiple series of 25 indentations were applied using different indentation forces ranging from 20 μN to 2 mN. The scattering of the

results versus indentation force was monitored in order to determine the smallest force/depth, before which the results are unreliable.

Nanoindentation across Copper

In order to investigate the different prepared samples using nanoindentation, the samples are first placed on the sample holder of the instrument, and an optical microscope is used to locate the primary region to be tested. The optical microscope is then replaced by the Hysitron TriboScope head and a full-size scan using SPM is performed. Using the obtained image, the copper interface is identified and indentations are applied across the copper from epoxy A to epoxy B. Most of the nanoindentation tests applied were force-controlled; i.e. the maximum force is given and the indentation depth is monitored. Some experiments required displacement-controlled indentations and will be mentioned in the results section.

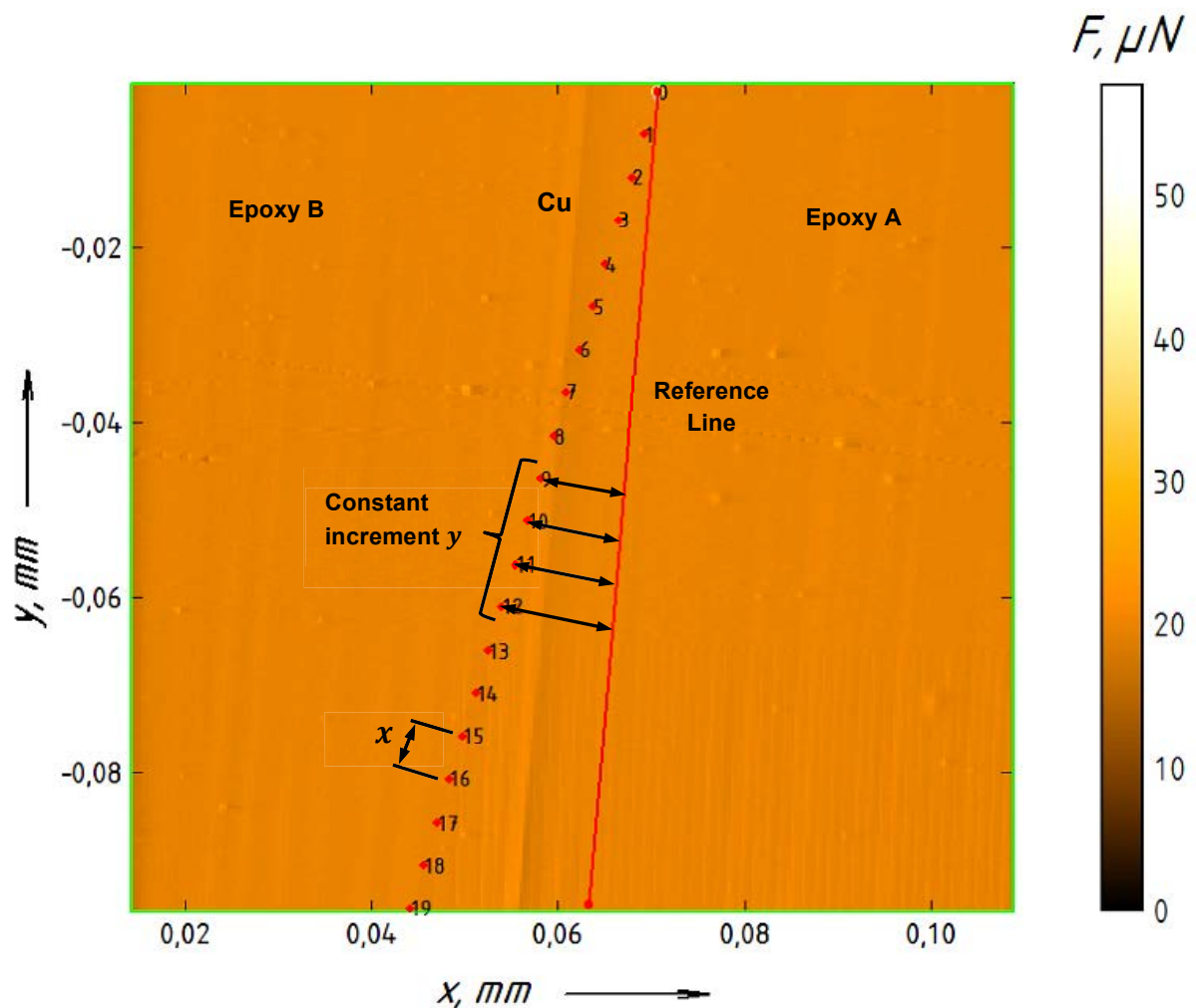


Figure 4.11: Illustration of the method used to apply indentations across the copper.

In order to apply as many indentations as possible in the region of interest while avoiding overlap between them, the way of applying the indentations across copper was modified. The indentations were applied with respect to a reference line as shown in Figure 4.1. This allows adjusting the distance x between two adjacent indents, and the increments y with which the indents approach the reference line. This reference line was always positioned to be parallel to the copper interface on the side of epoxy A, so that the indentations would cross the copper from epoxy A to epoxy B. The distance x depends on the indentation depth and was decided according to equation (3.1). The increment y will determine the number of indentations in the region to be tested; a smaller value of y would result in more indentation. It is controlled by both the distance x and the size of the scan.

All indentations were applied using the same loading cycle: 2 seconds loading, 30 seconds of holding time at maximum load to minimize creep effects, and 2 seconds of unloading. The obtained force-displacement curves were processed using an evaluation software where the Oliver-Pharr method was applied. The upper 60 to 95 percent of the unloading curves were used for analysis. The top 5 percent were excluded to avoid scattering at maximum load.

AFM Measurements

In order to have a reference method, AFM measurements in force-distance mode were performed on the sample with 20 nm thick copper. The Asylum Research MFP-3DTM AFM was used in this study. The tip used was a PointProbe[®] Plus SPM probe made from n-type silicon with a radius of 13 nm, attached to a cantilever with a spring constant of 38.57 nN/nm. The test started by performing a topography scan, after which a trigger of 200 nm was used to perform measurements across the copper from epoxy A to epoxy B with spaces of 1 μm in between. By introducing a linear fit to each force-distance curve, a stiffness map was obtained where the stiffness variations around the copper can be monitored.

4.3 Results and Discussion

Influence of Surface Roughness

The Figure below shows mean and standard deviation values resulting from multiple series of 25 indentations applied with indentation forces ranging from 0.02 to 2 mN.

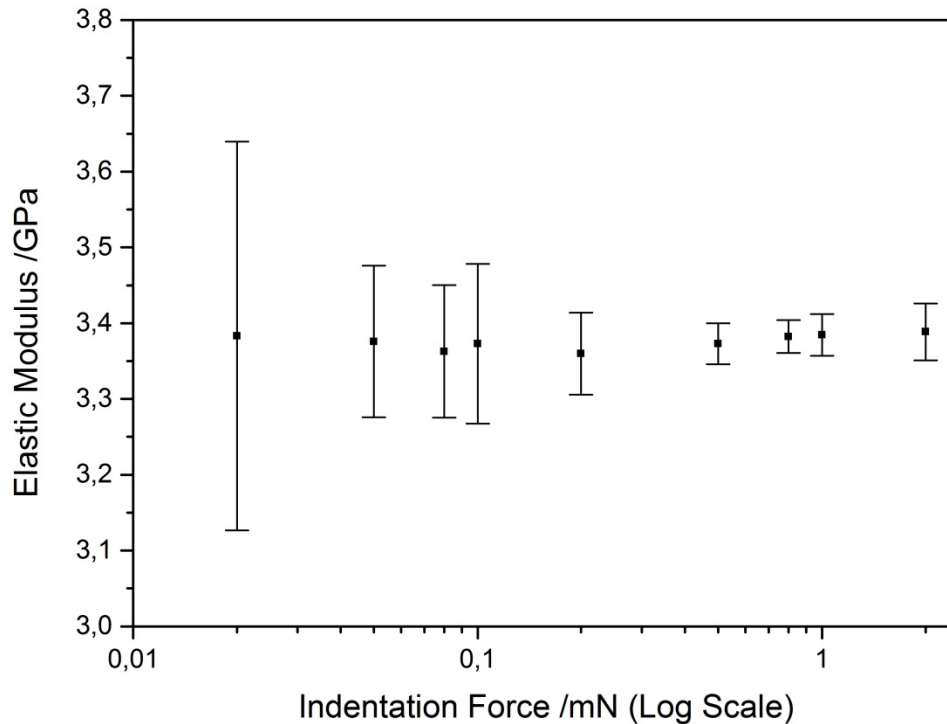


Figure 4.12: Mean and standard deviation of elastic modulus values resulting from different indentation forces.

The mean values of the elastic modulus resulting from the different indentation forces are all very close, which is a sign of good indenter area function calibration at different depths. However, there are significant differences in the results scattering represented by the standard deviation values. The smallest indentations performed using 0.02 mN resulted in indentations of ~35 nm depth and a large standard deviation of around 300 MPa. This large scattering implies that the indentation depth was in the same range of surface roughness. The indentations applied with forces ranging from 0.05 to 0.1 mN resulted in indentation depths of ~65 to 105 nm. The standard deviation of those indentations was considerably reduced to an approximate value of only 105 MPa. This value is small enough to perform reliable measurements across the copper and to recognize any changes in the elastic modulus values due to the presence of an interphase.

Doubling the indentation force to 0.2 mN resulted in indentation depths of ~ 160 nm, and further reduced the standard deviation. Accordingly, this indentation force was chosen accordingly to perform the initial measurements, and if needed, the indentation forces could be reduced down to a minimum of 50 μN , which is considered the limit for performing reliable measurements. Although higher indentation forces result in even less scattering, they would also result in indentations that are too big for the required measurements.

Preliminary Results and Indenter Geometry Effects

The initial measurements were performed on the sample with 100 nm thick copper layer, using a force of 0.2 mN and resulting in a depth of ~ 160 nm. The indentations approached the copper with 200 nm increments, while a space of 4 μm was left between the adjacent indentations. According to equation (3.1), an indentation depth of 160 nm results in an indentation width of ~ 1.2 μm , and according to Hodzic et al.¹⁵ the space between two indentations should be at least twice the indentation width in order to avoid overlap of the accompanying stress zones. This means that the space between the indentations should be at least 2.4 μm . Therefore, the applied space of 4 μm is large enough to avoid overlap. This can be seen in the SPM image in Figure 4.13.

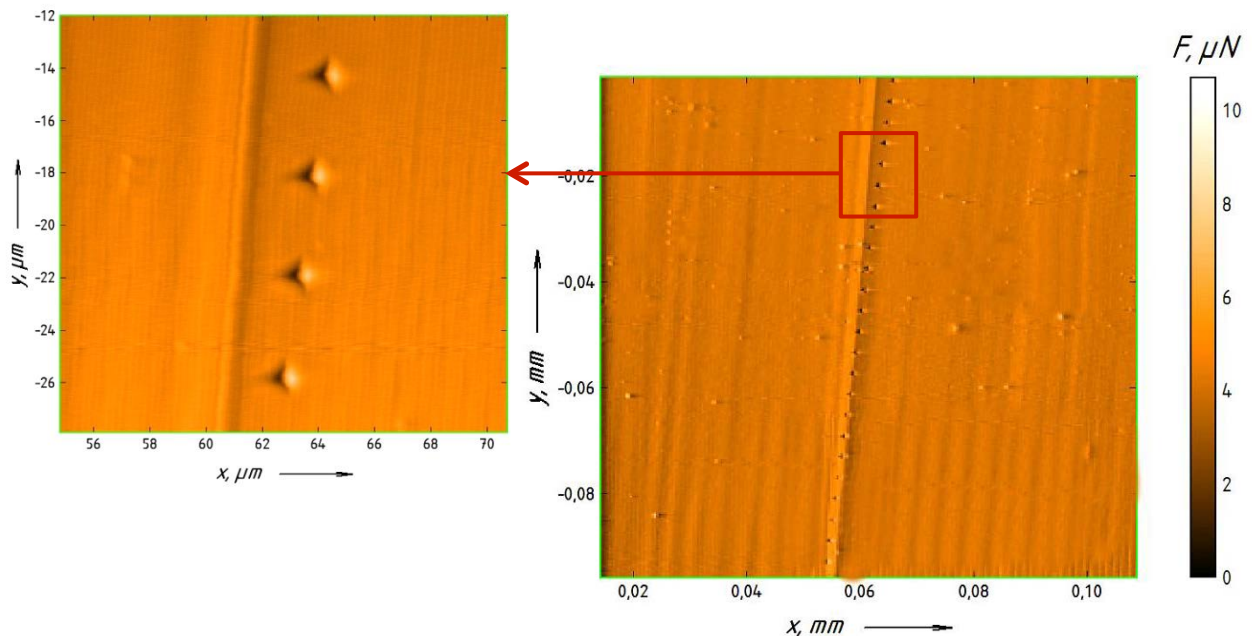


Figure 4.13: Indentations approaching copper with increments of 200 nm using a force of 0.2 mN without overlap.

Three series of indentations were applied on the same sample using the same conditions. The results are shown in Figure 4.14. All the curves were initially in the level of test 1 curve, but were shifted vertically to illustrate the variation in behavior.

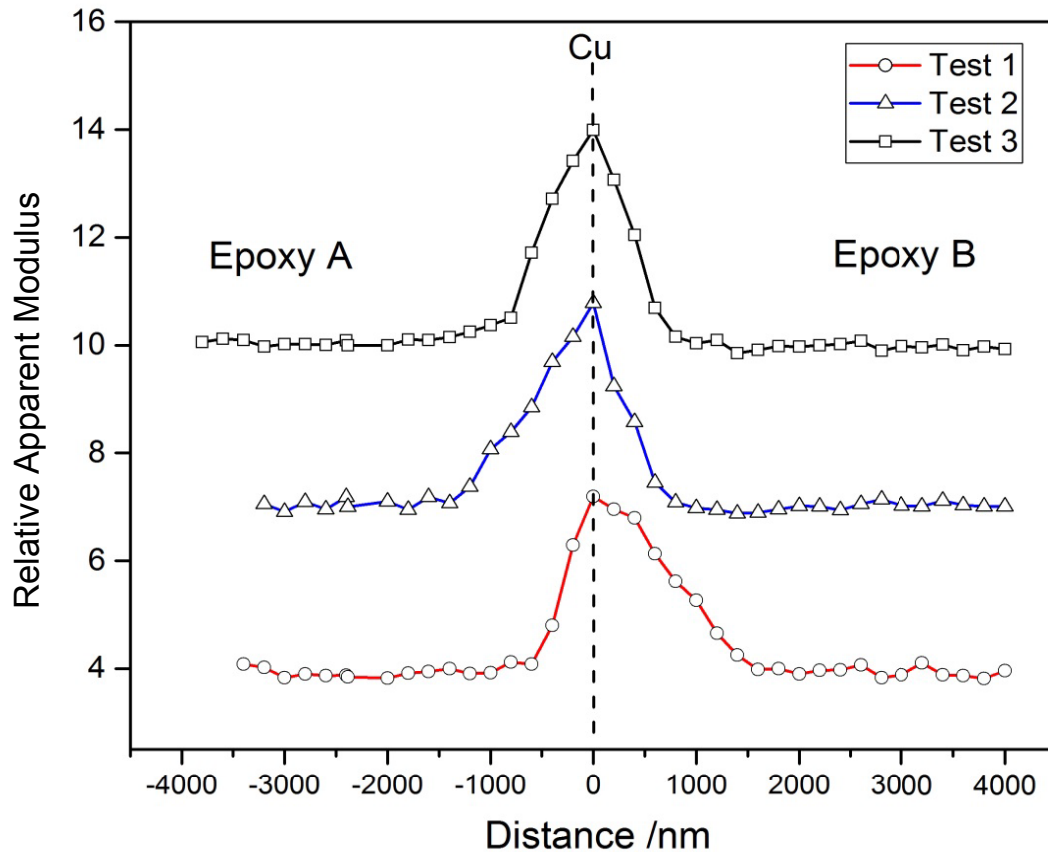


Figure 4.14: Variation of the apparent elastic modulus values with the distance from the 100 nm thick copper layer when 0.2 mN indentations are applied with a spacing of 200 nm.

The first thing that can be noticed from the plot above, is that in accordance with the results from the FEM, the copper with a thickness of 100 nm does have a mechanical influence on the indentations in its vicinity, which is represented by the peak around the copper. The second thing to be observed is the different slopes of the curve on both sides of the copper. This was first thought to be an influence of an interphase on the side of epoxy B. However, these slope variations did not have a fixed trend, as each of the three series resulted in a different behavior with the steeper slope being on either epoxy side.

Since this random behavior was unlikely to be caused by the material itself, it was thought that it might be caused by the indenter asymmetry around the copper. In order to check for this, a FEM model was run, where the indenter was oriented randomly so that it would have

an asymmetric geometry with respect to a perfect copper interface. Indentations with a depth of 150 nm were applied across the copper from epoxy A to epoxy B. The results are shown in Figure 4.15.

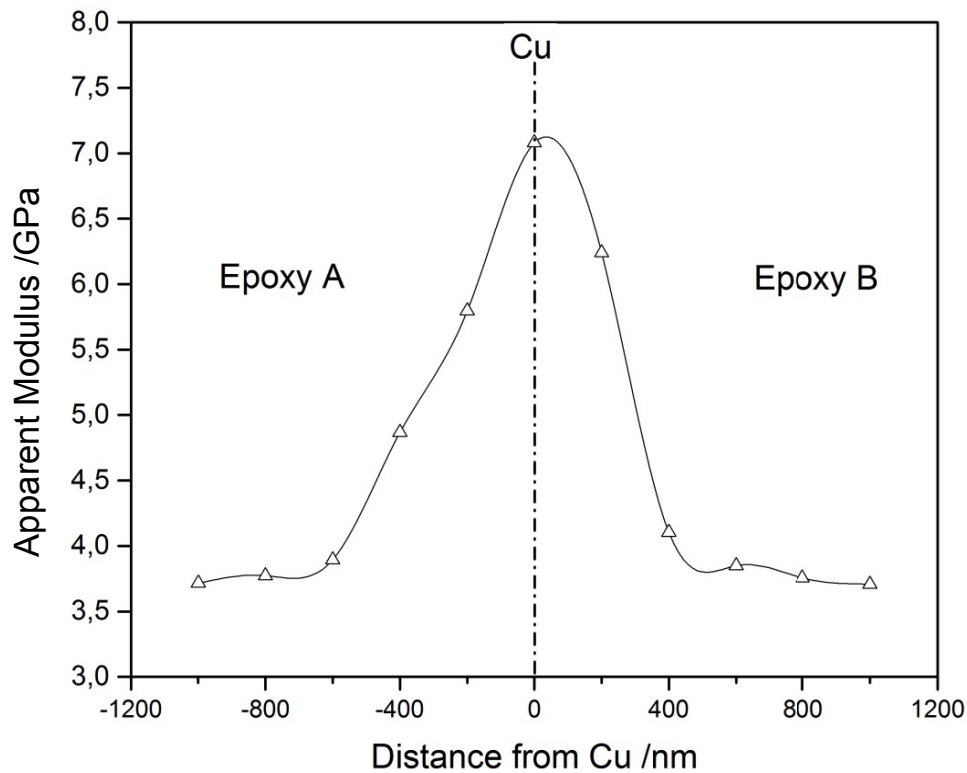


Figure 4.15: FEM calculations for 150 nm deep indentations applied across a perfect copper interface using randomly oriented Berkovich indenter

The FEM calculations show similar results to those obtained experimentally using nanoindentation. Even though there is no interphase in the FEM model, a different slope is noticed around the copper. The only difference between the curve above and the symmetrical curve showed in the previous chapter (Figure 3.9), is the indenter orientation. In Figure 3.9, the indenter geometry was symmetrical with respect to the copper line, while in Figure 4.15 it is asymmetrical. This influence is illustrated in Figure 4.16. In Figure 4.16a, the indenter is symmetrical around the copper. Therefore, when indentations are applied on both epoxy sides at the same distance d from the copper, the area of the indenter interacting with the copper in both cases will be the same and the calculated apparent elastic modulus values will be the same. In Figure 4.16b however, the indenter is asymmetric with respect to the copper layer. In this case, when an indentation is applied at the same distance d from the copper on both its sides, the area of the indenter interacting with the copper will be different in both cases. Hence, the calculated apparent elastic modulus values will be different as well.

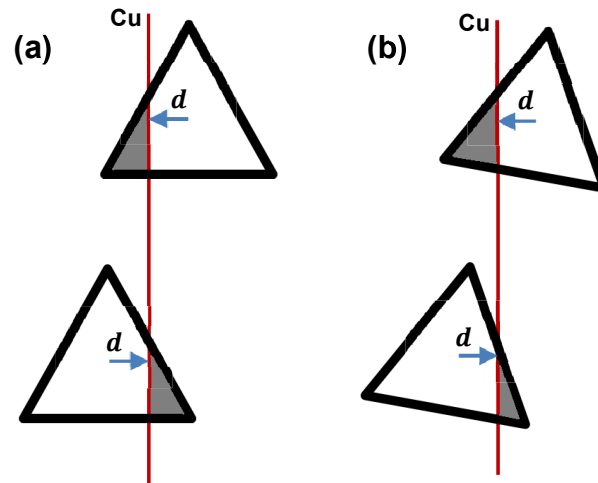


Figure 4.16: Schematic illustration of the projected areas of two indentations applied on both epoxy sides at the same distance d from the copper, when the Berkovich indenter is oriented (a) symmetrically and (b) asymmetrically with respect to the copper line.

The results above show that the asymmetrical geometry of the Berkovich indenter can be a major source of error when it comes to investigating the mechanical properties near the interface. However, such an error was barely reported in the literature and several interphase studies were performed using Berkovich indenter without discussing the influence of its asymmetric geometry on the obtained results.^{13,14,115,117} This error can be avoided by using a symmetrical indenter such as a conical indenter.¹¹⁹ In order to perform reliable investigations regarding the mechanical property variation in the interphase region using a Berkovich indenter, the asymmetry of the indenter geometry should be taken into account.

Accounting for the Indenter Asymmetry

Another series of indentations was applied on the same sample using the same parameters. This time, however, the sample was rotated so that the copper layer is aligned vertically, and the indenter orientation was adjusted to be symmetrical around the copper interface (as shown in Figure 4.16a). This setup was used for all the indentation tests performed from this point on. The resulting indentation imprints are shown in Figure 4.17.

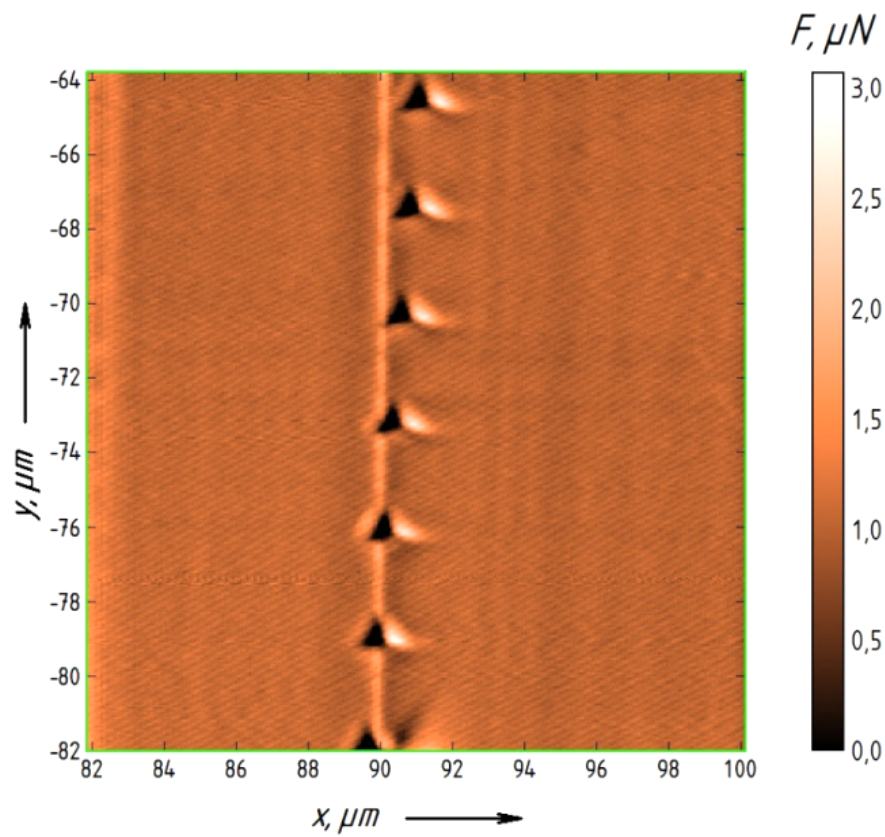


Figure 4.17: Imprints of 0.2 mN indentations that are aligned symmetrically with respect to the copper.

The apparent elastic modulus variation resulting from this indentation series is represented in Figure 4.18. From the plot, and in accordance with the plots in Figure 4.14 as well as the FEM results, the mechanical constriction of the copper on the indentations in its vicinity can be clearly seen, as there is an obvious increase in the modulus around the copper. The modulus starts increasing at a distance of ~ 1200 nm from the copper, which is equivalent to the radius of the IAZ.

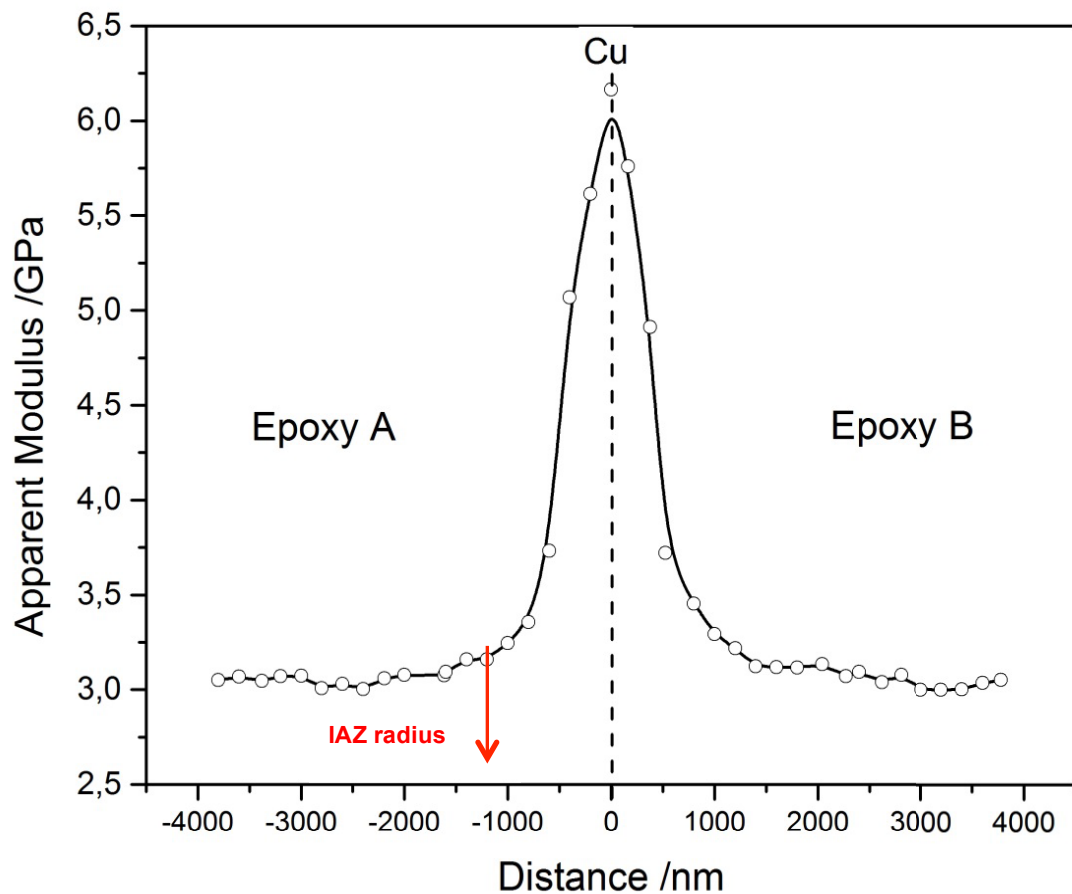


Figure 4.18: Apparent elastic modulus variation across the 100 nm thick copper, resulting from 0.2 mN indentations with 200 nm spacings.

In contrast with the plots in Figure 4.14, the variation in mechanical property is quite symmetrical around the copper. This is however surprising, because it does not show any signs of interphase existence. The results obtained from this experiment are similar to those obtained using FEM for a perfect interface (Figure 3.9). Further experiments were performed on other samples with different copper layer thicknesses using the same testing parameters. The results are shown in Figure 4.19. The curves show that the mechanical constriction of copper on the indentations decreases significantly with decreasing copper thickness. However, this cannot be totally avoided even with a thickness as small as 20 nm. Moreover, all the samples showed the same symmetrical behavior around the copper, which does not indicate the existence of an interphase of distinctive properties.

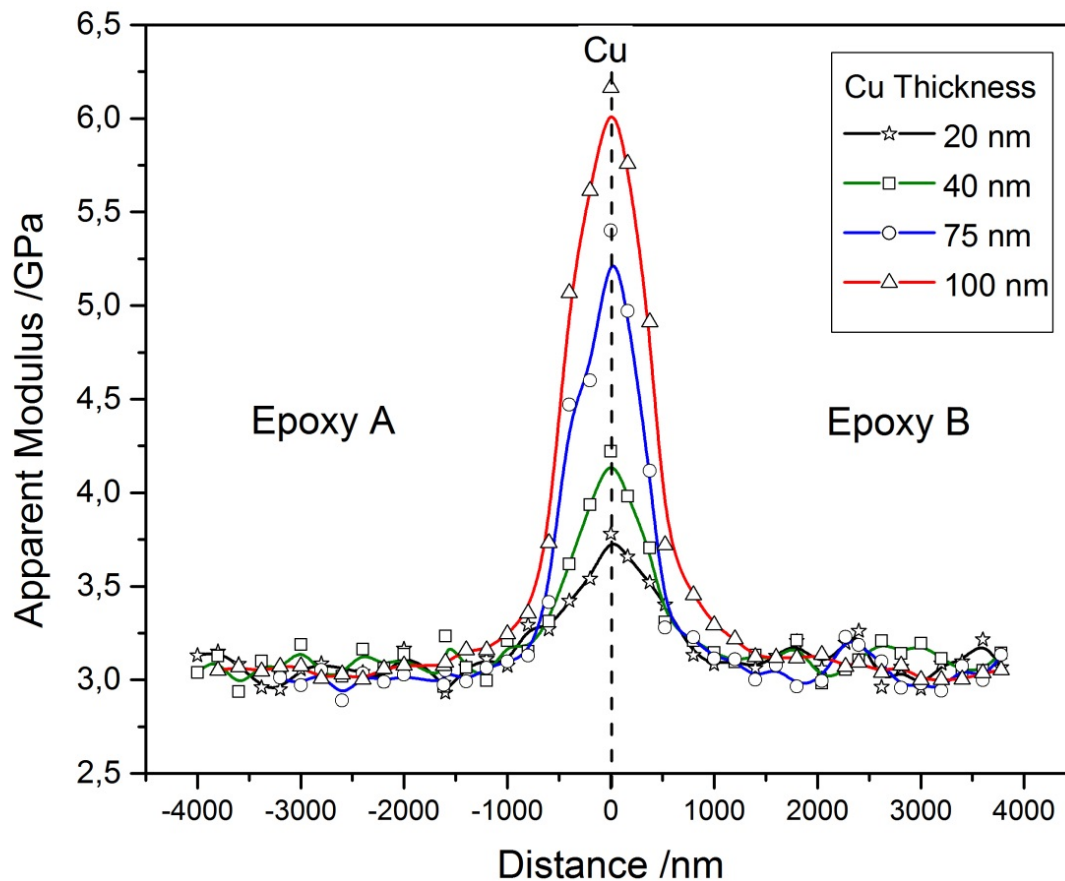


Figure 4.19: 0.2 mN indentations with a spacing of 200 nm performed across different copper thicknesses.

The first possible explanation for not detecting an interphase can be that the indenter width is so big compared to the interphase width that it cannot distinguish its contribution to the apparent elastic modulus value from that of copper. In order to verify this possibility, indentations were applied on the sample with 75 nm thick copper, where the indentation force was only 50 μ N. This is the minimum force that can be applied without having a significant influence from the surface roughness (Figure 4.12). This indentation force results in an indentation depth of \sim 65 nm and consequently an indentation width of \sim 490 nm according to equation (3.1). The accompanying stress zone would extend over twice this width which is \sim 980 nm. Therefore, for this measurement a space of 1 μ m was left between the adjacent indents, while the increment with which they approach the copper was 50 nm. The indentation imprints in this case are significantly smaller as shown in Figure 4.20.

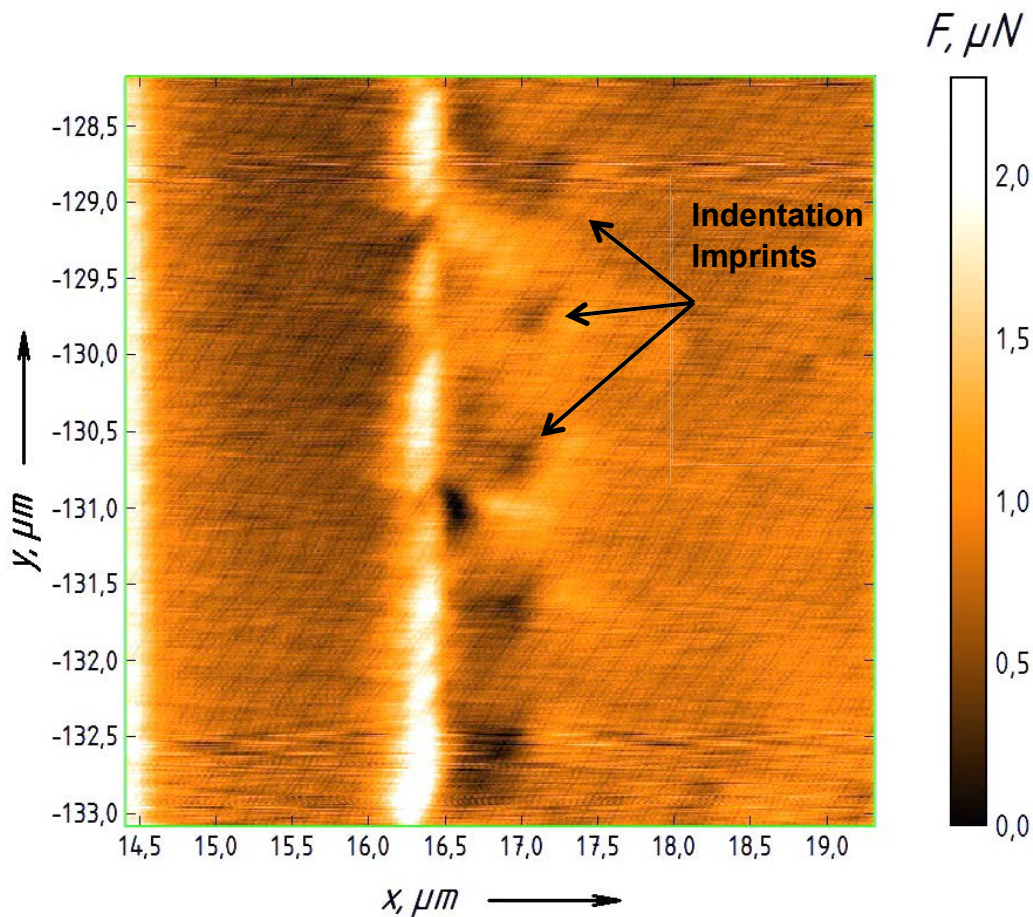


Figure 4.20: Imprints of 50 μN indentations approaching the copper interface with 50 nm increments.

The results of this experiment are shown in Figure 4.21. It can be seen that the influence of the copper is more pronounced in this case, as the magnitude of the apparent modulus peak is higher than in the case of the 0.2 mN indentations. This agrees with the FEM results when indentations were applied at different depths; the contribution of each phase to the value of the measured apparent elastic modulus becomes bigger when smaller indentations are applied. Similarly, if an interphase exists, it should be easier to detect when smaller indentations are applied. However, even in this case, the apparent modulus shows a symmetrical behavior around the copper as in the case of a perfect interface, which does not indicate the presence of an interphase of distinctive properties.

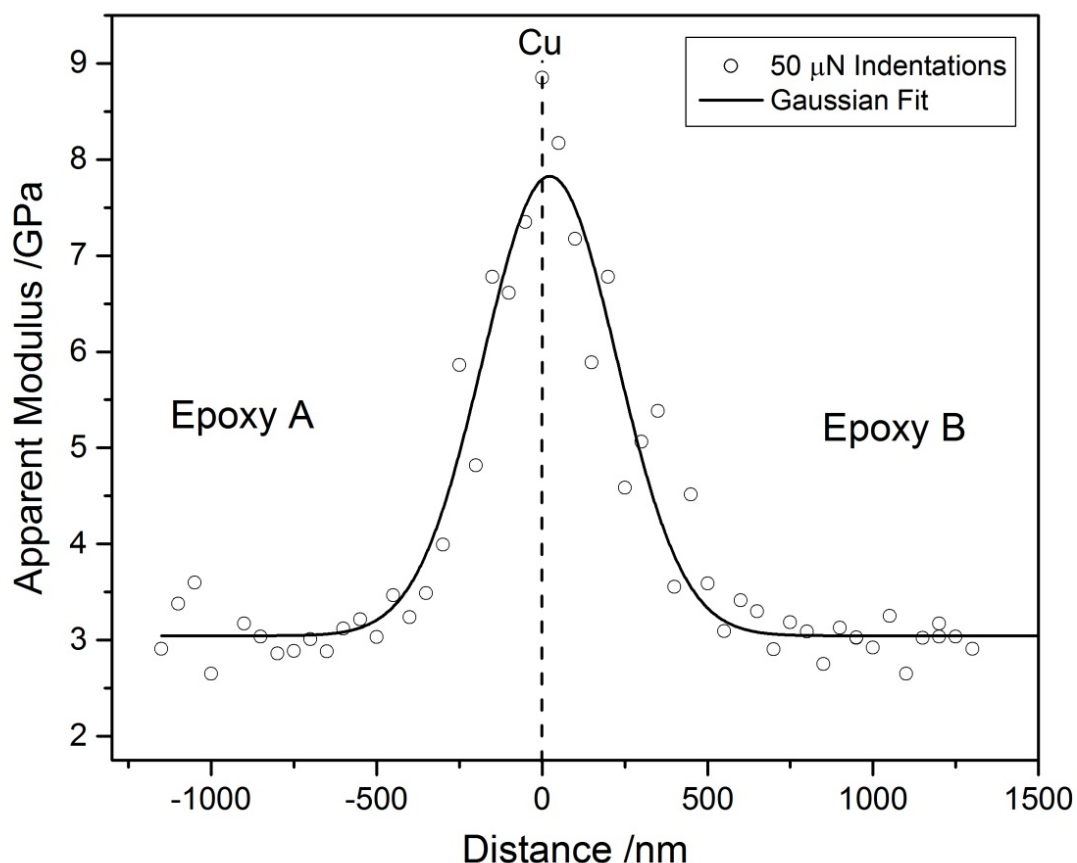


Figure 4.21: 50 μN indentations with a spacing of 50 nm performed across 75 nm thick copper.

Direct Investigation of the Interphase as a Function of Indentation Depth

Another reason why it was not possible to detect an interphase using nanoindentation can be the preparation method. As explained earlier, in order to obtain samples with a smooth continuous surface, the sample surfaces were cut using the microtome, which has proven efficient. However, there are some problems that may result from using the microtome to prepare the samples. For example, the microtome can be a source of surface induced stresses, especially around the edges of the sample.¹³⁰ In this case, those stresses would be more likely to build up at the copper interface, due to the large differences in material properties between copper and epoxy such as stiffness or coefficient of thermal expansion, which make the two materials react differently to the heat induced while cutting. Those stresses can distort the microstructure of the regions where they are induced, which is the interphase in this case.¹³⁰ Additionally, because the interphase in this system is expected to be softer than the bulk, it may get smeared by the microtome knife. The smearing of rubber (being the softer phase) in a rubber/polystyrene system by the microtome knife was reported by Williams and Hudson.¹³¹

In order to avoid the potential influences from the microtome on the interphase, a further modification was introduced to the already prepared sample. The two epoxy parts were separated from each other as shown in Figure 4.22, and the indentations were applied directly to both epoxy blocks on the surfaces parallel to the copper layer.

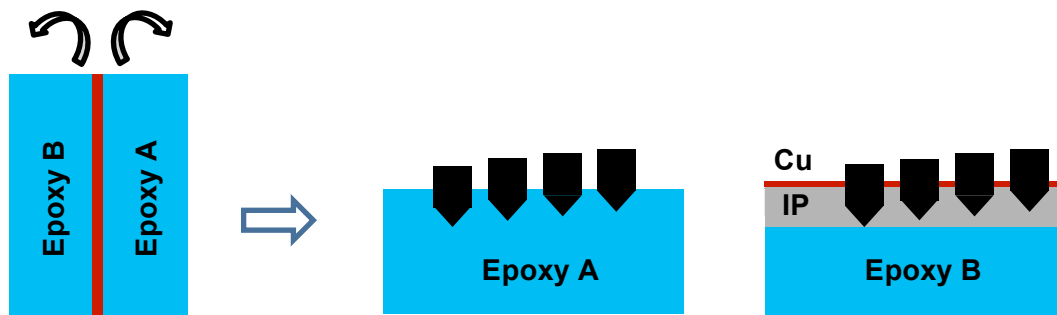


Figure 4.22: Separation of the two epoxy parts in order to investigate the interphase directly as a function of indentation depth

In order to minimize the influence of copper, another sample was prepared for this experiment with a copper thickness of ~ 10 nm only. It was observed that after separating the two epoxy blocks, the copper was transferred to the surface of epoxy B, which can be a sign of good bonding between the copper and the epoxy that cured while in contact with it.

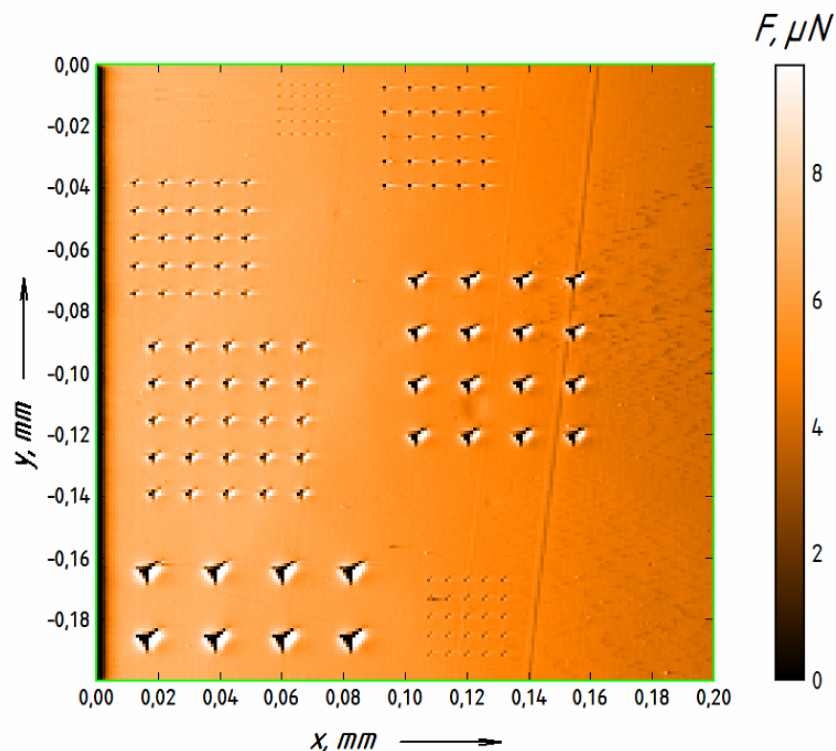


Figure 4.23: Multiple indentation series with different depths used for direct investigation of the interphase.

The indentations for this test were displacement-controlled; multiple series were performed at different indentation depths ranging from 100 nm to 1.3 μm . 25 indentations were applied for smaller indentation depths, while a fewer number of indentations was used for larger depths as the results become more consistent. The imprints of this experiment are shown in Figure 4.23.

It is important to note that this experiment would not provide quantitative information about the interphase thickness, as the influence of an indentation extends in the vertical direction over ~ 10 times the indentation depth.¹³² However, the experiment can give a relative idea whether a phase of different properties exists below the copper. The average calculated modulus for each indentation series is plotted versus the indentation depth for both epoxy parts and represented in Figure 4.24.

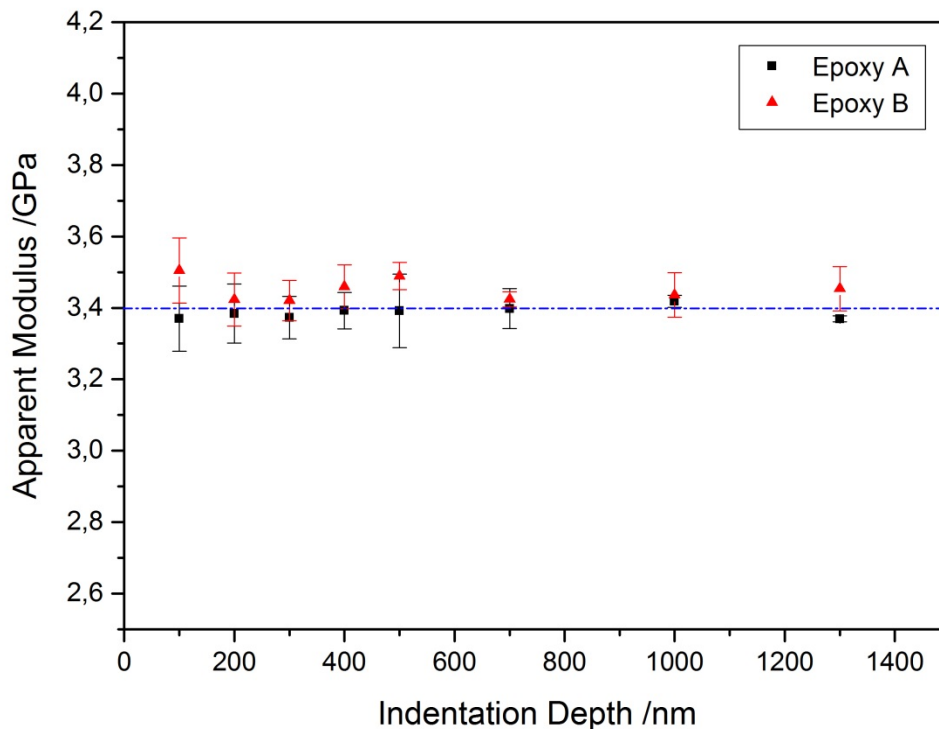


Figure 4.24: Apparent elastic modulus as a function of indentation depth for both sides of the amine-cured epoxy.

The results above show that epoxy A experiences very constant modulus values with different indentation depths, which is to be expected. The average of the modulus values from epoxy A at different depths is expressed by the dashed line. Similarly, epoxy B does not show any difference in the modulus values between the small indentations and the bigger ones. The

modulus values from epoxy B are slightly higher than those from epoxy A with a deviation of less than 3%, which can be caused by the copper. This agrees with the previous results of the indentations across the copper. They both suggest that in the used epoxy system, there is no interphase next to the copper.

AFM Results

AFM measurements were performed as a reference method for comparing with the nanoindentation results, since the tip used in AFM is much smaller than the Berkovich indenter and the contributions from other phases rather than the one being tested are minimal. Therefore, it should be easier to detect the interphase existence. The topography image of the epoxy/Cu/epoxy sample with a copper thickness of 20 nm is shown in Figure 4.25.

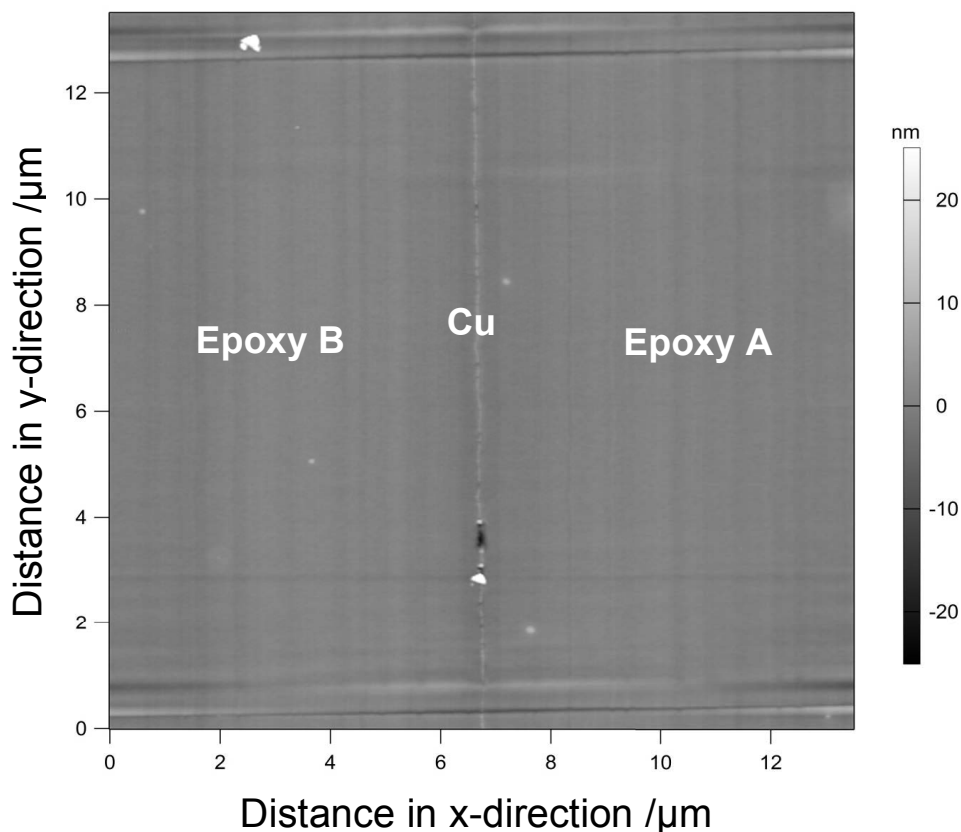


Figure 4.25: AFM topography image of the epoxy/Cu/epoxy sample with a copper thickness of 20 nm.

The stiffness map resulting from the force-distance measurements performed across the copper is presented in Figure 4.26. The indentations were performed at a distance of $\sim 1.3 \mu\text{m}$ from each other, where each point is represented by a pixel on the stiffness map.

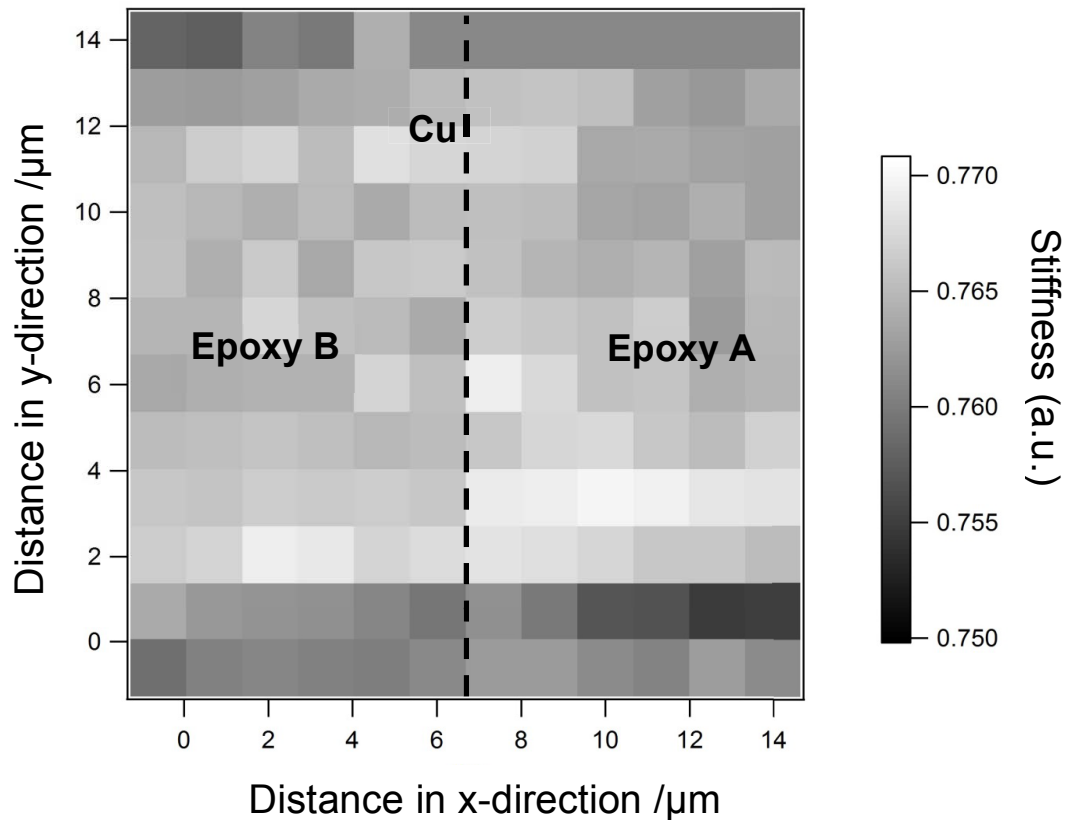


Figure 4.26: A stiffness map generated by applying AFM force-distance measurements across the copper.

The stiffness map above shows that the whole surface is quite homogeneous. Unlike the nanoindentation results, the copper does not show higher stiffness, this is because the copper layer is only 20 nm, while the distance between two test points is $\sim 1.3 \mu\text{m}$. In contrast with the Berkovich indenter, the AFM tip has a much higher aspect ratio, which means that the indentations are small enough that they do not get influenced by the copper, especially when such a relatively big distance is left between the adjacent points. In accordance with the nanoindentation results, there is no region of different stiffness next to the copper on the side of epoxy B, where the interphase is expected to form. This means that according to the applied AFM measurements, no interphase is formed in the vicinity of the copper. An interphase of distinctive properties might exist but it would only have a thickness of less than $1.3 \mu\text{m}$, since the distance between every two test points was $\sim 1.3 \mu\text{m}$. The results from the AFM combined with the different performed nanoindentation measurements, and in comparison with the FEM calculations, suggest that in the epoxy system being investigated, no interphase was formed between the epoxy and the copper.

4.4 Conclusion

The aim of this chapter was to verify the validity of the proposed model experimentally by using nanoindentation to investigate the interphase between copper and amine-cured epoxy. Samples were prepared in a way that allows having epoxy/Cu/epoxy sandwich structure, where the interphase is formed at only one of the two epoxy/Cu interfaces. Moreover, a method was successfully developed which allows applying multiple indentations across the copper interface without overlap. The preliminary results showed that the indenter asymmetry around the copper can be a major source of error and needs to be taken into account. Otherwise, different mechanical property values would be measured at both sides of the copper due to the indenter geometry asymmetry.

The indenter geometry was adjusted to be oriented symmetrically around the copper and nanoindentation was successfully applied across the interface line without overlap. In accordance with the FEM results, the copper layer with a thickness of 100 nm showed a constriction effect on the indentations in its vicinity. However, decreasing the layer thickness down till 20 nm did not help avoid this constriction effect. In contrast with other studies that reported the formation of a softer interphase between amine-cured epoxy and copper, none of the samples with the different copper thicknesses showed any signs of interphase existence, even when indentations were applied with a depth of only ~65 nm and a spacing of 50 nm in between. Moreover, the AFM measurements in force-distance mode with increments of ~1.3 μm did not show any stiffness variations across the copper.

In order to rule out the possibility that preparing the samples with the microtome did not damage the surface structure somehow, the two epoxy blocks were separated and multiple series of nanoindentation tests were applied perpendicular to the interphase at different indentation depths. This experiment as well did not show any change in the mechanical properties with different indentation depths from the surface, which confirms that in the used epoxy system and in contrast with other studies in the literature, no interphase was formed with the copper. The curing parameters of the epoxy seem to have a huge influence on the formation of the interphase as well as its final width. This will be discussed in detail and verified in the next chapter.

5

Characterization of the Interphase in an Anhydride- cured Epoxy/Copper System

5.1 Introduction

In the literature, there are drastic differences between the reported thicknesses of epoxy interphases, depending on the matrix/reinforcement system, the curing parameters and the measurement technique. For example, Bogetti et al.¹¹⁰ reported an interphase with a thickness of only 3 nm between amine-cured epoxy and unsized carbon fibers, while Munz⁴⁶ reported an interphase thickness that is as wide as $\sim 234.7 \mu\text{m}$ between amine-cured epoxy and polyvinylpyrrolidone (PVP).

This also applies to the case of epoxy/Cu interphases; different thicknesses are reported in the literature, sometimes even for the same epoxy system and the same measuring technique. For instance, the thickness of the interphase between copper and an epoxy system composed of a DGEBA resin and an aliphatic/cycloaliphatic amine-based curing agent was reported to be $\sim 1.9 \mu\text{m}$ by Chung et al.,⁵⁸ while it was found to be only $\sim 280 \text{ nm}$ by Munz et al.,¹³³ where both studies used the AFM-FMM technique. However, there were two main differences between the two studies: the preparation method and more importantly the curing conditions. In the first study, mixing was performed at $80 \text{ }^\circ\text{C}$ for at least 7 minutes, followed by curing for 2 hours at $130 \text{ }^\circ\text{C}$, while in the second study, the mixture was mixed and cured at $50 \text{ }^\circ\text{C}$. Moreover, using the same curing conditions, Munz et al.⁶⁷ similarly used AFM-FMM to investigate the interphase between copper and the same epoxy system but from another supplier. This time, an interphase that is as wide as $\sim 29.4 \mu\text{m}$ was reported. Despite the variation in the reported interphase thicknesses, the interphases from all three studies were found to be softer than the bulk epoxy. Table 5.1 summarizes the curing temperature used in the three studies mentioned above and the measured interphase thicknesses. The table shows that different systems can result in interphases with considerably different thicknesses even under the same curing conditions. Moreover, the same system can result in different interphase thicknesses by only altering the curing temperature. This suggests the presence of different kinetics, even though the driving force for interphase formation in different systems is the same (e.g. the preferential adsorption of the amine molecules onto the copper surface).

Table 5.1: Epoxy/Cu interphase thicknesses reported in different studies, all using DGEBA based resins and aliphatic/cycloaliphatic amine-based hardeners.

Epoxy System	Curing Temperature (°C)	Interphase thickness (µm)
EPIKOTE 828/ Epikure F-208 ⁵⁸	130	1.9
EPIKOTE 828/ Epikure F-208 ¹³³	50	0.28
L180/H181 ⁶⁷	50	29.4

Furthermore, the values in the table above suggest a correlation between the curing temperature and the interphase thickness for the same kind of epoxy/Cu systems. The system we used and presented in chapter 4 was also consisting of a DGEBA-based epoxy resin and an aliphatic/cycloaliphatic curing agent. However, in contrast with the studies presented above, the system was cured at room temperature, which can be an explanation of why no interphase was indicated.

Different studies have investigated the relation between different kinetics and the interphase formation. For instance, the final width of the concentration gradient at the interface was reported to be strongly affected by the ratio between the curing rate and the diffusion rate, defined as the Damköhler number.^{51,65} Palmese and McCullough⁵¹ employed thermodynamic and kinetic treatments in order to analyze the role of preferential adsorption and diffusion in the formation of interphase regions in thermosetting composites. They defined two different time variables: the characteristic time for diffusion, t_d , which is related to the average diffusivity for a specified isothermal cure temperature prior to vitrification, and the characteristic time for reaction in the bulk, t_{rb} , which represents the time necessary for vitrification at a given isothermal temperature. They discussed the interphase formation at three different possible situations as expressed in Table 5.2. The first situation is when $t_d \ll t_{rb}$. In this case, no concentration gradients would survive. Hence, the average concentrations will match the local concentrations. Similarly, when $t_{rb} \ll t_d$, time would not be enough for gradients to form before vitrification. They suggested that the only condition under which an interphase can form is when the characteristic times for diffusion and reaction are of the same order; i.e. $t_d \approx t_{rb}$.

Table 5.2: The relation between different reaction regimes and the interphase formation.⁵¹

Condition	Effect	Explanation
$t_d \ll t_{rb}$	No Interphase	Fast rearrangement following adsorption
$t_d \approx t_{rb}$	Interphase	Gradients frozen in place upon vitrification
$t_{rb} \ll t_d$	No interphase	Not enough time for gradients to form before vitrification

Since the system we investigated in chapter 4 was cured at room temperature, it is most probable that the third condition in the table above applies to the system. The relatively low temperature resulted in a relatively long characteristic time for diffusion compared to the curing time, too long that it was not enough to form a concentration gradient before vitrification occurs. Consequently, no interphase was formed, which explains why no difference in mechanical properties was monitored next to the copper.

In their study, Aufray and Roche¹³⁴ suggested that in order to obtain a thick interphase, the liquid monomer mixture should be left in contact with the surface of the metal solid for a few hours before starting the curing cycle. A major difference, however, between the epoxy system they used and the amine-cured system used in this work is that in their case, curing started when the temperature was raised above room temperature, while in our system curing starts as soon as the monomers are mixed together (the system has a pot life of only 0.5-4 hours).¹³⁵ The polymerization reaction and the interphase formation reaction are in competition, they need to be studied simultaneously when the interphase thickness is of concern.

Since the amine-cured epoxy that was used in this work did not show any signs of interphase existence in contrast with the reported studies in the literature, it was necessary to introduce another epoxy system where an interphase is more likely to be formed in order to verify the validity of our model experimentally. The chosen new epoxy system is an anhydride-cured epoxy system. It has some major differences compared to the amine-cured epoxy represented in chapter 4. For instance, it has a much longer pot life and it cures only at elevated temperatures. Other differences will be illustrated in detail throughout this chapter.

When anhydride/epoxy systems are cured while in contact with copper, the anhydride-based curing agent is also known to adsorb preferentially onto the copper surface. Boerio and Ondrus⁶⁴ investigated the interphase formation in epoxy/anhydride adhesives on different

metal substrates. They found that the anhydride adsorbed onto the surface of aluminum oxide substrates forming surface carboxylates. However, when brought into contact with a copper substrate, the anhydride curing agent not only reacted with the cuprous oxide (Cu_2O), but the cuprous ions were further removed from the oxide and oxidized, forming a thick film of carboxylate salt at the interphase which was described as a weak boundary layer.

Anhydrides exhibit slow curing kinetics below temperatures as high as 200 °C. For moderate curing conditions, the addition of accelerators such as imidazoles is required.^{29,30} However, when an anhydride/epoxy/imidazole system cures while in contact with a copper surface, the imidazoles are known to react with copper in a coordination reaction instead of acting as an accelerator in the ring opening reaction.¹³⁵ This behavior contributes as well to the formation of an interphase of distinctive properties between the epoxy and the copper.

In this chapter, the same experiments performed in the previous chapter on the amine-cured epoxy system will be performed on the anhydride-cured system. The results will be compared to the FEM model as well as to other studies in the literature.

5.2 Experimental Work

Materials

The epoxy used in this study is an anhydride-cured epoxy system which consists of Araldite[®] LY 556 resin, HY 917 hardener, and DY 070 accelerator (all provided by Ciba Specialty Chemicals). The epoxy system is described by the supplier as a low-viscosity system with an extremely long pot life (165-175 hours at room temperature).¹³⁶ Some specifications of the system components are provided in Table 5.3.

Table 5.3: Specifications of the used epoxy resin, anhydride-based hardener and accelerator.¹³⁶

	Resin Araldite[®] LY 556	Hardener HY 917	Accelerator DY 070
Density at 25 °C [g/cm³]	1.15-1.2	1.20-1.25	0.95-1.05
Viscosity at 25 °C [mPas]	10000-12000	50-100	≤ 50
Epoxy value [equivalent/Kg]	5.30-5.45	-	-

The Araldite[®] LY 556 is a DGEBA-type resin, the HY 917 is a methyl-tetrahydrophthalic anhydride hardener, and the DY 070 is a 1-methyl imidazole accelerator.¹³⁷

Sample Preparation

Similar to the case of the amine-cured epoxy, a sample was prepared in a way that allows having epoxy/Cu/epoxy structure with an interphase on only one epoxy side. The first step is to prepare the first epoxy part (epoxy A), which will act layer as a substrate for the copper layer. The resin, the hardener and the accelerator were mixed with a ratio of 100:90:0.5 by weight. As recommended by the supplier, the hardener and the accelerator were premixed to allow the use of two component mixing/metering equipment. Afterwards, the resin is added and the mixture is homogenized by vigorous stirring for 10 min.¹³⁶

Since in this case heating at elevated temperatures is required, a silicon mold was used to cast the sample. The silicon mold was cube shaped with an inner side dimension of 25 mm. For preparing the epoxy A part, only half the mold was filled with the liquid mixture and placed in the oven. The curing cycle included heating at 80 °C for four hours after which gelation occurs, followed by another four hours of heating at 120 °C to finalize curing. The temperature was high enough to evaporate any present bubbles and moreover, the free surface that was exposed to the air ended up being quite smooth after curing. This surface was then sputtered with copper (half the surface was covered as explained in chapter 4) according to the parameters in Table 4.2, in order to achieve a layer thickness of only 10 nm. The sputtered sample was again placed in the silicon mold, another epoxy liquid mixture was prepared (epoxy B) and cast to fill the rest of the mold. And the whole structure was again placed in the oven and experienced the same curing cycle.

The final epoxy/Cu/epoxy sample was displaced from the silicon mold, and prepared using the microtome in the same way and using the same parameters explained in the experimental work section in chapter 4.

Nanoindentation and AFM Measurements

The nanoindentation and AFM measurements were applied using the same instruments and the same procedure explained in chapter 4. The exact parameters such as the indentation depth or the spaces between the indentations will be mentioned in the results and discussion section.

5.3 Results and Discussion

Nanoindentation across Copper

Nanoindentation was applied across the copper layer from epoxy A to epoxy B in a similar manner to the procedure followed for testing the amine-cured epoxy. In this case, all the measurements were applied on a sample with a 10 nm thick copper layer. The first indentation series was applied using a force of 0.2 mN, resulting in indentations depths in the range of 150 nm. According to equation (3.1), this results in an indentation width of $\sim 1.1 \mu\text{m}$. Therefore, a space of $2.3 \mu\text{m}$ was left between two adjacent indents, which is larger than twice the indentation width. The increment with which the indentations approached the copper was 200 nm. The resulting variation in apparent elastic modulus values is represented in Figure 5.1. The data points are smoothed by 3 points using the adjacent-averaging method.

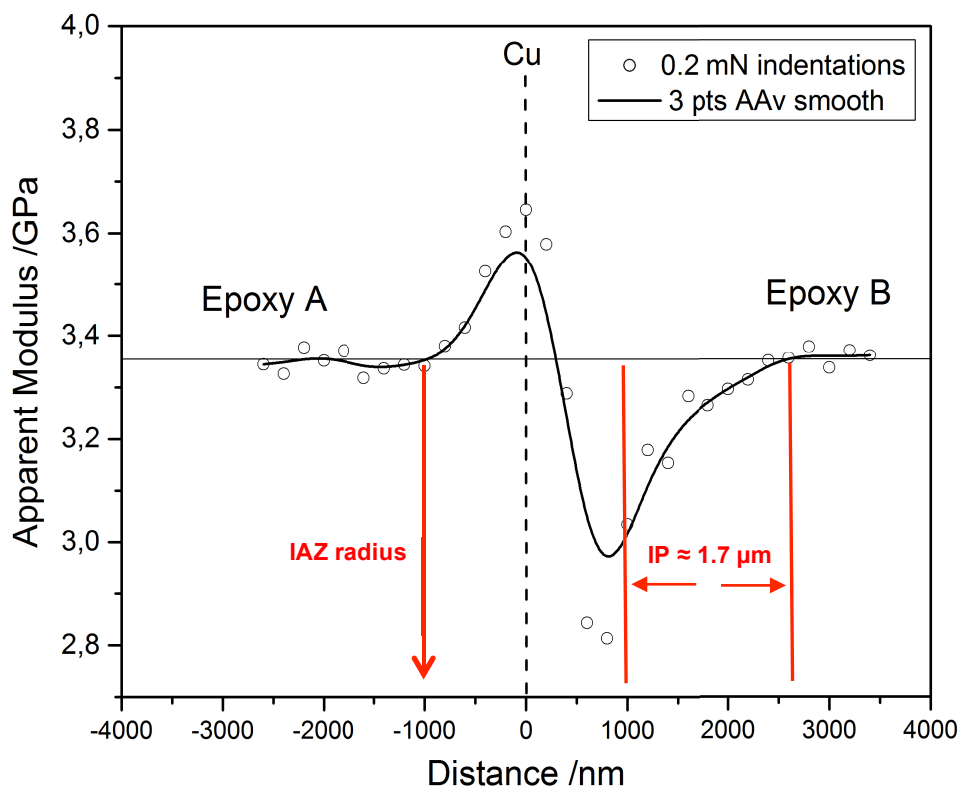


Figure 5.1: Apparent elastic modulus variation resulting from 0.2 mN indentations across the copper with 200 nm spacings.

The first thing that could be noticed is the peak around the copper. This peak shows that the copper with a thickness of only 10 nm still restricted the indentations in its vicinity. This

effect starts at a distance of $\sim 1 \mu\text{m}$ from the copper on the side of epoxy A. The IAZ should be around $2.2 \mu\text{m}$, which is double the indentation width according to Hodzic et al.¹⁵ Accordingly, the IAZ radius is in the range of $1.1 \mu\text{m}$, which is very close to the point at which the stiffness starts increasing in the curve above.

The second thing, and in contrast with the symmetrical curves obtained from the amine-cured epoxy (Figure 4.19), there is a drop in the apparent elastic modulus next to the copper peak on the side of epoxy B. This drop is similar to the curves obtained from the FEM when a softer interphase was introduced (Figures 3.12 and 3.15). In accordance with literature, this suggests the presence of a soft interphase next to the copper layer on the side of epoxy B, which was cured while in contact with the copper. Moreover, by applying the analysis explained in chapter 3, it should be possible to estimate the thickness of this interphase. As illustrated in Figure 5.1, the IAZ radius can be determined from the side of epoxy A, which is around $1 \mu\text{m}$. By mirroring this point on the side of epoxy B, the region at which the IAZ interacts with copper can be excluded. This means that any variations from the bulk starting from 800 nm away from the copper are caused solely by the interphase. As the indentations are applied further from the copper, the apparent modulus value starts increasing until it reaches the bulk value at a distance of $2.7 \mu\text{m}$ away from the copper. By subtracting the distance where IAZ was restricted by the copper ($1 \mu\text{m}$), we obtain the interphase thickness which is $\sim 1.7 \mu\text{m}$.

In order to confirm the results, two other series of indentations were performed across the copper with different parameter. The first indentation series was applied using a force of 0.1 mN , resulting in indentation depths around 95 nm and according to equation (3.1) an indentation width of $\sim 715 \text{ nm}$. Therefore, a space of $1.5 \mu\text{m}$ was left between the adjacent indentations to avoid overlapping, and the indentations approached the copper with an increment of 150 nm . The second indentation series was applied using a force of 0.08 mN only, which resulted in indentations with a depth of around 80 nm and an indentation width of $\sim 600 \text{ nm}$. Therefore, a space of $1.3 \mu\text{m}$ was left between the adjacent indentations and the indentations approached the copper with an increment of 100 nm . The data from both series were smoothed by three points using the adjacent-averaging method. The results from the two series are shown in Figures 5.2 and 5.3.

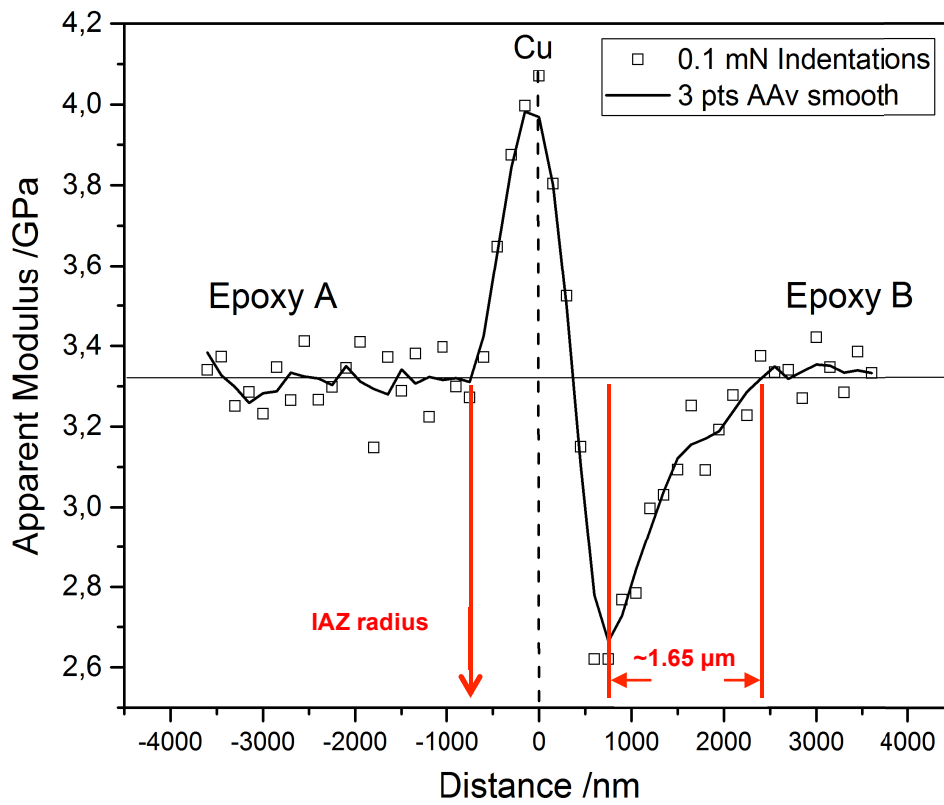


Figure 5.2: Apparent elastic modulus variation resulting from 0.1 mN indentations across the copper with 150 nm spacings.

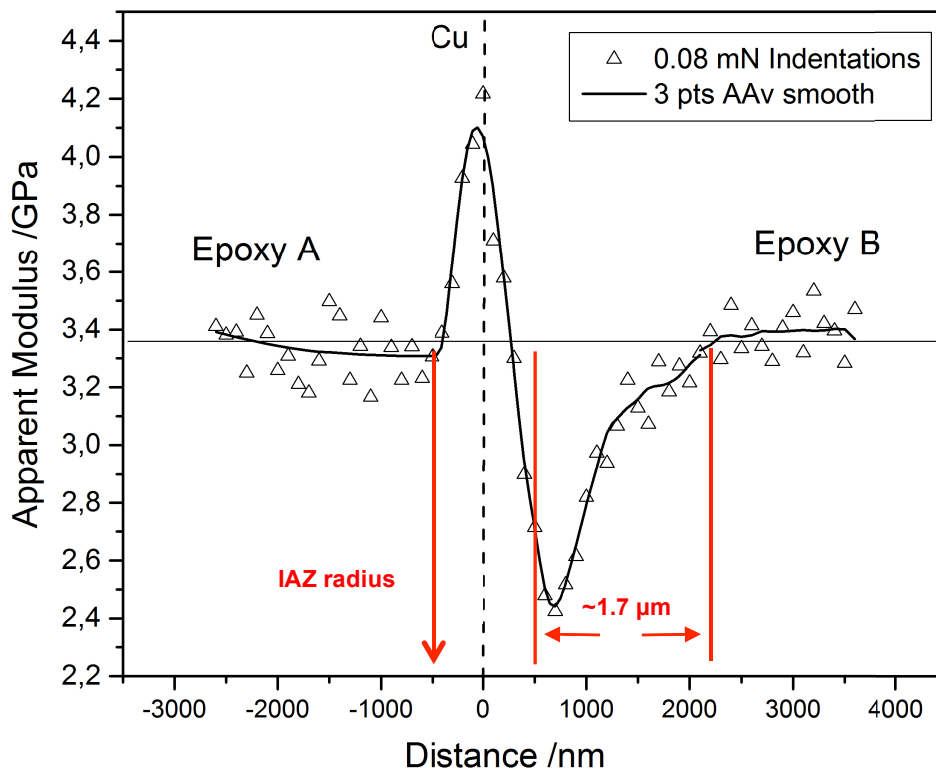


Figure 5.3: Apparent elastic modulus variation resulting from 0.08 mN indentations across the copper with 100 nm spacings.

By applying the analysis explained earlier using FEM on the results from the indentation series above, it is possible to estimate the interphase thickness. In the case of the indentations performed using a force of 0.1 mN, the value of the apparent modulus started increasing from the bulk at a distance of ~ 750 nm from the copper on the side of epoxy A. This value corresponds to the radius of the IAZ, and by mirroring it to the side of epoxy B it is possible to determine the point at which the indenter is not influenced by the copper anymore. Starting from this point and up till the values of the apparent elastic modulus reach the bulk values again, the interphase thickness can be estimated to be around $1.65 \mu\text{m}$. By applying the same procedure to the data obtained from the 0.08 mN indentations, an interphase thickness of around $1.7 \mu\text{m}$ can be determined.

In those two indentation series, the distances from the copper at which the modulus values started increasing correspond to the radius of the stress zone surrounding the indenter. The experiments showed that in both cases, and similar to the first series, the extent of the IAZ was very close to twice the indentation depth as suggested by Hodzic et al.¹⁵ Moreover, the three indentation series prove that a softer interphase exists next to the copper, in agreement with other studies in the literature.^{58,67,133} The interphase thickness is estimated to be $\sim 1.7 \mu\text{m}$. It is worth mentioning that the closest value of interphase thickness reported in the literature is $1.9 \mu\text{m}$ in the work of Chung et al.⁵⁸ Although the system used in their study was an amine-cured epoxy, the curing cycle in their work (mixing at 80°C followed by curing for at 130°C) was the most similar to the one applied in our study (80°C followed by post curing at 120°C). As explained in the introduction of this chapter, the curing parameters are crucial in determining the final interphase thickness. The interphase thickness of anhydride/epoxy systems cured while in contact with copper is barely reported in the literature.

The results above verify the validity of our model as well as the indentation application method. Moreover, it shows that regardless of the indentation parameters (indentation depth or spaces between indents), it is possible to determine the interphase thickness. However, applying smaller indentations with smaller spacings can make the contribution of the interphase properties to the measured apparent modulus values more pronounced, which can be noticed from the increasing minimum values of the measured apparent elastic modulus with decreasing the indentation depth.

Although most nanoindentation instruments are force-controlled,⁸⁸ force control may affect the indentation depth and consequently the IAZ radius, possibly leading to unreliable results. In order to check for this, a similar series of indentations was applied on a sample with a 40 nm thick copper layer. This time, the indentations were displacement-controlled; the indentation depth is constant and the force changes accordingly. The indentations had a depth of 200 nm, spacings of 3 μm , and approached the copper with increments of 200 nm. The results are shown in Figure 5.4

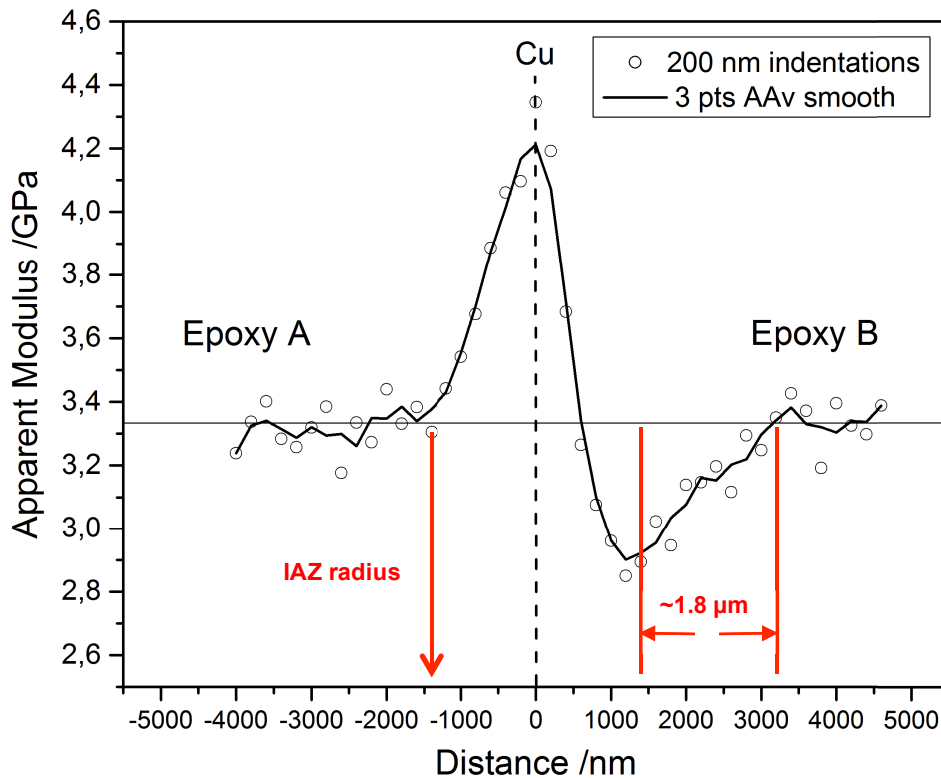


Figure 5.4: Apparent elastic modulus variation resulting from 200 nm indentations with 200 nm spacings, applied across 40 nm thick copper.

The plot above shows that the constriction effect exhibited by the copper layer is more pronounced in this case due to its larger thickness (40 nm compared to 10 nm in the previous measurements). Moreover, the 200 nm indentations resulted in an IAZ with a radius of $\sim 1.4 \mu\text{m}$. By following the same analysis procedure, an interphase with a thickness of $\sim 1.8 \mu\text{m}$ can be measured, which is very close to the thickness values obtained from the force-controlled measurements. This shows that the force-controlled measurements, even with possible relative IAZ radius variations, were still reliable in determining the interphase thickness

Direct Investigation of the Interphase as a Function of Indentation Depth

Similar to the amine-cured epoxy, and in order to exclude the possibility that the obtained results might be caused by any microtome-induced artifacts, the two sides of the epoxy were separated and the indentations were applied at different depths perpendicular to the interphase. The exact procedure was explained in section 4.3. It is worth mentioning that in this case and in contrast with the amine-cured epoxy, the copper was still sticking to the epoxy A block after separation, which can be a sign of poor adhesion between the copper and epoxy B. The average calculated modulus for each indentation series is plotted versus the indentation depth for both epoxy parts and represented in Figure 5.4. It can be seen that the scattering of the indentation values from smaller indentations (100 nm) on epoxy A is in the same range of the peak caused by the indentations across the copper in Figure 5.1 (~200 MPa). Moreover, it was previously reported that by increasing the indentation depth on a stiff film/soft substrate system, the measured mechanical properties start decreasing gradually from indentation depth equal to 0.25 the film thickness.¹³⁸ In this case, the indentation depth is at least 10 times the film thickness. These reasons may explain the lack of a significant influence of copper in the plot below.

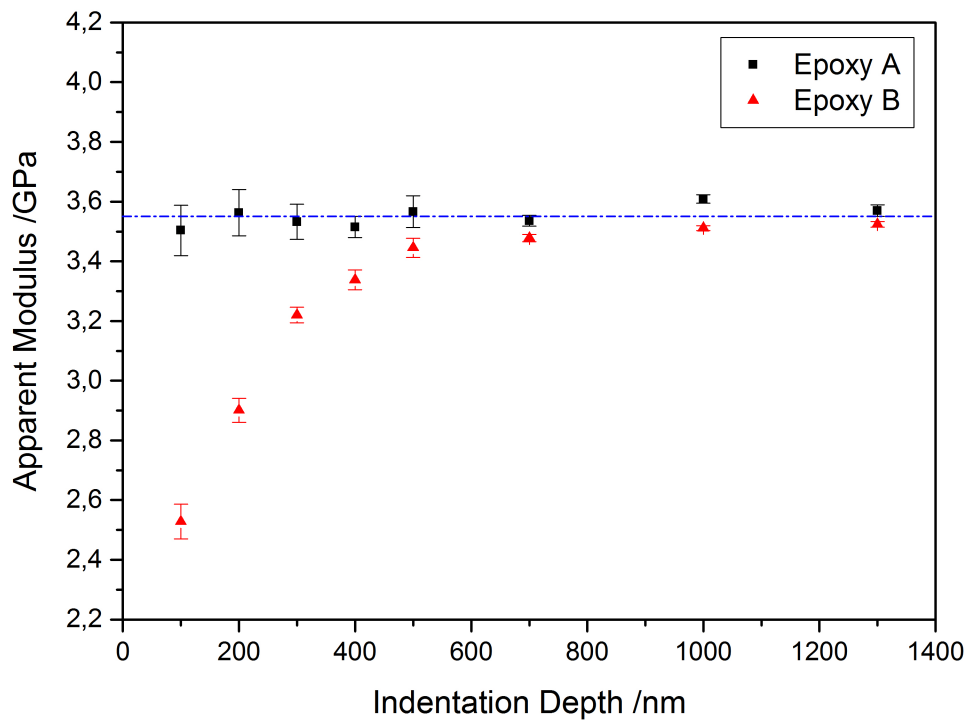


Figure 5.5: Apparent elastic modulus as a function of indentation depth for both sides of the anhydride-cured epoxy.

Figure 5.4 shows a significant difference between the behaviors of both epoxy parts in response to different indentation depths. While epoxy A is showing steady apparent modulus values, epoxy B is exhibiting a plateau that increases until it reaches a steady value starting from ~ 700 nm. This means that epoxy B exhibits lower stiffness values closer to the surface; i.e. closer to the interphase. Although these results cannot provide concrete information about the interphase thickness, it confirms the presence of an interphase that is softer than the bulk. In addition, it rules out the possibility that the obtained results from the indentations across the copper might be due to artifacts caused by the microtome knife while preparing the samples.

AFM Measurements

As a reference method, AFM measurements were applied across the copper as explained in chapter 4. The resulting topography image is shown in Figure 5.5.

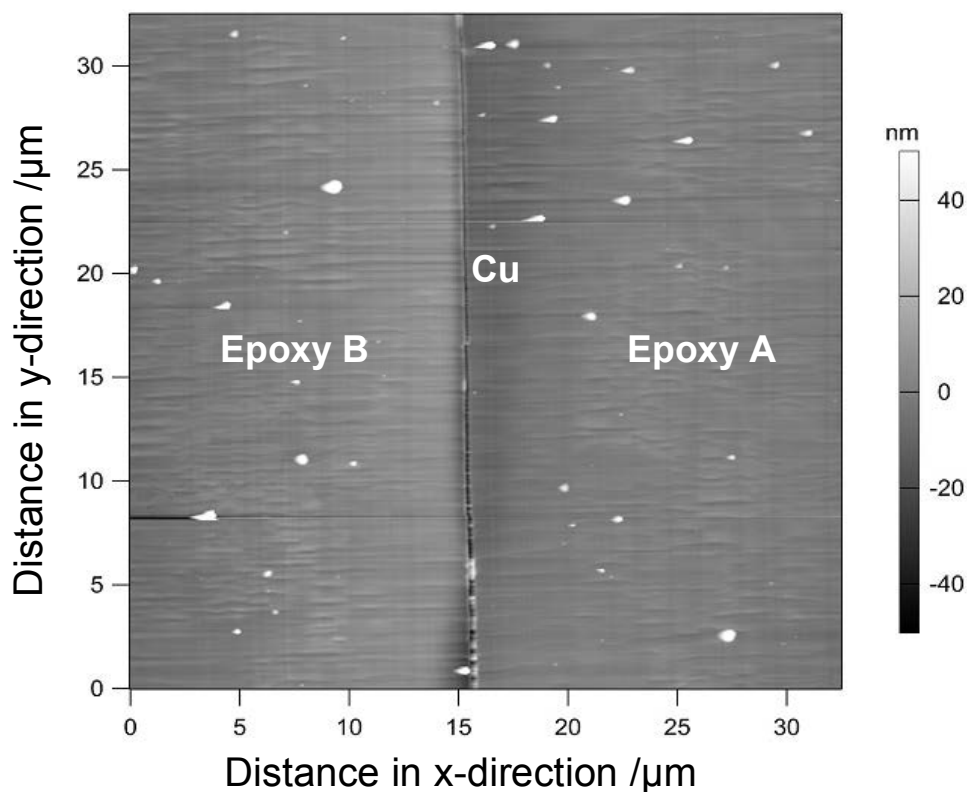


Figure 5.6: AFM topography image of the epoxy/Cu/epoxy sample with a copper thickness of 10 nm.

The corresponding stiffness map resulting from the force-distance measurements performed across the copper is presented in Figure 5.6. The indentations were performed at a distance of 1 μm from each other; each point is represented by a pixel on the stiffness map.

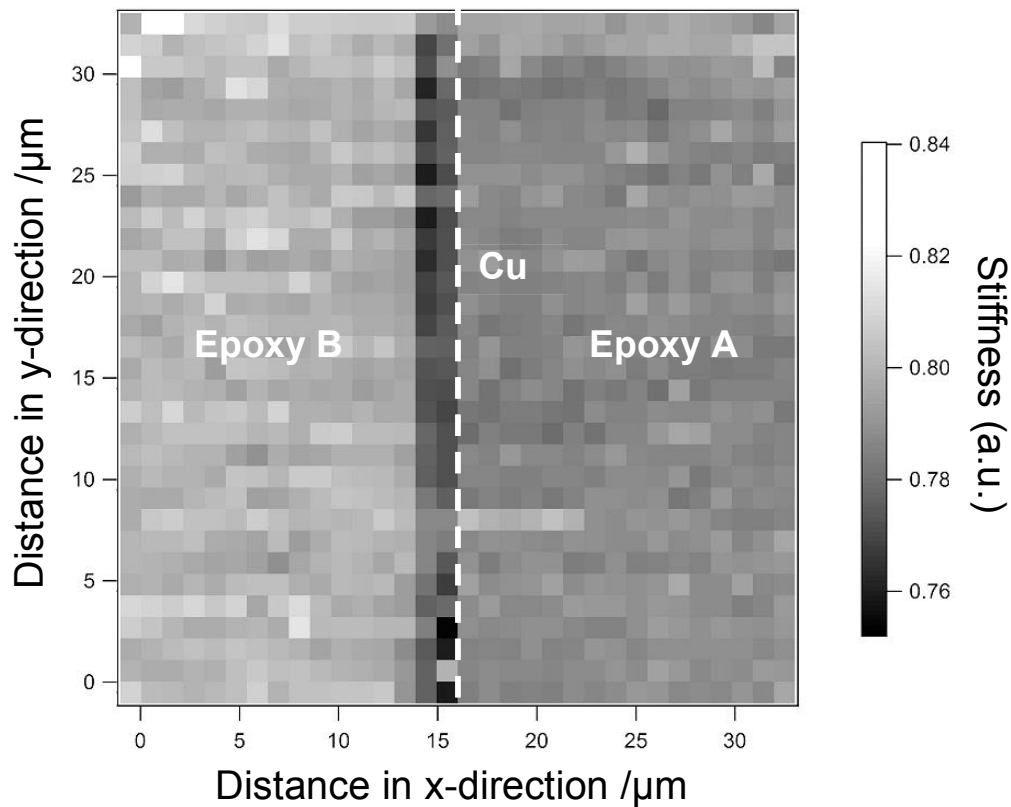


Figure 5.7: A stiffness map of the anhydride-cured samples generated by applying AFM force-distance measurements across the copper.

The stiffness map presented above shows that in the vicinity of the copper on the side of epoxy B, a region of lower stiffness exists which extends over two pixels. Since the distance between each two test points was 1 μm , it can be concluded that the interphase thickness is somewhere between 1 and 2 μm , which agrees with the nanoindentation results that showed an interphase of $\sim 1.7 \mu\text{m}$ thickness. The aim of this AFM measurement was mainly for comparison with the nanoindentation results and confirming that a softer region exists in the vicinity of the copper on the side of epoxy B, which was successfully achieved. However, for an accurate estimation of the interphase thickness using AFM, the distance between two test points should be decreased.

5.4 Conclusion

In this chapter, an anhydride-cured epoxy system was introduced in order to verify the ability of our proposed model to investigate the thickness and properties of epoxy/Cu interphases. A major difference between this system and the amine-cured epoxy investigated in chapter 4 is the curing parameters. This system has a much longer pot life and cures only at elevated temperatures. In addition, the thickness of the copper layer was further decreased to only ~10 nm.

The nanoindentation experiments showed the copper layer with a thickness of only 10 nm still restricted the indentations in its vicinity. However, our proposed model proved to be efficient in determining the thickness of the interphase regardless of the copper constriction effect. A softer interphase of around ~1.7 μm was detected between the anhydride-cured epoxy and the copper on the side of epoxy B. Moreover, the nanoindentation results showed that a great advantage of the proposed model is that it is efficient regardless of the indentation parameters such as the indentation depth, as it was possible to determine the interphase thickness with indentations as deep as ~150 nm. AFM measurements in force-distance mode were also applied as a reference method for comparison. The distance between the adjacent test points across the copper was as large as 1 μm . However, a region of lower stiffness was detected by 2 test points next to the copper, which confirms the presence of a softer interphase with a thickness in the range of 1 to 2 μm . For an accurate determination of the interphase thickness using AFM, the distance between the tested points should be decreased.

The possibility that the measured variation in mechanical properties might be an artifact caused by the microtome knife was ruled out. The epoxy blocks were separated and the interphase was investigated as a function of the indentation depth. A plateau was found on the side of epoxy B, which was cured while in contact with copper. This plateau starts with low modulus values at lower indentation depths, and increases until it reaches the bulk values at larger indentation depths (around 700 nm). Although this kind of measurement does not provide quantitative information about the interphase thickness, it confirms the presence of a softer interphase.

6

Concluding Remarks

With the growing role of composites in a wide range of applications, special attention is being paid to interphases, as it is believed that the size and properties of the interphase can be determinant of the performance of the whole composite. However, a direct mechanical characterization of the interphase region can be limited by the relatively small size of the interphase.

The main aim of this research was to extend and to assess the applicability of nanoindentation for investigating the size and properties of interphases in polymer/metal composites in general and in epoxy/copper composites as a particular case. In order to fulfill this aim, an epoxy/Cu/epoxy system was proposed, where the thickness of the copper layer is in the range of only 100 nm or less, and where one epoxy/Cu side (epoxy A) has a perfect interface, while the other side (epoxy B) forms an interphase with the copper. The two hypotheses behind this system were: First, the copper, with such a small thickness, will not have a constriction effect on the indentations in its vicinity. Second, when the interphase is located at only one side of the copper, the other side can be used as a reference for detecting any variations in the mechanical properties caused by the constriction effect and not the interphase itself. Thus, these effects can be excluded from the measured property variations on the interphase side.

The first step was to verify the validity of the proposed system using FEM. A 3D FEM model was generated with an epoxy/Cu/epoxy structure, where the copper had a thickness of 100 nm. A 400 nm thick region that is softer than the epoxy was inserted on one side of the copper to resemble the interphase. The FEM results showed that copper with a thickness of only 100 nm was still restricting the indentations in its vicinity. However, using the side of epoxy A as a reference, it was possible to determine the extent of the indent affected zone (IAZ). This information was further applied to the side of epoxy B to determine the point at which the IAZ is not influenced by the copper anymore, and it was successfully possible to determine the region that is solely influenced by the interphase properties. Due to the relatively large indentation width, the measured properties at different points include contributions from multiple phases in the system, which makes it difficult to detect the absolute mechanical properties within the interphase. However, the calculations showed that by decreasing the indentation depth it is possible to intensify the single contribution from each phase in the system to the measured values, which can be useful in highlighting the contrast between the interphase properties and the bulk.

In order to verify the proposed system experimentally, samples were prepared in a way that allows having an epoxy/Cu/epoxy structure with the interphase being on only one side. The system used was an amine-cured epoxy that cures at room temperature, and the deposited copper layers were in the range of 20-100 nm. A method that allows applying multiple indents in the region of interest without overlap was successfully developed. Preliminary results showed that the Berkovich indenter needs to be oriented symmetrically around the copper interface. Otherwise, it can lead to measuring different properties at both sides of the copper that are caused solely by the indenter asymmetry.

In accordance with the FEM calculations, the nanoindentation measurements showed that the copper with a thickness of only 100 nm does restrict the indentations in its vicinity, which was represented by an increase in the mechanical properties around the copper. Moreover, decreasing the copper thickness to 20 nm did not help eliminate this effect. Surprisingly, however, no signs of interphase existence were detected on the side of epoxy B from the different samples, as the obtained curves were quite symmetrical around the copper. This behavior did not change when the indentation depth and the spaces between them were reduced down to 60 and 50 nm, respectively. In accordance with the nanoindentation results, the stiffness maps generated by AFM did not show any stiffness variations across the copper. In order to rule out the possibility that the microtome knife might have distorted the interphase structure, the epoxy/Cu/epoxy samples were separated at the interface and indentations were applied perpendicular to the interface plane, so that the interphase can be investigated as a function of indentation depth. The results from this experiment as well did not show any difference between the indentations applied on both epoxy blocks at different depths. Taken together, the results mentioned above suggest that in the system being investigated, no interphase was formed between the epoxy and the copper.

The proposed model was applied on another epoxy system that is anhydride-cured. Unlike the first system, the anhydride-cured epoxy required heating at elevated temperatures to be cured. In addition, the thickness of the copper layer was further reduced to only 10 nm. Although this minimized the mechanical influence of the copper on the indenter, it did not eliminate it totally. However, in contrast with the amine-cured epoxy, a softer region was detected next to the copper on the side of epoxy B, which refers to the formation of a soft interphase region between the epoxy and the copper. By determining the extent of the IAZ using epoxy A side,

and excluding its interaction with the copper on epoxy B side, it was possible to determine that the interphase had a width of $\sim 1.7 \mu\text{m}$. Determination of the interphase thickness was possible by performing indentations as deep as $\sim 200 \text{ nm}$ and spaces as wide as 200 nm in between. By reducing the indentation depth as well as the spacing between the indentations, it was possible to make the stiffness variations caused by the interphase more pronounced.

The AFM measurements confirmed the existence of a softer interphase next to the copper. In accordance with the nanoindentation results, the interphase thickness was determined to be in the range of 1 to $2 \mu\text{m}$. The distance between the adjacent test points was $1 \mu\text{m}$. For a more accurate estimation of the interphase region using AFM force-distance curves, this distance need to be decreased. The existence of a softer interphase was also confirmed by separating the two epoxy blocks and applying indentations perpendicular to the interface plane at different depths. Lower modulus values were detected on the side of epoxy B at smaller indentation depths, where the modulus value increased gradually by increasing the indentation depth until it reached the bulk value.

The proposed system combined with the modified method of nanoindentation application have proven efficient in investigating the size of the interphase between epoxy and copper as well as the variation of its mechanical properties from the bulk. We claim this system can be used to investigate the interphase thickness and properties between polymers and metals in general, as the same sample preparation method can be applied.

In contrast with other literature studies, the results obtained in this work show that an interphase between epoxy and copper does not necessarily form. In fact, different epoxy/Cu interphase thicknesses were reported, even when the used epoxy system and the characterization method were identical.^{58,67,133} This suggests that the curing parameters, specifically the curing temperature, can play a major role in determining the final width of an interphase. For future work, it would be very useful to apply the same methods presented in this study in order to investigate in depth the influence of the curing parameters on the final width of the formed interphase between epoxy and copper. Furthermore, the variation of the interphase thickness can be related directly to the interfacial adhesion, and consequently, the performance of the composite. This can be very helpful in engineering the interphase in a way that serves the composite performance through altering the curing parameters.

References

1. Huang H, Talreja R. Numerical simulation of matrix micro-cracking in short fiber reinforced polymer composites: Initiation and propagation. *Compos Sci Technol.* 2006;66(15):2743–57.
2. Sharpe LH. The Interphase in Adhesion. *J Adhes.* 1972;4(1):51–64.
3. Drzal LT. The interphase in epoxy composites. In: *Epoxy Resins and Composites II.* Berlin/Heidelberg: Springer-Verlag; 1986.1–32.
4. Fishman SG. Interfaces in Composites. *JOM.* 1986;38(3):26–7.
5. Williams JG, Donnellan ME, James MR, Morris WL. Properties of the interphase in organic matrix composites. *Mater Sci Eng A.* 1990;126(1-2):305–12.
6. Piggott MR. Tailored Interphases in Fibre Reinforced Polymers. *MRS Proc.* 1989;170:265.
7. Fan HB, Wong CKY, Yuen MMF. A multi-scale method to investigate delamination in electronic packages. *J Adhes Sci Technol.* 2006;20(10):1061–78.
8. Vörös G, Pukánszky B. Modeling the Effect of a Soft Interlayer on the Stress Distribution around Fibers: Longitudinal and Transverse Loading. *Macromol Mater Eng.* 2002;287(2):139–48.
9. Cuadrado N, Casellas D, Anglada M, Jiménez-Piqué E. Evaluation of fracture toughness of small volumes by means of cube-corner nanoindentation. *Scr Mater.* 2012;66(9):670–3.
10. Pelletier H, Krier J, Mille P. Characterization of mechanical properties of thin films using nanoindentation test. *Mech Mater.* 2006;38(12):1182–98.
11. Sun Y, Liang J, Xu Z-H, Wang G, Li X. Nanoindentation for measuring individual phase mechanical properties of lead free solder alloy. *J Mater Sci Mater Electron.* 2008;19(6):514–21.
12. Gao S-L, Mäder E. Characterisation of interphase nanoscale property variations in glass fibre reinforced polypropylene and epoxy resin composites. *Compos Part A Appl Sci Manuf.* 2002;33(4):559–76.
13. Lee S-H, Wang S, Pharr GM, Xu H. Evaluation of interphase properties in a cellulose fiber-reinforced polypropylene composite by nanoindentation and finite element analysis. *Compos Part A Appl Sci Manuf.* 2007;38(6):1517–24.
14. Kumar R, Cross WM, Kjerengtroen L, Kellar JJ. Fiber bias in nanoindentation of polymer matrix composites. *Compos Interfaces.* 2004;11(5-6):431–40.
15. Hodzic A, Stachurski Z., Kim J. Nano-indentation of polymer–glass interfaces Part I. Experimental and mechanical analysis. *Polymer (Guildf).* 2000;41(18):6895–905.

16. VanLandingham MR, Dagastine RR, Eduljee RF, McCullough RL, Gillespie JW. Characterization of nanoscale property variations in polymer composite systems: 1. Experimental results. *Compos Part A Appl Sci Manuf.* 1999;30(1):75–83.
17. Thomas S, Joseph K, Malhotra SK, Goda K, Sreekala MS. *Polymer Composites: Volume 1.* Wiley-VCH; 2012.
18. Congress US. *Advanced Materials by Design.* Washington, DC: US Government Printing Office; 1988.
19. Peters PWM, Schulte K. Polymer Matrix Composites. In: *Advanced Aerospace Materials.* Berlin, Heidelberg: Springer Berlin Heidelberg; 1992.219–45.
20. McAdams, L. V. and Gannon JA. *High Performance Polymers and Composites.* Wiley; 1991. 258-318.
21. Dearborn EC, Fuoss RM, Mackenzie AK, Shepherd RG. Epoxy Resins from Bis- , Tris- , and Tetrakis-Glycidyl Ethers. *Ind Eng Chem.* 1953;45(12):2715–2721.
22. Gundjian M, Cole KC. Effect of copper on the curing and structure of a DICY-containing epoxy composite system. *J Appl Polym Sci.* 2000;75(12):1458–73.
23. Hamerton I. *Recent Developments in Epoxy Resins.* Rapra Review Reports. Rapra Technology Ltd; 1996.
24. Shechter L, Wynstra J, Kurkijy RP. Glycidyl Ether Reactions with Amines. *Ind Eng Chem.* 1956;48(1):94–97.
25. Vanlandingham MR, Eduljee RF, Gillespie Jr. JW. Relationships between stoichiometry, microstructure, and properties for amine-cured epoxies. *J Appl Polym Sci.* 1999;71(5):699–712.
26. Nikolic G, Zlatkovic S, Cakic M, Cakic S, Lacnjevac C, Rajic Z. Fast Fourier Transform IR Characterization of Epoxy GY Systems Crosslinked with Aliphatic and Cycloaliphatic EH Polyamine Adducts. *Sensors.* 2010;10(1):684–96.
27. Montserrat S, Flaqué C, Calafell M, Andreu G, Málek J. Influence of the accelerator concentration on the curing reaction of an epoxy-anhydride system. *Thermochim Acta.* 1995;269-270(C):213–29.
28. Fisch VW, Hofmann W. Chemischer aufbau von gehärteten epoxyharze. III. Mitteilung über chemie der epoxyharze. *Die Makromol Chemie.* 1961;44(1):8–23.
29. Pham HQ, Marks MJ. Epoxy Resins. In: *Ullmann's Encyclopedia of Industrial Chemistry.* Weinheim, Germany: Wiley-VCH Verlag GmbH & Co. KGaA; 2005.
30. Antoon MK, Koenig JL. Crosslinking mechanism of an anhydride-cured epoxy resin as studied by fourier transform infrared spectroscopy. *J Polym Sci Polym Chem Ed.* 1981;19(2):549–70.
31. Mauri AN, Galego N, Riccardi CC, Williams RJJ. Kinetic Model for Gelation in the Diepoxide–Cyclic Anhydride Copolymerization Initiated by Tertiary Amines. *Macromolecules.* 1997;30(6):1616–20.

32. Fedtke M, Domaratus F. Curing of epoxide resins by anhydrides of dicarboxylic acids: model reactions. *Polym Bull.* 1986;15(1):13–9.
33. Steinmann B. Investigations on the curing of epoxy resins with hexahydrophthalic anhydride. *J Appl Polym Sci.* 1989;37(7):1753–76.
34. Strong AB. *Fundamentals of Composites Manufacturing, Second Edition: Materials, Methods and Applications.* Second. Dearborn: Society of Manufacturing Engineers; 2008.
35. Selby K, Miller LE. Fracture toughness and mechanical behaviour of an epoxy resin. *J Mater Sci.* 1975;10(1):12–24.
36. Kim SL, Skibo MD, Manson JA, Hertzberg RW, Janiszewski J. Tensile, impact and fatigue behavior of an amine-cured epoxy resin. *Polym Eng Sci.* 1978;18(14):1093–100.
37. Drzal LT, Rich MJ, Koenig MF, Lloyd PF. Adhesion of Graphite Fibers to Epoxy Matrices: II. The Effect of Fiber Finish. 1983;16(2):133–152.
38. Packham DE. The Adhesion of Polymers to Metals: The Role of Surface Topography. In: *Adhesion Aspects of Polymeric Coatings.* Boston, MA: Springer US; 1983.19–44.
39. Jesson DA, Watts JF. The Interface and Interphase in Polymer Matrix Composites: Effect on Mechanical Properties and Methods for Identification. *Polym Rev.* 2012;52(3):321–54.
40. Drzal LT, Rich MJ, Lloyd PF. Adhesion of graphite fibers to epoxy matrices: I. The role of fiber surface treatment. *J Adhes.* 1983;16(1):1–30.
41. Saelhoff A, Wilms C, Warnecke M, Pico D, Sernecki M, Seide G, Gries T. Matrix / Fibre Boundary Layer in Fibre Reinforced Plastics : Characterization of the Adhesion. *Chemical Engineering Transactions.* 2013;32:1633-1638.
42. Tannenbaum R, Zubris M, David K, Ciprari D, Jacob K, Jasiuk I et al. FTIR Characterization of the Reactive Interface of Cobalt Oxide Nanoparticles Embedded in Polymeric Matrices. *J Phys Chem B.* 2006;110(5):2227-2232
43. Pangelinan AB, McCullough RL, Kelley MJ. Analytic model for surface-induced molecular weight segregation in thermoplastic composites. *J Polym Sci Part B Polym Phys.* 1994;32(14):2383–94.
44. Lesko JJ, Jayaraman K, Reifsnider KL. Gradient Interphase Regions in Composite Systems. *Key Eng Mater.* 1996;116-117:61–86.
45. Peacock JA, Fife B, Nield E, Crick RA. Examination Of The Morphology Of Aromatic Polymer Composite (APC-2) Using An Etching Technique. In: Ishida H, Koenig JL, redakteurs. *The first International Conference on Composite Interface.* Cleveland: Elsevier Publishing Co., Inc.; 1986.299–305.

46. Munz M. Evidence for a three-zone interphase with complex elastic–plastic behaviour: nanoindentation study of an epoxy/thermoplastic composite. *J Phys D Appl Phys.* 2006;39(18):4044–58.
47. Fink BK, McCullough RL. Interphase research issues. *Compos Part A Appl Sci Manuf.* 1999;30(1):1–2.
48. Yu S, Yang S, Cho M. Multi-scale modeling of cross-linked epoxy nanocomposites. *Polymer (Guildf).* 2009;50(3):945–52.
49. Drzal LT. Composite Property Dependence on the Fiber, Matrix, and the Interphase. In: *Tough Composite Materials: Recent Developments.* Park Ridge: Noyes Publications; 1985.227–43.
50. Odegard GM, Clancy TC, Gates TS. Modeling of the mechanical properties of nanoparticle/polymer composites. *Polymer (Guildf).* 2005;46(2):553–62.
51. Palmese GR, McCullough RL. Kinetic and Thermodynamic Considerations Regarding Interphase Formation in Thermosetting Composite Systems. *J Adhes.* 1994;44(1-2):29–49.
52. Garton A, Stevenson WTK, Wang S. Interfacial reactions in carbon-epoxy composites. *Br Polym J.* 1987;19(5):459–67.
53. Fitzer E, Geigl K-H, Hüttner W, Weiss R. Chemical interactions between the carbon fibre surface and epoxy resins. *Carbon N Y.* 1980;18(6):389–93.
54. Bolger JC. Acid Base Interactions Between Oxide Surfaces and Polar Organic Compounds. In: *Adhesion Aspects of Polymeric Coatings.* Boston, MA: Springer US; 1983.3–18.
55. Hong S-G, Tsai J-S. The adsorption and curing behaviors of the epoxy/amidoamine system in the presence of metal oxides. *J Therm Anal Calorim.* 2001;63(1):31–46.
56. Nakamae K, Nishino T, Airu X, Asaoka S. Localization of the curing agent at an epoxy resin/oxidized aluminium interface. *Int J Adhes Adhes.* 1995;15(1):15–20.
57. Boerio FJ, Hong PP. Non-destructive characterization of epoxy-dicyandiamide interphases using surface-enhanced Raman scattering. *Mater Sci Eng A.* 1990;126(1-2):245–52.
58. Chung J, Munz M, Sturm H. Stiffness variation in the interphase of amine-cured epoxy adjacent to copper microstructures. *Surf Interface Anal.* 2007;39(7):624–33.
59. Kelber JA, Rogers JW, Banse BA, Koel BE. Interaction of dimethylamine with clean and partially oxidized copper surfaces. *Appl Surf Sci.* 1990;44(3):193–204.
60. Skourlis TP, McCullough RL. An experimental investigation of the effect of prepolymer molecular weight and stoichiometry on thermal and tensile properties of epoxy resins. *J Appl Polym Sci.* 1996;62(3):481–90.
61. Racich JL, Koutsky JA. Boundary Layers in Thermosets. In: *Chemistry & Properties of Crosslinked Polymers.* Elsevier; 1977.303–23.

62. Yim H, Kent M, McNamara WF, Ivkov R, Satija S, Majewski J. Structure within Thin Epoxy Films Revealed by Solvent Swelling: A Neutron Reflectivity Study. *Macromolecules*. 1999;32(23):7932–8.
63. Ondrus DJ, Boerio FJ, Grannen KJ. Molecular Structure of Polymer/Metal Interphases. 1989; 29(1-4):27-42.
64. Boerio F., Ondrus D. Effect of substrates on the structure of polymer interphases. *J Colloid Interface Sci*. 1990;139(2):446–56.
65. Yang F, Pitchumani R. A kinetics model for interphase formation in thermosetting matrix composites. *J Appl Polym Sci*. 2003;89(12):3220–36.
66. Oyama HT, Lesko JJ, Wightman JP. Interdiffusion at the interface between poly(vinylpyrrolidone) and epoxy. *J Polym Sci Part B Polym Phys*. 1997;35(2):331–46.
67. Munz M, Cappella B, Sturm H, Geuss M, Schulz E. Materials Contrasts and Nanolithography Techniques in Scanning Force Microscopy (SFM) and their Application to Polymers and Polymer Composites. In: *Advances in Polymer Science*. Springer Berlin Heidelberg; 2003.87–210.
68. Kardos JL. The Role of the Interface in Polymer Composites — Some Myths, Mechanisms, and Modifications. In: *Molecular Characterization of Composite Interfaces*. Berlin, Heidelberg: Springer Berlin Heidelberg; 1985.1–11.
69. Eirich FR. Some mechanical and molecular aspects of the performance of composites. *Appl Polym Symp*. 1984;39(1):93–102.
70. Piggott MR. The effect of the interface/interphase on fiber composite properties. *Polym Compos*. 1987;8(5):291–7.
71. Di Anselmo A, Jancar J, Benedetto AT, Kenny JM. Finite element analysis of the effect of an interphase on the mechanical properties of polymeric composite materials: A review. In: Benedetto AT, Nicolais L, Watanabe R, redakteurs. *Composite Materials*. First. Amsterdam: Elsevier; 1992.
72. Tsai HC, Arocho AM, Gause LW. Prediction of fiber-matrix interphase properties and their influence on interface stress, displacement and fracture toughness of composite material. *Mater Sci Eng A*. 1990;126(1-2):295–304.
73. Jancar J. Review of the role of the interphase in the control of composite performance on micro- and nano-length scales. *J Mater Sci*. 2008;43(20):6747–57.
74. Lee SM. *Handbook of Composite Reinforcements*. John Wiley & Sons; 1992. 715.
75. Vanlandingham MR, Eduljee RF, Gillespie JW. Moisture diffusion in epoxy systems. *J Appl Polym Sci*. 1999;71(5):787–98.
76. Drzal LT, Rich MJ, Koenig MF. Adhesion of Graphite Fibers to Epoxy Matrices. III. The Effect of Hygrothermal Exposure. *J Adhes*. 1985;18(1):49–72.

77. Faupel F, Strunskus T, Kiene M, Thran A, Bechtolsheim C V., Zaporojtchenko V. Fundamental Aspects Of Polymer Metallization. *MRS Proc.* 1998;511:15.
78. Soane DS, Martynenko Z. *Polymers in microelectronics: fundamentals and applications.* Amsterdam: Elsevier Science Publishers; 1989.
79. Bouchet J, Roche A-A. The Formation of Epoxy/Metal Interphases: Mechanisms and Their Role in Practical Adhesion. *J Adhes.* 2002;78(9):799–830.
80. Duprat M, Dabosi F. Corrosion Inhibition of a Carbon Steel in 3% NaCl Solutions by Aliphatic Amino-Alcohol and Diamine Type Compounds. 1981;37(2):89-92.
81. Lee HY, Park GS. Failure paths at copper-base leadframe/epoxy molding compound interfaces. *J Mater Sci.* 2002;37(19):4247–57.
82. Chung PWK, Yuen MMF, Chan PCH, Ho NKC, Lam DCC. Effect of copper oxide on the adhesion behavior of Epoxy Molding Compound-copper interface. In: 52nd Electronic Components and Technology Conference 2002. IEEE; 2002.1665–70.
83. Chan EKL, Fan H, Yuen MMF. Effect of Interfacial Adhesion of Copper/Epoxy under Different Moisture Level. In: 7th Int Conf on Thermal, Mechanical and Multiphysics Simulation and Experiments in Micro-Electronics and Micro-Systems. IEEE; 2006.1–5.
84. Filbey JA, Wightman JP. Surface Characterization in Polymer/Metal Adhesion. In: *Adhesive Bonding.* Boston, MA: Springer US; 1991.175–202.
85. Herrera-Franco PJ, Drzal LT. Comparison of methods for the measurement of fibre/matrix adhesion in composites. *Composites.* 1992;23(1):2–27.
86. Fakirov S, Bhattacharyya D. *Handbook of Engineering Biopolymers.* München: Carl Hanser Verlag GmbH & Co. KG; 2007.
87. Poon B, Rittel D, Ravichandran G. An analysis of nanoindentation in linearly elastic solids. *Int J Solids Struct.* 2008;45(24):6018–33.
88. Fischer-Cripps AC. *Nanoindentation.* New York, NY: Springer New York; 2011.
89. Hertz H. Ueber die Berührung fester elastischer Körper. *J für die reine und Angew Math (Crelle's Journal).* 1882;1882(92):156–71.
90. Boussinesq J. *Applications of potentials for the study of equilibrium and motion of elastic solids.* Paris: Gautier-Villars. 1885.
91. Sneddon IN. Boussinesq's problem for a rigid cone. *Math Proc Cambridge Philos Soc.* 1948;44(04):492.
92. Sneddon IN. The relation between load and penetration in the axisymmetric boussinesq problem for a punch of arbitrary profile. *Int J Eng Sci.* 1965;3(1):47–57.
93. Miller R, Rodney D. On the nonlocal nature of dislocation nucleation during nanoindentation. *J Mech Phys Solids.* 2008;56(4):1203–23.

94. Doerner MF, Nix WD. Summary for Policymakers. In: Intergovernmental Panel on Climate Change, redakteur. *Climate Change 2013 - The Physical Science Basis*. Cambridge: Cambridge University Press; 1986.1–30.
95. Oliver WC, Pharr GM. An improved technique for determining hardness and elastic modulus using load and displacement sensing indentation experiments. *J Mater Res*. 1992;7(06):1564–83.
96. Cheng C-M, Cheng Y. On the initial unloading slope in indentation of elastic-plastic solids by an indenter with an axisymmetric smooth profile. *Appl Phys Lett*. 1997;71(18):2623.
97. Pharr GM, Bolshakov A. Understanding nanoindentation unloading curves. *J Mater Res*. 2002;17(10):2660–71.
98. Tromas C, Verdier M, Fivel M, Aubert P, Labdi S, Feng ZQ et al. Mechanical and Nanomechanical Properties. In: *Nanomaterials and Nanochemistry*. Berlin, Heidelberg: Springer Berlin Heidelberg; 2007.229–67.
99. Herrmann K, Jennett N., Wegener W, Meneve J, Hasche K, Seemann R. Progress in determination of the area function of indenters used for nanoindentation. *Thin Solid Films*. 2000;377-378:394–400.
100. Bolshakov A, Pharr GM. Influences of pileup on the measurement of mechanical properties by load and depth sensing indentation techniques. *J Mater Res*. 1998;13(04):1049–58.
101. Rar A, Sohn S, Oliver WC, Goldsby DL, Tullis TE, Pharr GM. On the Measurement of Creep by Nanoindentation with Continuous Stiffness Techniques. *MRS Proc*. 2004;841:R4.2.
102. McElhaney KW, Vlassak JJ, Nix WD. Determination of indenter tip geometry and indentation contact area for depth-sensing indentation experiments. *J Mater Res*. 1998;13(05):1300–6.
103. Choi Y, Lee HS, Kwon D. Analysis of sharp-tip-indentation load-depth curve for contact area determination taking into account pile-up and sink-in effects. *J Mater Res*. 2004;19(11):3307–15.
104. Maier V, Merle B, Göken M, Durst K. An improved long-term nanoindentation creep testing approach for studying the local deformation processes in nanocrystalline metals at room and elevated temperatures. *J Mater Res*. 2013;28(09):1177–88.
105. Chudoba T, Richter F. Investigation of creep behaviour under load during indentation experiments and its influence on hardness and modulus results. *Surf Coatings Technol*. 2001;148(2-3):191–8.
106. Binnig G, Quate CF, Gerber C. Atomic Force Microscope. *Phys Rev Lett*. 1986;56(9):930–3.
107. Cappella B, Dietler G. Force-distance curves by atomic force microscopy. *Surf Sci Rep*. 1999;34:1–104.

108. Brandl F, Sommer F, Goepferich A. Rational design of hydrogels for tissue engineering: Impact of physical factors on cell behavior. *Biomaterials*. 2007;28(2):134–46.
109. Vanlandingham MR, McKnight SH, Palmese GR, Bogetti TA, Eduljee RF, Gillespie JW. Characterization of Interphase Regions Using Atomic Force Microscopy. *MRS Proc*. 1996;458:313.
110. Bogetti TA, Wang T, VanLandingham MR, Gillespie JW. Characterization of nanoscale property variations in polymer composite systems: 2. Numerical modeling. *Compos Part A Appl Sci Manuf*. 1999;30(1):85–94.
111. Tsukruk VV., Singamaneni S. *Scanning Probe Microscopy of Soft Matter*. Weinheim, Germany: Wiley-VCH Verlag GmbH & Co. KGaA; 2011.
112. Fortier H, Variola F, Wang C, Zou S. AFM force indentation analysis on leukemia cells. *Anal Methods*. 2016;8(22):4421–31.
113. Calabri L, Pugno N, Menozzi C, Valeri S. AFM nanoindentation: tip shape and tip radius of curvature effect on the hardness measurement. *J Phys Condens Matter*. 2008;20(47):474208.
114. Laurent-Brocq M, Béjanin E, Champion Y. Influence of roughness and tilt on nanoindentation measurements: A quantitative model. *Scanning*. 2015;37(5):350–60.
115. Safavi-Ardebili V, Sinclair AN, Spelt JK. Experimental Investigation of the Interphase in an Epoxy-Aluminum System. *J Adhes*. 1997;62(1-4):93–111.
116. Johnson KL. *Contact Mechanics*. First. Cambridge: Cambridge University Press; 1987.
117. Yedla SB, Kalukanimuttam M, Winter RM, Khanna SK. Effect of Shape of the Tip in Determining Interphase Properties in Fiber Reinforced Plastic Composites Using Nanoindentation. *J Eng Mater Technol*. 2008;130(4):041010.
118. Downing TD, Kumar R, Cross WM, Kjerengtroen L, Kellar JJ. Determining the interphase thickness and properties in polymer matrix composites using phase imaging atomic force microscopy and nanoindentation. *J Adhes Sci Technol*. 2000;14(14):1801–12.
119. Li F, Williams JG, Altan BS, Miskioglu I, Whipple RL. Studies of the interphase in epoxy–aluminum joints using nano-indentation and atomic force microscopy. *J Adhes Sci Technol*. 2002;16(7):935–49.
120. Chung J. *Nanoscale Characterization of Epoxy Interphase on Copper Microstructures*. Technische Universität Berlin; 2006.
121. Mai K, Mäder E, Mühle M. Interphase characterization in composites with new non-destructive methods. *Compos Part A Appl Sci Manuf*. 1998;29(9-10):1111–9.
122. Munz M, Sturm H, Schulz E, Hinrichsen G. The scanning force microscope as a tool for the detection of local mechanical properties within the interphase of fibre reinforced polymers. *Compos Part A Appl Sci Manuf*. 1998;29(9-10):1251–9.

123. Hexion Inc. Technical Datasheet of EPIKOTE™ Resin MGS™ RIMR 135 and EPIKURE™ Curing Agent MGS™ RIMH 134–RIMH 137. 2006.
124. Billiet S, Van Camp W, Hillewaere XKD, Rahier H, Du Prez FE. Development of optimized autonomous self-healing systems for epoxy materials based on maleimide chemistry. *Polymer (Guildf)*. 2012;53(12):2320–6.
125. Bozzola JJ. Electron Microscopy. In: *Encyclopedia of Life Sciences*. Chichester, UK: John Wiley & Sons, Ltd; 2001.1–8.
126. DiATOME Diamond Knives. *Diamond Knife Handling and Use Manual*.
127. Holbery JD, Eden VL. A comparison of scanning microscopy cantilever force constants determined using a nanoindentation testing apparatus. *J Micromechanics Microengineering*. 2000;10(1):85–92.
128. Bhushan B, Kulkarni AV., Bonin W, Wyrobek JT. Nanoindentation and picoindentation measurements using a capacitive transducer system in atomic force microscopy. *Philos Mag A*. 1996;74(5):1117–28.
129. Hysitron®. *TS 75 TriboScope® User Manual*.
130. Rosato DV, Rosato MG. Testing, Inspection, and Quality Control. In: *Injection Molding Handbook*. Boston, MA: Springer US; 2000.1028–126.
131. Williams RJ, Hudson RW. Some techniques for the examination of high impact polystyrene by electron microscopy. *Polymer (Guildf)*. 1967;8:643–50.
132. Mott B. *Micro-indentation hardness testing*. London: Butterworth; 1956.
133. Munz M, Sturm H, Schulz E. Interphase characterization via the stiffness contrast of a scanning force microscope in displacement modulation mode. *Surf Interface Anal*. 2000;30(1):410–4.
134. Aufray M, Roche AA. Residual stresses and practical adhesion: effect of organo-metallic complex formation and crystallization. *J Adhes Sci Technol*. 2006;20(16):1889–903.
135. Hofmeister C, Maaß S, Fladung T, Thiel K, Mayer B. Influence of copper layer on epoxy acrylate based solder mask surface chemistry and the effect on epoxy adhesion. *Appl Adhes Sci*. 2015;3(1):12.
136. Chemicals CS. Hot curing epoxy system based on Araldite ® LY 556 / Hardener HY 917 / Accelerator DY 070 Datasheet. 1998.
137. Rabearison N, Jochum C, Grandidier JC. A cure kinetics, diffusion controlled and temperature dependent, identification of the Araldite LY556 epoxy. *J Mater Sci*. 2011;46(3):787–96.
138. Chen S, Liu L, Wang T. Investigation of the mechanical properties of thin films by nanoindentation, considering the effects of thickness and different coating–substrate combinations. *Surf Coatings Technol*. 2005;191(1):25–32.